



Axial flow turbine for solar updraft towers

PhD dissertation

by

Walid Mohammed Abdel-Magid Abdel-Motalb Belal

DOI: 10.54598/002120

Gödöllő

2022

**Doctoral school
denomination:**

Doctoral School of Mechanical Engineering

Science:

Renewable energy

Leader:

Prof. Dr. Farkas István, DSc

Faculty of Mechanical Engineering

Hungarian University of Agriculture and Life Sciences, Gödöllő, Hungary

Supervisor:

Prof. Dr. István Keppler, PhD

Institute of Technology

Hungarian University of Agriculture and Life Sciences, Gödöllő, Hungary

Dr. Ildikó Molnar, PhD

Faculty of Mechanical and Safety Engineering

Óbuda University, Budapest, Hungary

.....

Affirmation of head of school

.....

Affirmation of supervisor

CONTENTS

NOMENCLATURE AND ABBREVIATIONS	5
1. INTRODUCTION AND OBJECTIVES	7
1.1. Introduction.....	7
1.2. The main research objectives	8
2. LITERATURE REVIEW	9
2.1. Description of solar chimney	9
2.2. A Solar chimney	11
2.2.1. <i>Studies of the chimney effect</i>	<i>11</i>
2.2.2. <i>Studies of greenhouse effect</i>	<i>13</i>
2.2.3. <i>Hybrid solar chimney</i>	<i>16</i>
2.3. Approach of a turbine for solar chimney power plant.....	22
2.4. Designs for a turbine for solar chimney power plant.....	23
2.4.1. <i>Free vortex theory design.....</i>	<i>24</i>
2.4.2. <i>Blade element theory design.....</i>	<i>25</i>
2.5. Aerodynamics of shrouded wind turbine	26
2.5.1. <i>Studies shape duct and its effect.....</i>	<i>26</i>
2.5.2. <i>Improvement of the blade shape.....</i>	<i>28</i>
2.5.3. <i>Calculation of system performance</i>	<i>29</i>
2.6. Timeline of the previous researches	33
2.7. Characteristics of the solar chimney turbine	37
2.8. Summary of literature review evaluation.....	38
3. MATERIALS AND METHODS	39
3.1. Aerodynamic analysis of a shrouded turbine.....	39
3.1.1. <i>Actuator disc theory considering surrounding duct.....</i>	<i>40</i>
3.1.2. <i>Rotor disc theory considering surrounding duct.....</i>	<i>42</i>
3.1.3. <i>Blade element theory considering surrounding duct</i>	<i>42</i>
3.2. Mathematical model of Solar Chimney	44
3.2.1. <i>Collector.....</i>	<i>45</i>
3.2.2. <i>Heat transfer coefficient calculation.....</i>	<i>47</i>
3.2.3. <i>Chimney.....</i>	<i>49</i>
3.2.4. <i>Turbine</i>	<i>49</i>
3.3. Optimal design of blade geometry.....	50
3.4. CFD model of solar chimney	51
3.4.1. <i>Turbulent modelling</i>	<i>54</i>
3.4.2. <i>Grid generation</i>	<i>59</i>
3.4.3. <i>Boundary conditions.....</i>	<i>63</i>

3.4.4.	<i>Coupled fluid–structure interaction simulations</i>	66
3.5.	Experimental apparatus	67
3.5.1.	<i>Layout of experimental rig</i>	68
3.5.2.	<i>Measurement strategy</i>	70
3.5.3.	<i>The sensors of the measurements</i>	71
4.	RESULTS AND DISCUSSIONS	74
4.1.	The mathematical model of solar chimney power plant	74
4.1.1.	<i>Temperature profile of the collector</i>	75
4.1.2.	<i>The effect of mass flow rate</i>	76
4.2.	The methodology of turbine design working on SCPP	76
4.3.	Simulation SCPP with radiation models and turbine	78
4.4.	The influence of the solar collector shape	81
4.4.1.	<i>The square shape collector</i>	82
4.4.2.	<i>The circular shape collector</i>	82
4.5.	Comparing of the different theories of the turbine design	85
4.6.	Wind tunnel measurements	87
4.7.	New scientific results	91
5.	CONCLUSIONS AND SUGGESTIONS	94
6.	SUMMARY	95
7.	ÖSSZEFOGLALÁS (SUMMARY IN HUNGARIAN).....	96
8.	APPENDICES	97
A.1.	Bibliography	97
A.2.	Publications related to the thesis	102
A.3.	Engineering Drawing	103
A.1.1	<i>Drawing of my designed blade</i>	103
A.2.1	<i>Drawing of the hub</i>	107
9.	ACKNOWLEDGMENTS	108

NOMENCLATURE AND ABBREVIATIONS

a, ar	average and local axial induction factors at the rotor
a'	tangential induction factors at the rotor
A	flow area (m^2)
b	thermal penetration coefficient ($W s^{1/2} / m^2 K$)
B	number of blades
c	Chord (m)
C_d	drag coefficient
C_l	lift coefficient
C_M	torque coefficient
C_n	normal force coefficient
C_{p3}	pressure coefficient at the diffuser outlet
c_p	specific heat capacity at constant pressure ($J/kg K$)
C_P	power coefficient
C_t	tangential force coefficient
C_T	thrust coefficient
dA	elementary area (m^2)
dM	elementary torque ($N m$)
dP	elementary power (W)
F	Prandtl tip-loss factor
g	gravitational acceleration (m/s^2)
h	heat transfer convection coefficient ($W/m^2 K$)
H_c	chimney height (m)
h_r	radiation heat transfer coefficient ($W/m^2 K$)
H_R	roof height above the ground (m)
h_w	wind convection heat transfer ($W/m^2 K$)
k	specific heat ratio
K	thermal conductivity ($W/m K$)
I	solar irradiation (W/m^2)
\dot{m}	mass flow rate (kg/s)
N_{um}	mean Nusselt numbers
p	pressure (Pa)
P	output power(W)
q	heat flux (W/m^2)
r	radial position (m)
R	ideal gas constant ($J/kg K$)
Re	Reynolds number
T	absolute temperature(K)
U_b	ground heat transfer coefficient ($W/m^2 K$)
U_t	collector loss coefficient ($W/m^2 K$)
V	air velocity(m/s)
w	total induced velocity (m/s)
W	relative velocity (m/s)
x	local-speed ratio

Nomenclature and abbreviations

Greek symbols

α	angle of attack, rad
α_p, α_c	absorptivity of the ground and the cover
β	area ratio
γ	diffuser velocity ratio
ε	velocity ratio
η	efficiency
θ	twist angle, rad
λ	tip-speed ratio
ρ	density of the fluid (kg/m ³)
σ_s	solidity of the turbine
τ_c	transmissivity of the cover
ϕ	flow angle, rad
Ω	angular speed of the turbine (rad/s)

1. INTRODUCTION AND OBJECTIVES

In this chapter, the importance of the research topic and brief description of the solar chimney power plant are presented along with the objectives of this research.

1.1. Introduction

Energy drives all modern economic systems. With the rapidly growing world population, more energy should be produced to satisfy rising human requirements and to maintain the welfare. So, harvesting energy on a large scale is undoubtedly one of the main challenges of our time. The global energy demand has continued to increase, but the means of meeting this demand have been mainly the use of non-renewable energy resources. More than 78% of the world's energy consumption in 2013 was supplied directly from fossil fuels, which also provides about 2.6 % from nuclear energy and 19% from renewable energies. With the increasing need for energy and limitation of fossil fuel resources, human beings are more aware of the importance of renewable energies, according to Fig. 1.1 (Arzpeyma et al. 2019). Using non-renewable energy supply sources such as fossil fuel burdens the environment with greenhouse gas emission and global warming, while the flared hot flue gas causes global warming in the atmosphere where the process occurs. The power generation sector was the highest contributor to global greenhouse gas emission in 2005 which accounted for about 25 percent of global greenhouse gas emission (Al-Kayiem and Aja, 2016).

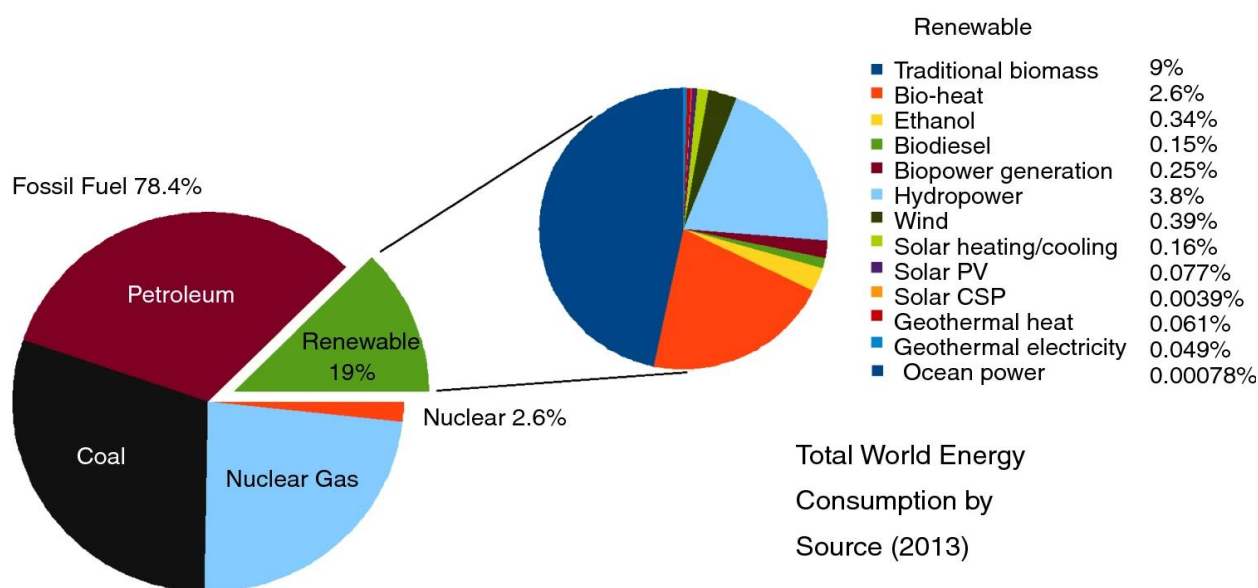


Fig. 1.1. Statistical analysis of world energy consumption (Arzpeyma et al., 2019)

Solar energy is the most abundant and well distributed form of renewable energy. Many solar technologies are used to harvest the sun's energy throughout the world. The annual renewable energy supply exceeds the global energy demand shown in the previous section on evolution of the world energy demand by several orders of magnitude. 6.48×10^{18} MJ of solar energy reaches the surface of the Earth, which is about ten thousand times more than the annual global primary energy demand and much more than all available energy reserves on our planet (Quaschnig, 2014). This solar energy reaches earth in two forms: direct and indirect solar energy. Solar technical systems using direct solar energy convert incoming solar radiation directly into useful energy, for instance, electricity or heat. Wind, river water and plant growth are indirect forms of solar energy. However, natural processes convert solar energy into other types of energy, then, other technical systems can use these indirect types of solar energy as well.

The most promising solution is an extension of using the renewable energy source, consequently, renewable energy gradually can be the main source of the world energy system (Guo et al., 2019). Solar chimney power plant (SCPP) is a new technology that utilizes renewable energy sources to produce electricity, for achieving its goals, it uses the combination of solar heating and chimney effect. The SCPP has low-efficiency but is favoured with well-developed technologies that make up the system. The materials for the development of the system are easily sourced locally. Thus, the plant has a promising future as a large-scale solar-electric power plant. The SCPP is characterized by a long lifespan, little maintenance, no combustible fuel, no cooling water and it is free of greenhouse gas emissions. The SCPP technologies are simple, reliable and can be developed in technologically less developed countries, which are sunny and often have limited draw material resources for other advanced technologies.

1.2. The main research objectives

The objective of this research is to design axial single stage turbine to obtain the maximum output power possible from SCPP. The design of an axial flow turbine is presented based the Blade Element Theory (BET), which is modified to improve the performance of the wind turbine by the concept of Argument diffuse wind turbine (ADWT). I also used the mathematical model to predict the expected output power. According to the characteristics of the solar chimney turbine, blade element theory is chosen to design solar chimney turbine. An aerodynamic analysis accounting the surrounding diffuser duct is presented, which defines parameters of the design.

My comprehensive mathematical model is used to calculate the design parameters. My The mathematical model depends on easily measurable quantities to estimate the performance of SCPP. The performance of the whole SCPP system is accurately analysed by using CFD simulation model, with fewer assumptions in the theoretical calculation, but more detailed description of pressure and flow field could be obtained. A 3D approach for SCPP prototype is carried out by using ANSYS CFX v18 with axial vertical flow turbine. I manufactured the solar chimney turbine by using the 3D printing technology. The blade calculations were according my new approach of BET, which consider the surrounding duct. I have tested my newly designed turbine blades using a wind tunnel of 1m diameter and 8 m length. I measured the electrical output power, pressure difference around the turbine and airflow rate to calculate dimensionless parameters. Therefore, the following methods could be used in the research to accomplish the following objectives and tasks:

- Investigation of the performance of the SCPP by mathematical model to deeply understand the concept of SCPP and calculate the parameters of the turbine design.
- Estimation of the performance of the SCPP with different collector shapes by CFD simulation.
- Comparison of the different theories of the turbine design using evaluation of their performance within the SCPP simulation.
- Solution of the blade element theory (BET) equations with the diffuser duct effect to make the blade more sensitive and to have efficient performance.
- Testing the performance of the turbine using wind tunnel measurements.

2. LITERATURE REVIEW

Utilization of renewable energy has therefore been the goal of numerous researchers to improve the cost of energy production. To that end, many innovative concepts have been proposed to capture more energy from the renewable energy sources such as solar, wind, and hydroelectric energy.

The following literature survey focuses on the solar chimney power plant (SCPP), and pays more attention to axial flow turbine designs for operation in SCPP. A solar chimney power plant is a rather new technology proposed to be a device that generates electricity in large scale by transforming solar energy into mechanical energy, and then convert mechanical energy to electrical energy. Many researchers give insight into how far the field is developed and how other researchers have focused on the overall plant analysis. It can be expected that the solar chimney will undergo a similar process of improvement as other renewable energy sources.

2.1. Description of solar chimney

The solar chimney power plant (SCPP) is one option that will help in global electricity production by using renewable energy resources. The SCPP is a low temperature power plant consisting of three essential elements. A typical SCPP consists of three major components, namely, a solar collector, a chimney and wind turbines, as shown in Fig. 2.1. In a SCPP, solar radiation collected by the solar collector and greenhouse effect, which heats up the ambient air entering the collector; then the hot air flows into the chimney through the collector exit, which is also the entrance of the chimney. In the chimney, the air density difference between the inside and outside of the chimney causes a large pressure difference between the system and the ambient air (chimney effect), which will drive the wind turbine installed at the chimney base to generate electricity (wind turbine effect). The SCPP has no adverse effect on the environment, needs no cooling water and has extremely low maintenance costs. Furthermore, the SCPP can operate even at nights since the soil under the collector works, as a natural heat storage system. These distinct advantages have made SCPP an attractive option for utilizing solar energy.

As mentioned, a solar chimney power plant converts solar radiation into mechanical energy, then electricity by using well-known principles: the greenhouse effect, buoyancy of the chimney, and wind turbine. The sun radiation under a large glass/ plastic roof produces hot air. Direct and diffuse solar radiation fall down on the transparent roof, where specific fractions of the energy are transmitted, absorbed and reflected, the quantities of these fractions depend on the solar incidence angle and optical characteristics of the glass, such as the thickness, refractive index and extinction coefficient.

The transmitted solar radiation reaches the ground surface; a part of the energy is absorbed while another part is reflected back to the roof, where it is again reflected to the ground. The multiple reflection of radiation continues, resulting in a higher fraction of energy absorbed by the ground, known as the transmittance- absorptance product of the ground. Through the mechanism of natural convection, the warm ground surface heats the near air, causing it to rise. The buoyant air rises up into the chimney of the plant, thereby drawing in more air at the collector perimeter and thus initiating forced convection, which heats the collector air more rapidly. Through mixed convection, the warm collector air heats the underside of the collector roof (Dhahri and Omri, 2013).

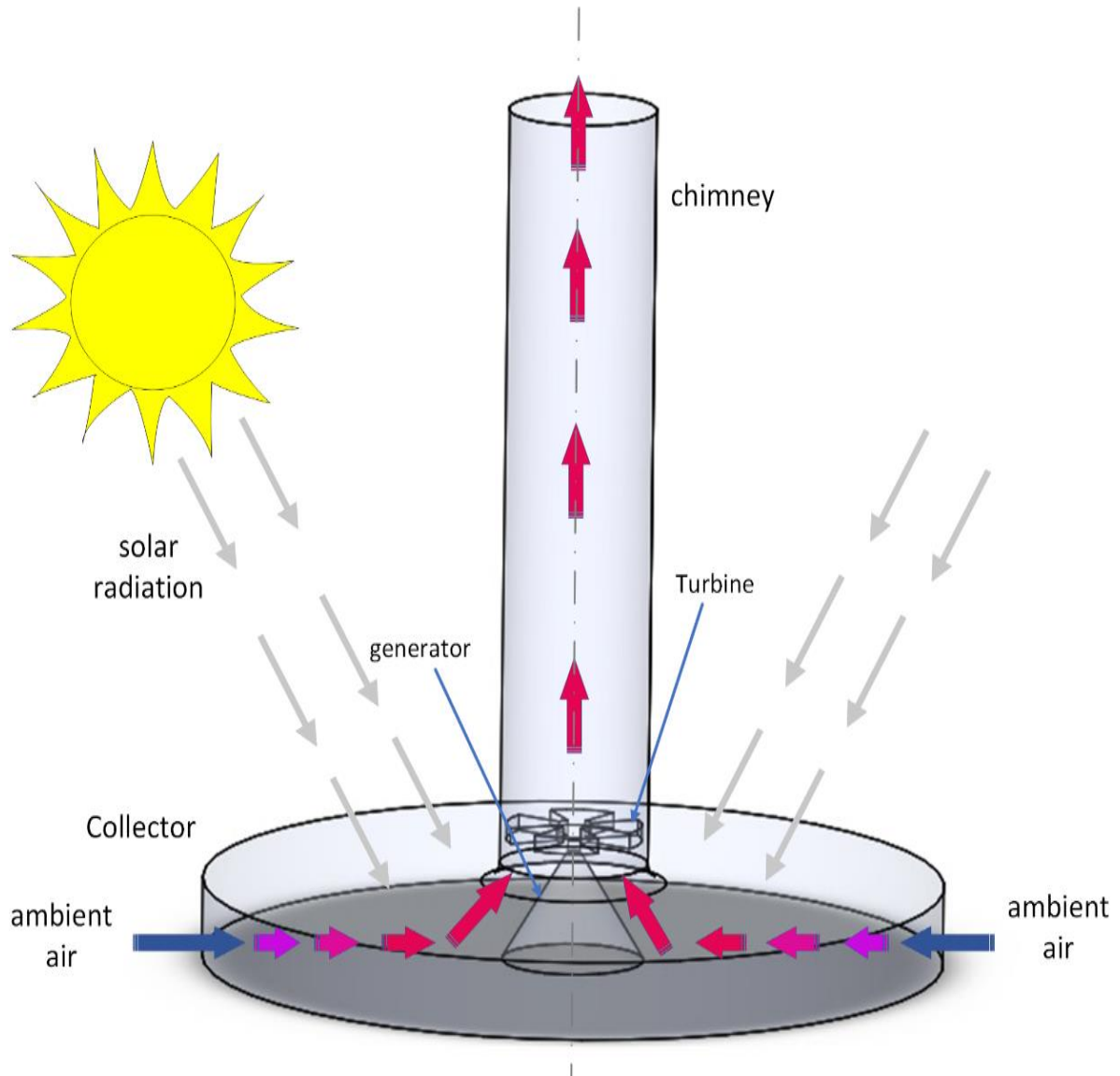


Fig. 2.1. Schematic diagram of SCPP

The chimney converts the solar energy absorbed by the solar collector into kinetic energy. The driving force (buoyancy) produced from the density difference that created by the rise in temperature in the collector and the change in density due to change in altitude plays a role in buoyancy. The difference in density between air inside the chimney and the ambient air generates a pressure potential according to the law of buoyancy that causes the flow through the solar chimney. The magnitude of the flow and the pressure drop over the turbine determine the maximum power that the turbine can extract from the flow.

A wind turbine is one of the main sub-systems (Key Part) of a solar chimney power plant, which converts the fluid power from the hot air to shaft power and transmits it to the generator. A typical layout of a solar chimney power plant has a single axial flow turbine. It has significant influence on the plant as the turbine pressure drop and plant mass flow rate are coupled. The typical solar chimney turbine is of the axial flow type. It has characteristics between those of wind turbines and gas turbines. However, the solar chimney turbines have a much higher energy extraction per unit

flow and are more akin to gas turbines, and the rotor blades are adjustable, like those of wind turbines.

2.2. A Solar chimney

Solar energy is the most abundant and well distributed form of renewable energy. So, many solar technologies are developed to encourage of using the solar energy throughout the world. In 1976, M. Simon showed the solar chimney has reasonable economic feasibility for production of the SCPP. Haaf *et al.*, (1983) was continuing Simon's work in 1979 by developing the first pilot prototype of SCPP in Manzanares, Spain, which was designed peak output of 50 kW, whereas in fact, the measured output was 36 kW (Haaf, 1984). This pilot plant was testing from the year 1982 to 1989. The most important finding of the prototype is the solar chimney concept has enough technically viable and operated reliably for electricity production.

Significant research effort has been put into the construction, simulation and operation of the solar chimney collector. An analytical model has been presented to study detailed performance for main plant elements (collector, chimney and wind turbine). Those researches evaluate the influence of a developed convective heat transfer equation, more accurate turbine inlet loss coefficient, quality collector roof glass, and various types of soil effect on the performance of a large-scale solar chimney power plant. The experimental studies are also done to obtain more accurate performance of solar chimney power plant. Many test rigs were created in many countries such as Spain, China and South Africa, so the analytical models were validated by comparison with experimental results. In this work, a survey of the previous research is presented in following.

2.2.1. Studies of the chimney effect

Mullett, (1987) developed analysis for the SCPP, aimed particularly to calculate overall efficiency and performance. He concluded that the solar chimney is essentially a power generator of large scale, Overall efficiency is directly related to the height of the chimney and is shown to be about 1% for a height of 1000 m. These resultants is confirmed by Yan *et al.*, (1991)

Hamdan and Rabbata, (2012) installed a prototype of solar chimney draft tower in AlAin in United Arab Emirates, which is 8 m high of chimney with 100 m² collector area and 0.75 m high in the centre, as shown in Fig. 2.2. Over the period of three days, the experimental data of the solar chimney were collected on 1st -3rd of December 2011. The air inlet temperature, air temperature before entering the chimney, the solar flux inside/outside the collector, and wind speed inside the chimney was measured that fully describe the performance of the solar chimney. An analytical model was presented and the mathematical equations were listed. The mathematical thermal model was created under the assumption of steady airflow with modified Bernoulli equation, buoyancy effect and ideal gas equation. The analytical model is effective tool to evaluate the influence of geometric parameters on the solar plant power generation. The experimental data and results of the analytical model were compared, and very good agreement is revealed from them. The conclusions that the chimney height, the collector radius, the solar irradiance, and the turbine pressure drop are essential parameters for the design and performance of solar chimneys.

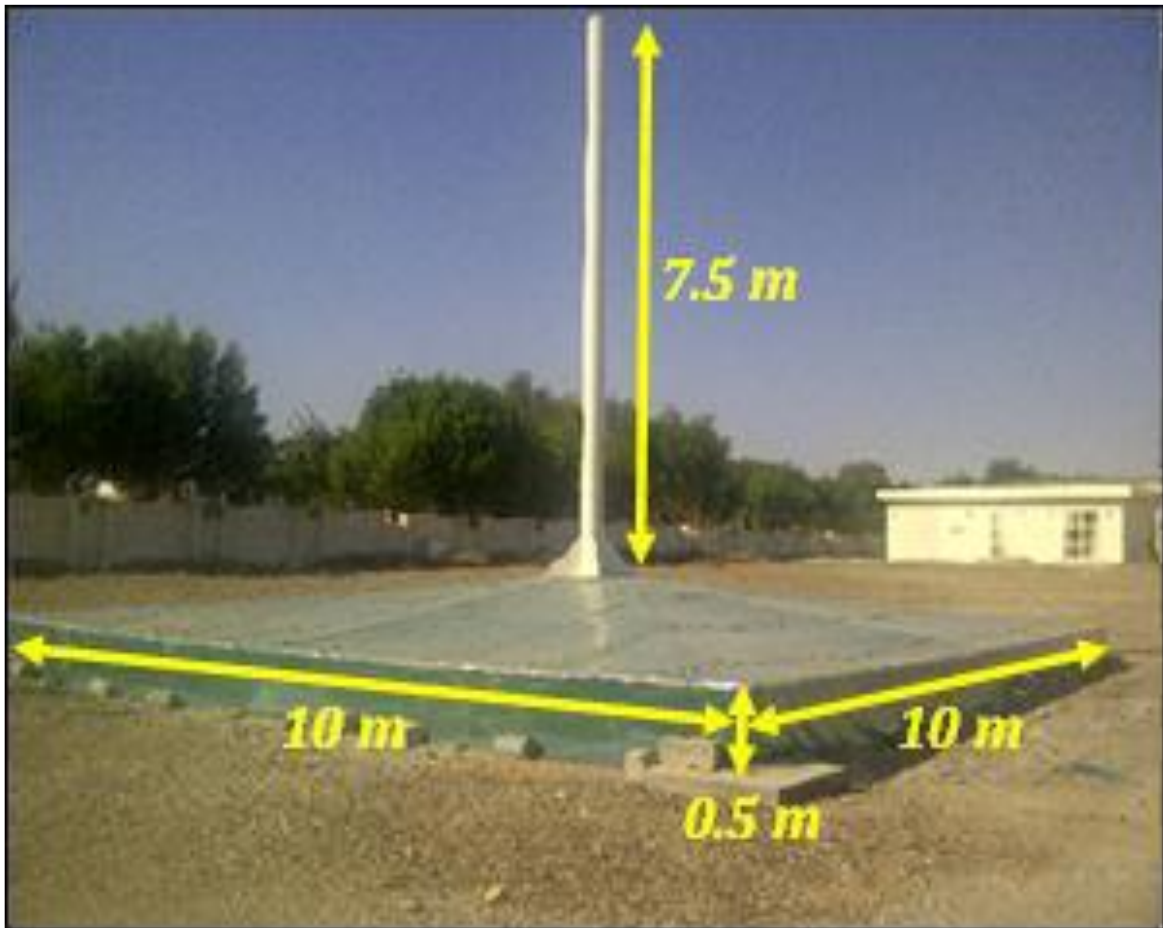


Fig. 2.2. pictures of solar chimney prototype with some dimensions at UAE University (Hamdan and Rabbata, 2012)

Koonsrisuk and Chitsomboon, (2013) developed a mathematical model of a solar collector, chimney, and turbine together. The theoretical model was solved by the iteration techniques to calculate produced power and pressure difference around the turbine. The validation of Results is carried out by comparing on the experimental results of the prototype from Manzanares. Moreover, the developed model is utilized to predict the performance characteristics of large-scale commercial solar chimneys, reveal the effect of pressure difference around the turbine, and find an important parameter for performance enhancement. The main aim of their study is prediction of dimensions of the most suitable plant, affordable by local government standards to respond to the electricity demand of a typical village in Thailand, is the one with a collector radius and chimney height of 200 m and 400 m, respectively. Furthermore, a conclusion that the optimum ratio between the turbine extraction pressure and the available driving pressure for the proposed plant is approximately 0.84. A simple method to evaluate the turbine power output for solar chimney systems is also proposed in the study using dimensional analysis.

Tingzhen et al., (2008) carried out numerical simulations of the solar chimney power plant systems coupled with turbine. The overall system of the SCPP has been divided into three regions: the collector, the chimney and the turbine. The governing equation of the heat transfer and flow were applied on these regions to form comprehensive the mathematical models, which solve by FLUENT. As a practical example, the numerical simulation results for Spanish prototype with a 3- blade turbine show that the maximum power output of the system is a little higher than 50 kW. In additionally, the effect of the turbine rotational speed on the chimney outlet parameters has been

analyzed that shows the validity of the numerical method advanced by the author. Thereafter, the developed model is used for designing and simulation of an MW-graded solar chimney power plant system with a chimney 400m in height and 30m in radius, collector 1500m in radius, and a 5-blade turbine, and the numerical simulation results show that the power output and turbine efficiency are 10MW and 50%, respectively. The conclusion that leads to the design of large-scale solar chimney power plant systems for more efficient production of the energy.

Muhammed and Atrooshi, (2019) applied computational fluid dynamics techniques to model the heat and transport relations in the collector and chimney area. The geometry, mesh layout and the existing analytical models are verified for consistency against the experimental data of the Manzanares plant in Spain. As one of the geometrical parameters such as collector diameter is changed, an optimization process occurs, leading to a decision on the best matching size for the other dimensions. The process checks the output against the optimized profiles of temperature, velocity, and pressure. Based on studying 180 cases in 15 groups for collector size against chimney height and diameter and another 130 cases in 12 groups for collector height, a table, and graphs of matching dimensions are obtained. As a consequence of this work, it is possible now to make a more accurate decision on consistent dimensions for a solar chimney plant.

Ahirwar and Sharma, (2019) performed a parametric 3D computational fluid dynamics (CFD) analysis of SCPP to observe the effects of chimney height, collector slope and chimney diverging angle on the performance of the Manzanares prototype. Numerical models were incorporated with solar load, DO (discrete ordinates) and RNG k- ϵ turbulence models. Firstly, CFD results were validated by comparing them with work of Hassan, Ali and Waqas, (2018). Several numerical simulations were performed on varying height of chimney, collector's slope and chimney diverging angles to improve the performance of solar chimney. Numerical simulations were performed at height of chimney $H=180\text{m}-210\text{m}$, chimney diverging angle = 20, 40, 60 and at collector slope = 20, 40, 60, 80 and 100 being all other parameters constant. It is seen that both velocity and temperature increase with increasing collector's slope due to enhanced heat transfer and mass flow rate. Higher collector slopes deteriorate the smooth airflow by developing vortices and recirculation of air, which obstructs the airflow and may reduce the overall performance. At height of 190m at 00 divergent angles 37.0840 kW power is received whereas at 190m and 20 divergent angles 71.5204 kW power is received with collector slope 40; therefore, this parameter of a solar chimney power plant is best.

2.2.2. Studies of greenhouse effect

Pasumarthi and Sherif, (1998) used experimental and mathematical model to study the effect of various parameters on the air temperature, air velocity, and power output of the solar chimney. Two experimental configurations were tried on the collector: increasing the collector base diameter and introducing an intermediate absorber. Enhancing the air temperature is resulted from the former modification, while the latter contributed to increasing the air temperature as well as the mass flow rate inside the chimney. Both enhancements helped to increase the overall chimney power output. Comparison Mathematical model results to published data of the solar chimney system built in Manzanares, Spain was achieved to validate the calculated results. Also, an economic assessment of the system costs are presented (Pasumarthi and Sherif, 1998b).

Kasaeian, Heidari and Vatan, (2011) developed a solar chimney pilot power plant with 10 m collector diameter and 12 m chimney height, after designing and installing, measured the

temperatures and air velocities inside the SCPP. The temperature and velocity readings were measured for some specified diameter of collector and chimney with varying weather condition in different days. Because of greenhouse effect happened under the collector, the temperature difference between the exit of collector and the ambient reached to 25 °C. The increasing in air temperature under canopy derived air flow from collector to the chimney. The air velocity increase with increasing solar radiation on both cold and hot days from a minimum point and after a while, it is broken by the collector warm-up. After the breaking of the increasing in air velocity, a steady air flow inside the chimney would appear. The maximum air velocity of 2.9 m/s was achieved inside the chimney, while the collector entrance velocity was around zero. The maximum chimney temperatures were recorded at the time between 1:30 p.m. and 2:30 p.m. (maximum temperature: 60 °C at the ambient temperature of 34 °C).

Li, Guo and Wang,(2012) developed a comprehensive theoretical model for the performance evaluation of a solar chimney power plant (SCPP), and the validation of the presented model was done by comparing with the experimental data of the Spanish prototype. This mathematical model takes account of the temperature lapse rates inside and outside the chimney, thermal equilibrium equations in the collector, the system driving force and the flow losses. Under a given solar radiation condition, a maximum power output for an SCPP has been limited due to thermal and flow losses and the pressure drop of the turbines. So, increasing the output power production could be achieved by expanding the dimensions of the SCPP. However, the conclusion that a limitation on the maximum collector radius exists for the maximum attainable power of the SCPP, which shown in Fig. 2.3. Variation of power output versus collector radius of the SCPPs with a constant chimney height of 194.6 m(Li, Guo and Wang, 2012); whereas, no such limitation exists for chimney height in terms of contemporary construction technology, as shown in Fig. 2.4. Variation of power output versus chimney height of the SCPPs with a constant collector radius of 122.0 m(Li, Guo and Wang, 2012)

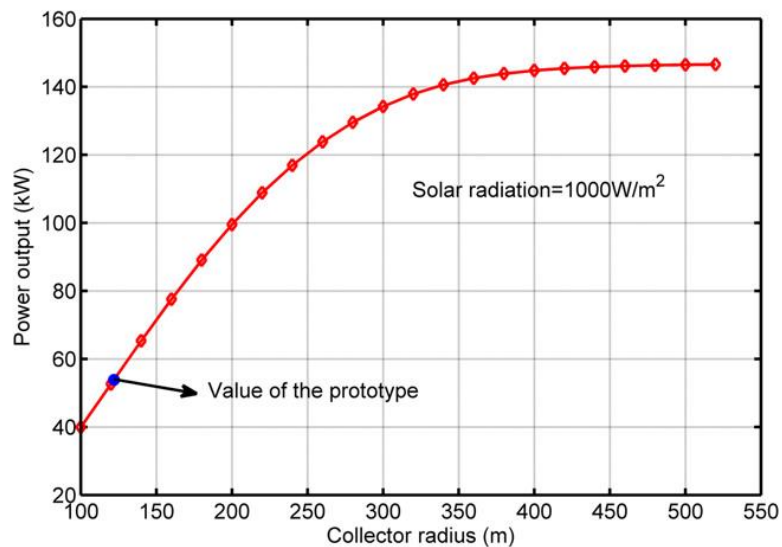


Fig. 2.3. Variation of power output versus collector radius of the SCPPs with a constant chimney height of 194.6 m(Li, Guo and Wang, 2012)

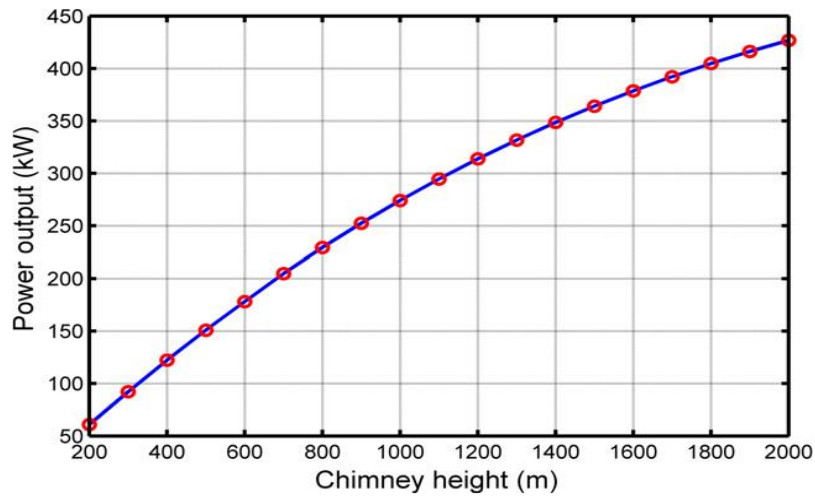


Fig. 2.4. Variation of power output versus chimney height of the SCPPs with a constant collector radius of 122.0 m(Li, Guo and Wang, 2012)

Patel, Prasad and Ahmed, (2014) Study the optimization a geometry of the major components of the SCPP using a computational fluid dynamics (CFD) technique software ANSYS-CFX to investigate and improve the flow characteristics inside the SCPP. The overall chimney height and the collector diameter of the SCPP were kept constant at 10 m and 8 m respectively. The collector outlet diameter was also varied from 0.6 m to 1 m. The collector inlet opening was varied from 0.05 m to 0.2 m. These modified collectors were tested with chimneys of different divergence angles (0° – 3°) and also different chimney inlet openings of 0.6 m to 1 m, as shown in Fig. 2.5. The diameter of the chimney was also varied from 0.25 m to 0.3 m. Based on the CFX computational results, the best configuration was achieved using the chimney with a divergence angle of 2° and chimney diameter of 0.25 m together with the collector opening of 0.05 m and collector outlet diameter of 1 m. The temperature inside the collector is higher for the lower opening resulting in a higher flow rate and power.

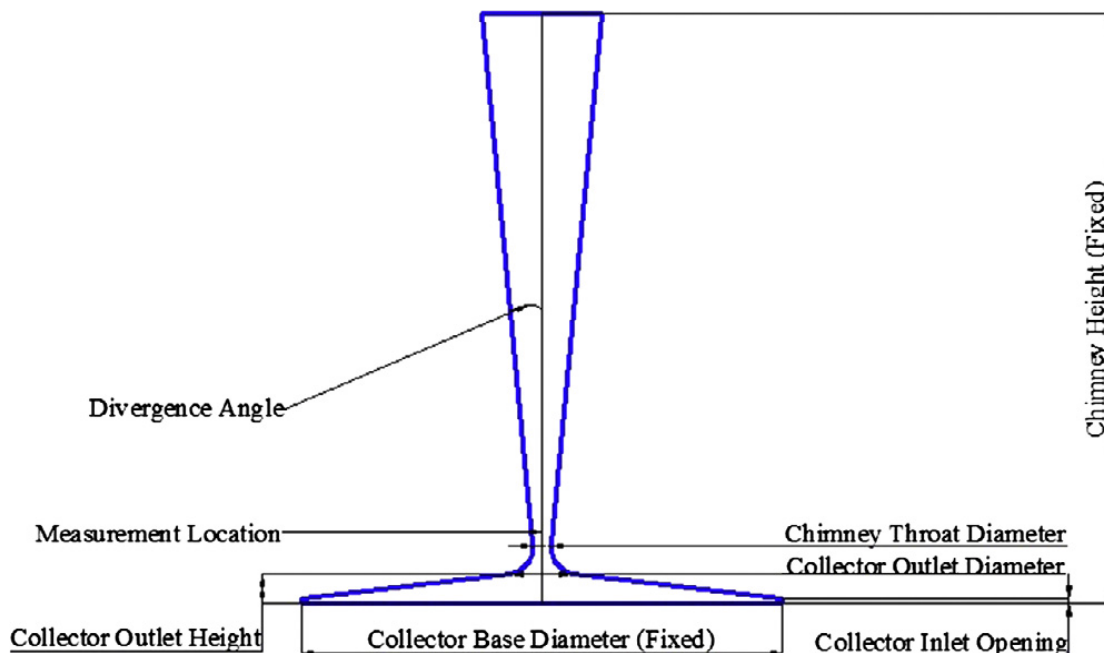


Fig. 2.5. Diagram of the SCPP with the various parameters that are studied(Patel, Prasad and Ahmed, 2014)

Elkady *et al.*, (2019) installed an experimental set-up model of SCPP with a variation of two geometrical parameters (chimney height, H and collector inlet height, h). The model collector radius, R is fixed at 1 m. The chimney diameter, d is fixed at 0.2 m and its height, H was varied from 2 m to 4 m. The collector inlet height, h was varied from 0.04 m to 0.08 m, as shown Fig. 2.6. Air velocity and temperature variation with time at chimney inlet have been measured as well as in canopy. The results show that the collector inlet height, h of 0.04 m and the chimney height, H of 4 m providing an optimum configuration for the constructed solar chimney model. The velocity and temperature profiles in the chimney were modelled by CFD analysis based on the same model dimensions. The CFD simulation was compared with the experimental data of the solar chimney model and a good agreement is noticed.

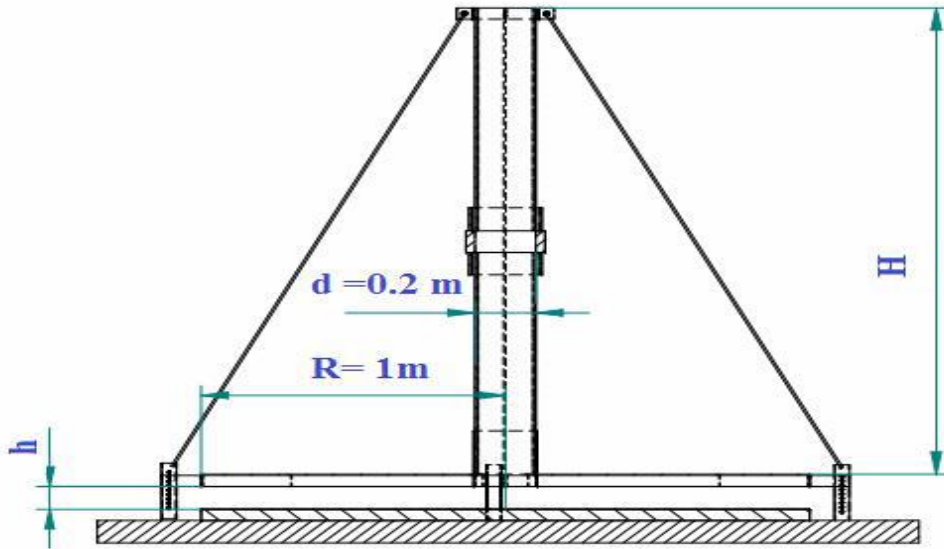


Fig. 2.6. Schematic diagram of solar chimney test rig of Elkady *et al.*, (2019)

In collector, there can be natural and artificial roughness such as the surface of the earth and the energy storage system. Fallah and Valipour, (2019) investigated the performance of SCPP with and without artificial roughness for the weather of Semnan by a three-dimensional simulation. Also, the dimensions of the Manzanares power plant were considered and the simulated without roughness, then simulation results were validated based on it. Results reveal that Semnan (53.23°E , 35.34°N), has a good potential for using SCPP. Without roughness, the maximum power of SCPP was 50.81 kW. The conclusion that the artificial roughness in SCPP improves heat transfer, but reduces velocity; therefore, there is an optimal dimension and location for it. Geometrically, the location of this roughness near the collector entrance has a better performance than other locations, but this change of locations has little impact on the performance of SCPP.

2.2.3. Hybrid solar chimney

Solar chimney system has low thermal efficiency because of converting solar thermal energy to air pressure inside its collector. One of methods that enhance systems productivity in combination with a photovoltaic (PV) system to increase the system total electricity production. Kiwan, Al-Nimr and Salim, (2020) Present two modifications of the solar chimney system by adding a photovoltaic (PV) system, and the installation of a water pool to cool the PV panels and to allow the system to generate freshwater. They develop a mathematical model to test the feasibility of both the conventional and changed systems. It is found that the total system utilization factor for the conventional system is 0.51%, while the utilization factor for the changed system is 4.37%.

Parametric analysis is conducted to determine the variables that lead to the best utilization factor. The best results are achieved when the submerged PV panels are closer to the chimney. They test the performance of the system, taking into account the weather data of a location in the country of Jordan. The results showed that the proposed system produces 45.35% more electricity annually than a standalone PV system installed in the same location. The sensitivity analysis conducted shows that the chimney height is the most significant variable influences the system utilization factor. The higher the chimney, the higher the utilization factor. Finally, the economic analysis concludes that the cost of freshwater produced by the system is 1.60 US\$ per cubic meter, which is 46.3% cheaper than what it produces using other similar systems. Also, the economic indices of the proposed system show an improvement from that for the conventional solar chimney.

Ahmed *et al.*, (2020) integrated solar chimneys and solar cells in a hybrid system to achieve the desired goal of increasing the production of electric power. A pragmatic model of the Hybrid Solar Chimney framework was worked to examine the warm and electrical execution of the Solar Chimney. The Solar cell was utilized as a retentive dark surface for the base of the Solar Chimney. The study demonstrated that the warm effectiveness of the half breed PV/Solar Chimney framework was moderately high about (91%) in view of the nearness of glass spread, which does not permit the exit of daylight falling on the Solar authority, which prompts a higher temperature around 67 C. Also, the obtained data showed that the total electrical efficiency of the system is about (10.5%). Moreover, the collector inclination angle has an essential effect on the performance of the system, and the 45° angle was the best angle of performance for the angle values taken (30°, 35°, and 45°).

Haghighat *et al.*, (2019) designed a new model of hybrid PV panels and solar chimneys, which uses the airflow created below the collector of solar chimney for cooling of the PV panels. The dissipated thermal energy of the PV panels is used for heating the air under the collector. In this modelling, two main factors as the location and width of the PV panels in the solar chimney were investigated. Modelling was performed for four different modes of combining the hybrid PV panels, as shown in Fig. 2.7 and solar chimney in three different widths of 70, 50, 30 cm for all four modes. The best result was obtained for the hybrid of PV panels and solar chimney for placing 50 cm wide PV s, instead of a transparent collector. In this case, the average PV panels temperature was 5 °C lower than the average PV panels temperature of the non-hybrid mode of solar chimney. This decrease in temperature would increase the efficiency of the PV panels by 1%. Furthermore, in this mode, the maximum flow velocity shows 0.2 m/s reduction in comparison to the transparent collector.

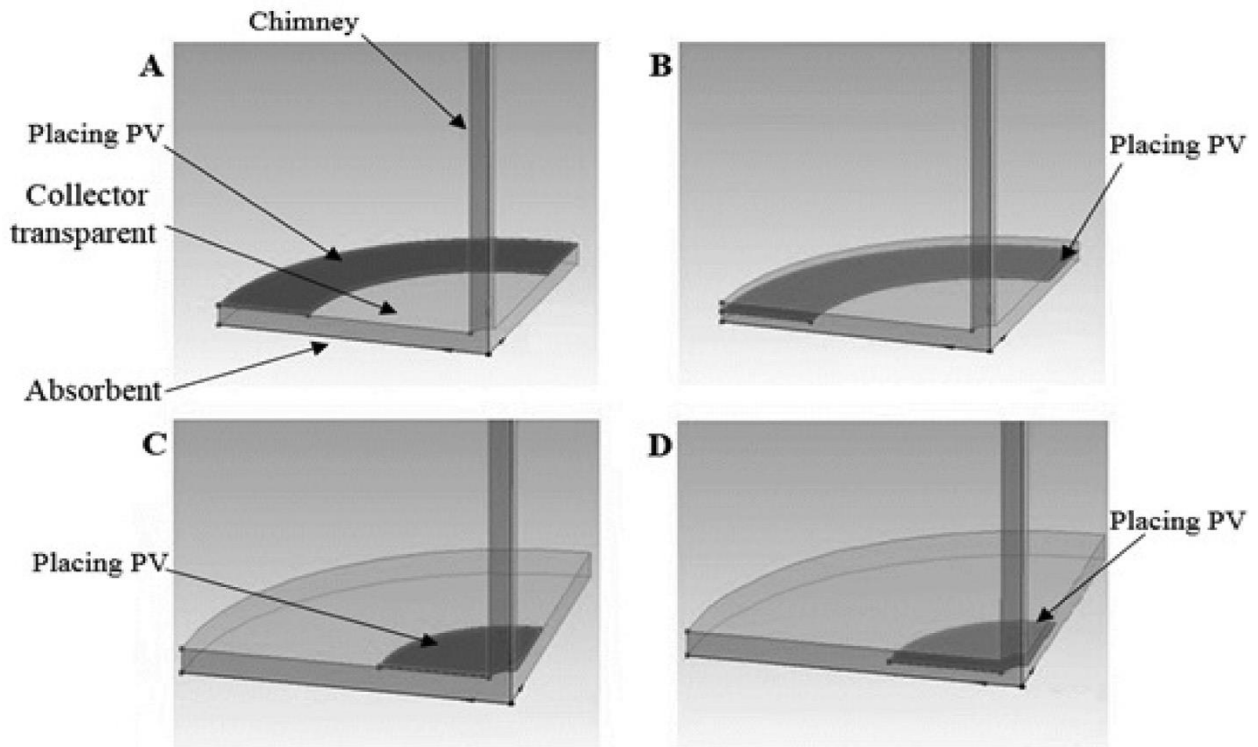


Fig. 2.7. Placing of PV panels in a solar chimney at four different positions A, B, C, D (Haghighat *et al.*, 2019)

Due to the low efficiency of the solar chimney in the night times, other researcher develop the solar chimney with external source of heat to improve its performance at the night. Tian *et al.*, (2020) proposed new configuration of SCPP by considering the solid oxide fuel cell and solid oxide electrolysis cell for storing the surplus energy as Hydrogen for the night times. They also present a developed version of deer hunting optimization algorithm to optimal designing of the economic aspect of the power plant. Simulation results are applied to two different seasons for more analysis and the results of the optimal system are compared with genetic algorithm and particle swarm optimization algorithm to show the system efficiency. The results showed that 0.16 kg/s hydrogen is produced at the peak of the radiation in a district of Yazd city. The results also show the decreasing the loss value based on optimal economical designing gives 1,192,000,000\$, 1,190,000,000\$, and 8,645,000,000\$ cost for two algorithms, and the proposed improved deer hunting optimization algorithm, respectively. It also shows that the energy generated by the presented configuration in the summer is higher than the winter.

Al-Kayiem *et al.*, (2019) proposed a hybrid solar chimney integrated with an external heat source to complement solar energy for uninterrupted power generation. Flue-gas channels were utilized to supply air into the collector passage, as show in Fig. 2.8. The hybrid arrangement was investigated experimentally and numerically. An experimental model comprising a 6 m-diameter solar air collector, 6.65 m-height chimney, and four flue thermal channels was designed and fabricated. The hybrid system was further simulated using ANSYS-Fluent. The numerical procedure was validated by comparing with experimental measurements for a conventional solar chimney with mean differences of 8.7% and 7.8% in air flow velocity and air temperature rise, respectively. Results showed that the hybrid approach considerably enhanced the plant performance. The insertion of flue channels, even with no flue-gas flow, enhanced the velocity and temperature by 6.87% and 6.3%, respectively measured at the chimney base. Simulation

results with 0.0015 kg/s at 116 °C flue gas in the thermal channels demonstrated that the air-mass flow rate and collector efficiency enhanced by 12.0%, and 64.0%, respectively. This study proved that the proposed technique can resolve the setback of night operation of solar chimney power plants and enable 24/7 power production.

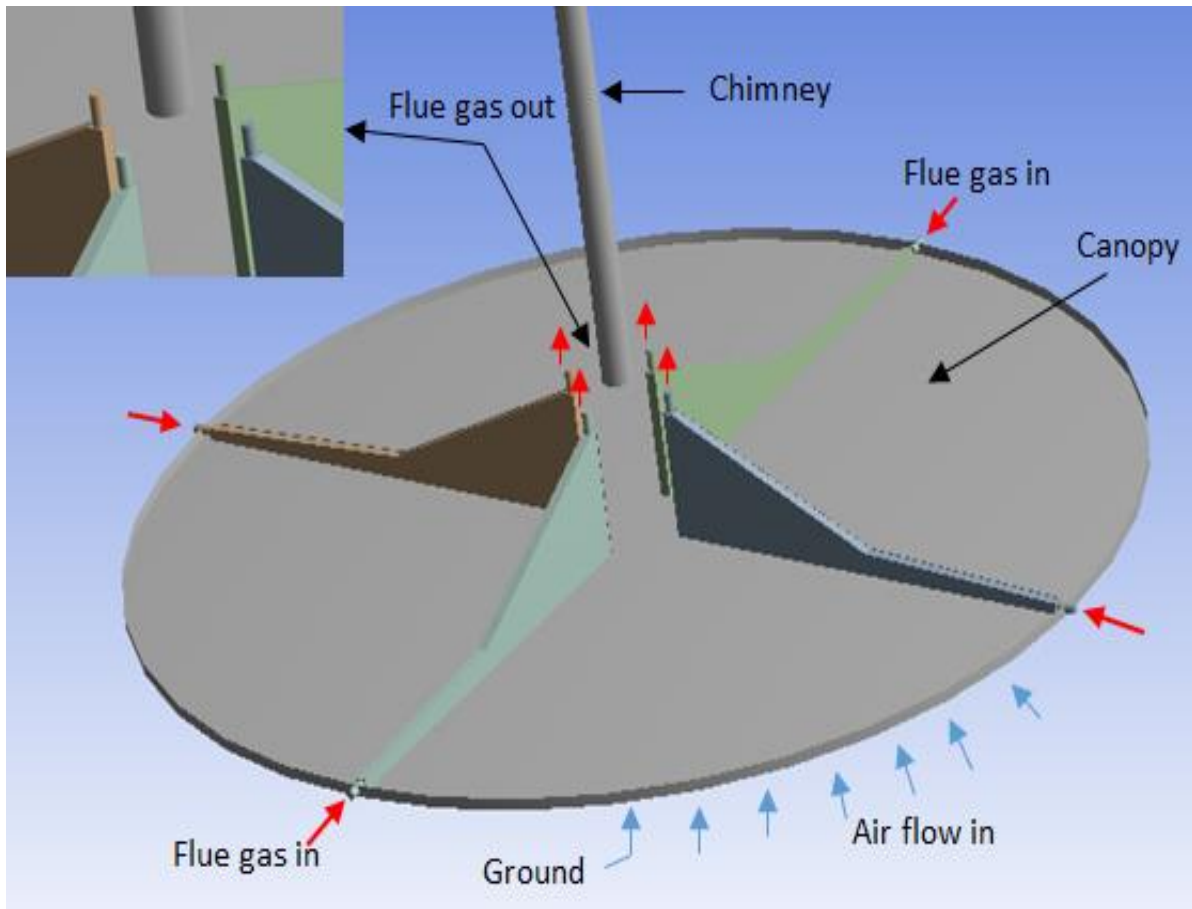


Fig. 2.8. Layout of the proposed hybrid solar chimney model by Al-Kayiem *et al.*, (2019)

Because the solar chimney system is convenient in dry weather, combining it with water desalination is a great idea to make sustainability development of the desert zone. Zuo *et al.*, (2011) demonstrate that solar chimneys can be incorporated into sea-water desalination systems, primarily attempting to increase the low productivity of solar systems. The authors proposed an integrated system, composed primarily of a chimney, a collector, a turbine, an energy storage layer, and a basin solar still. The structure of the chimney, collector, and turbine is not much different from that of a solar chimney power plant, as shown in Fig. 2.9 . The energy storage layer and the basin solar still are located below the energy collector. A rock energy layer works as an absorber bed. The incident solar radiation is transmitted to the still, and the major part of this energy is absorbed by the seawater surface. The seawater is therefore heated and evaporates, and it is later condensed on the inner surface of the glass cover. After that, it is collected as freshwater. Two mathematical models were developed, one for the solar chimney and one for the integrated system, considering prescribed conditions of solar radiation and ambient temperature. The system has a chimney of 200m height and 10-m diameter, a collector of 250 m diameter and 2 m height, and a storage layer of 40-m diameter. For 6 h of running time, it was estimated an annual power output of 2.83×10^5 kWh, an annual fresh water productivity of approximately 69,500 ton, with a price of fresh water of 2.65 euros/m³. For 7 h and 8 h running times, the power output and the fresh water productivity increase and the fresh water price decreases.

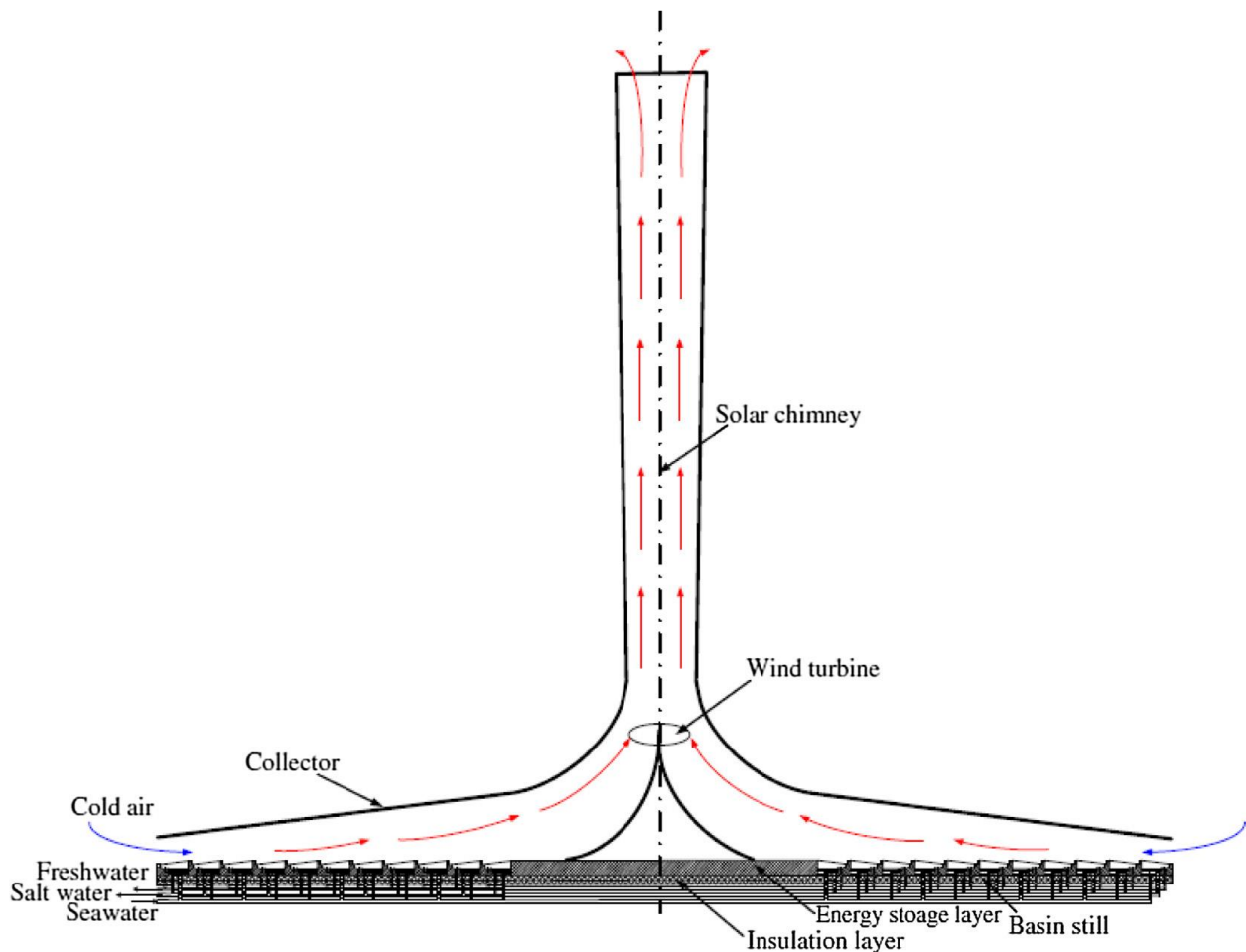


Fig. 2.9. Schematic diagram of the integrated system from Zuo *et al.*, (2011)

Another approach of combination SCPP and water desalination was proposed by Ming *et al.*, (2016) by replacing the greenhouse canopy by black tubes filled with hot water to warm the inlet air and to keep the relative humidity identical to ambient, as shown in Fig. 2.10. The device uses the same principle as the formation of clouds. Buoyance forces induce a hot airflow. As the air rises, the temperature decreases, and the relative humidity decreases. As the chimney is high enough, the air reaches the dew point and the water vapor condenses onto a solid surface and is collected as potable water. A wind turbine is installed at the top opening of the whole and extracts work from the ascending airflow. The black tubes used instead of a collector act as a solar collector and store thermal energy. A mathematical model was developed to evaluate the effectiveness of the structure in comparison to natural precipitation in nine cities in China. Hypothetic solar chimney with a chimney radius of 50m and a height of 3000 m was modelled. A 24 h of running time was assumed, with a water collecting mechanism 100% efficient. The authors concluded that the efficiency of the modified solar chimney is inversely proportional to the natural rainfall. Under favourable conditions, the amount of potable water produced is remarkable and might be able to benefit several millions of people. The performance of the device was not completely understood (Ming *et al.*, 2017).

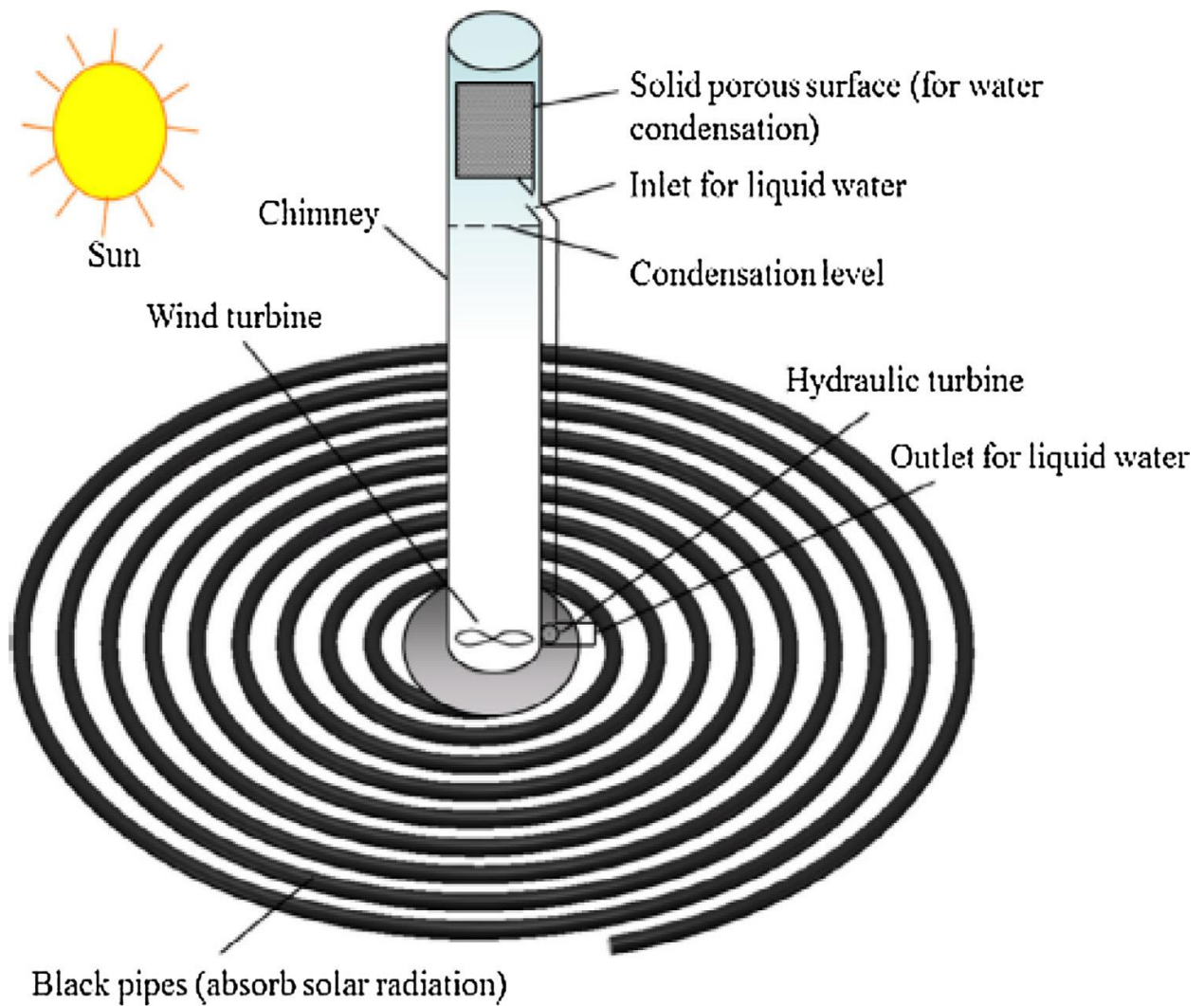


Fig. 2.10. Schematics of the system proposed by Ming *et al.*, (2016)

Zuo *et al.*, (2019) improved the original design to include indirect condensation freshwater production. A condenser positioned below the wind turbine preheats the seawater, as shown in Fig. 2.11, which absorbs the condensation latent heat of vapor in the hot airflow, improving the system performance. A numerical simulation of a solar chimney power plant, a solar chimney power plant combined with seawater desalination by indirect condensation freshwater production and a wind supercharged solar chimney power plant combined with seawater desalination by indirect condensation freshwater production was performed, and the results of these systems were compared to the flow field characteristics. The main conclusions were that the condenser made full use of the condensation latent heat released by water vapor and the wind pressure ventilate or significantly increased the electricity production.

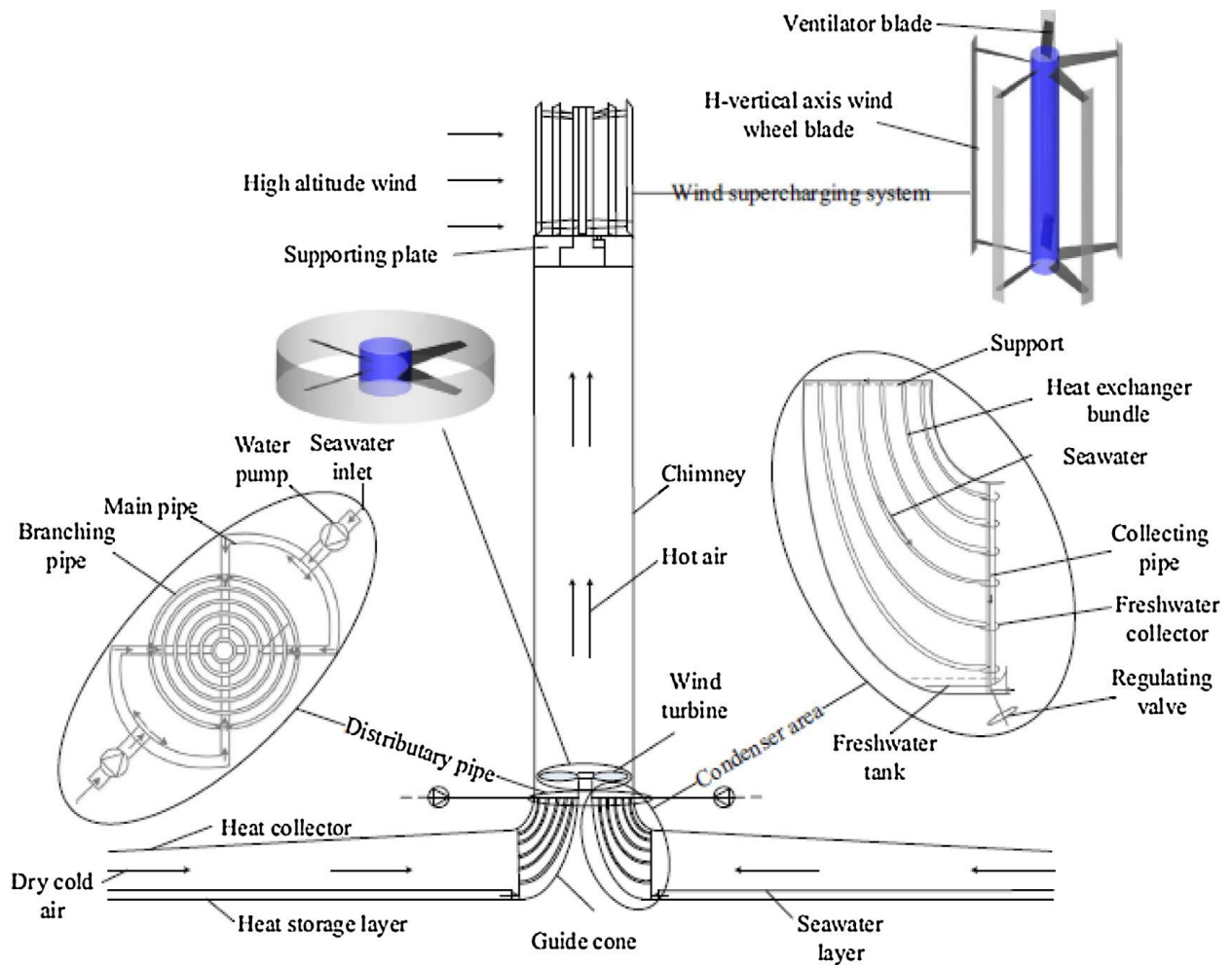


Fig. 2.11. Schematics of the system proposed by Zuo *et al.*, (2019)

Cirillo *et al.*, (2015) proposed the ventilation system approaching and presented a numerical and experimental investigation on a prototypal solar chimney system integrated in a south facade of a building. The chimney consists of a converging channel with one vertical wall and one inclined. The numerical analysis is carried out on a three-dimensional model in airflow and the governing equations are given in terms of $k-\epsilon$ turbulence model. The problem is solved by means of the commercial code Ansys-Fluent. The numerical analysis was intended to examine the effect of the solar chimney's stack height and depth. Results are given in terms of wall temperature distributions, air velocity and temperature fields and transversal profiles for a uniform wall heat flux on the vertical wall. Thermal and fluid dynamics behaviours are evaluated in order to have some indications to improve the energy conversion system. Furthermore, the results of an experimental investigation on a chimney system 4.0 m high and 1.5 m wide are given. The air velocity in the channel and the surface temperature on the heated wall are presented.

2.3. Approach of a turbine for solar chimney power plant

The turbine of the solar chimney is a key component of the SCPP plant as it extracts the kinetic energy from the air and transmits it to the generator. It has a significant influence on the plant as the turbine pressure drop and plant mass flow rate are coupled. The specifications for solar chimney turbines are in many aspects similar to those ones for large wind turbines. The solar chimney turbine and traditional wind turbines both convert large amounts of kinetic energy in the airflow at low temperature to mechanical energy. However, there are also various important

differences. The following characteristic is typical for solar chimney turbines in contrast to wind turbines.

The solar chimney turbine acquires enormous importance from its task in the SSCP plant, the turbine causes a pressure drop and dominates the mass flow rate; these two factors have a significant influence on the plant. Nizetic and Klarin, (2010) used a simplified analytical approach, which is a real air cycle to obtain the range of pressure drop ratio in turbines of 0.8–0.9 as the optimum value. Zhou and Xu, (2016) summarize the Literature of a pressure drop around the turbine in range 16/27(Betz Limit) to 0.9 to obtain the maximum performance of SSCP. On the other hand, Guo *et al.*, (2013) found the optimum pressure drop ratio in turbines is a function of the intensity of solar radiation. They investigated the SSCP performance using theoretical analysis and 3D numerical simulations within the actuator disk model in ANSYS Fluent package.

Various layouts were proposed for turbines of the solar chimney that shown by Zhou, Wang and Ochieng, (2010). However, all configuration of solar chimney turbine is of the axial flow type. Fig. 2.12 show the turbine configurations include the single vertical axis, the multiple vertical axis, and the multiple horizontal axis turbine layouts with or without inlet guide fan. The solar chimney turbine has characteristics between those of wind turbines and gas turbines: it has more blades than the typical two or three of wind turbines, but not as many as gas turbines. The rotor blades may be adjustable, like those of wind turbines, but as in gas turbines, the flow is enclosed, and some of the solar chimney turbines may have radial vanes of inflow inlet guide (von Backström and Gannon, 2004).

On other hands, the turbines of SSCP are ducted, and their maximum theoretically achievable total-to-total efficiency is therefore 100% the Betz-limit, which is applicable to ducted ones. The direction of the oncoming air flow is known and remains constant. The turbines are protected from harsh weather conditions but have to cope with higher temperatures. The large volumes of collector and chimney act as a buffer preventing large fluctuations in air flow speed, i.e. dynamic loads on the turbine blades and all the other rotating components are comparably low as compare with the gas turbine loads. Furthermore, the turbine pressure drop in SCCPs is about 10 times bigger than in wind turbines(Von Backström et al., 2008).

Later, Zuo *et al.*, (2018) developed a 3D numerical analysis of the airflow inside a wind supercharged solar chimney power plant combined with seawater desalination to evaluate the influence of structural parameters on the system performance. The evaluated parameters were turbine structure parameters, shape of the turbine guide (guide cone or guide vane – see Fig. 2.13) and wind pressure ventilator parameters. The authors concluded that an increase in the turbine blade number increased the maximum temperature difference and decrease the mass flow rate and the freshwater productivity. According to the authors, it is reasonable to choose four or five-blade turbine based on system output and the cost of blades. The guide vane can significantly reduce the rotation effect of the airflow after the turbine, increasing the freshwater productivity and the shaft power of the system. The guide cone increases the turbine efficiency and slightly decrease the mass flow rate and freshwater productivity.

2.4. Designs for a turbine for solar chimney power plant

In 1981, Schwarz and Knauss designed the turbo generator for the pilot plant in Manzanares. For this purpose, a single vertical axis turbine layout without inlet guide vanes was used (Fluri and von Backström, 2008). Gannon and Von Backström, (2002) proposed a single rotor layout for a

large-scale solar chimney with inlet guide vanes. A three-step turbine design method which is adapted from gas turbine literature is presented. Firstly, the major turbine dimensions are calculated by using a free vortex analysis method. Secondly, a matrix throughflow method predicts the air flow path through the inlet guide vanes and rotor. Finally, the blade profiles are designed using an optimization code coupled to a surface vortex method to determine turbine blades of a minimum chord and low drag. The proposed turbine design can extract over 80% of the power available in the flow (Gannon and Von Backström, 2002b).

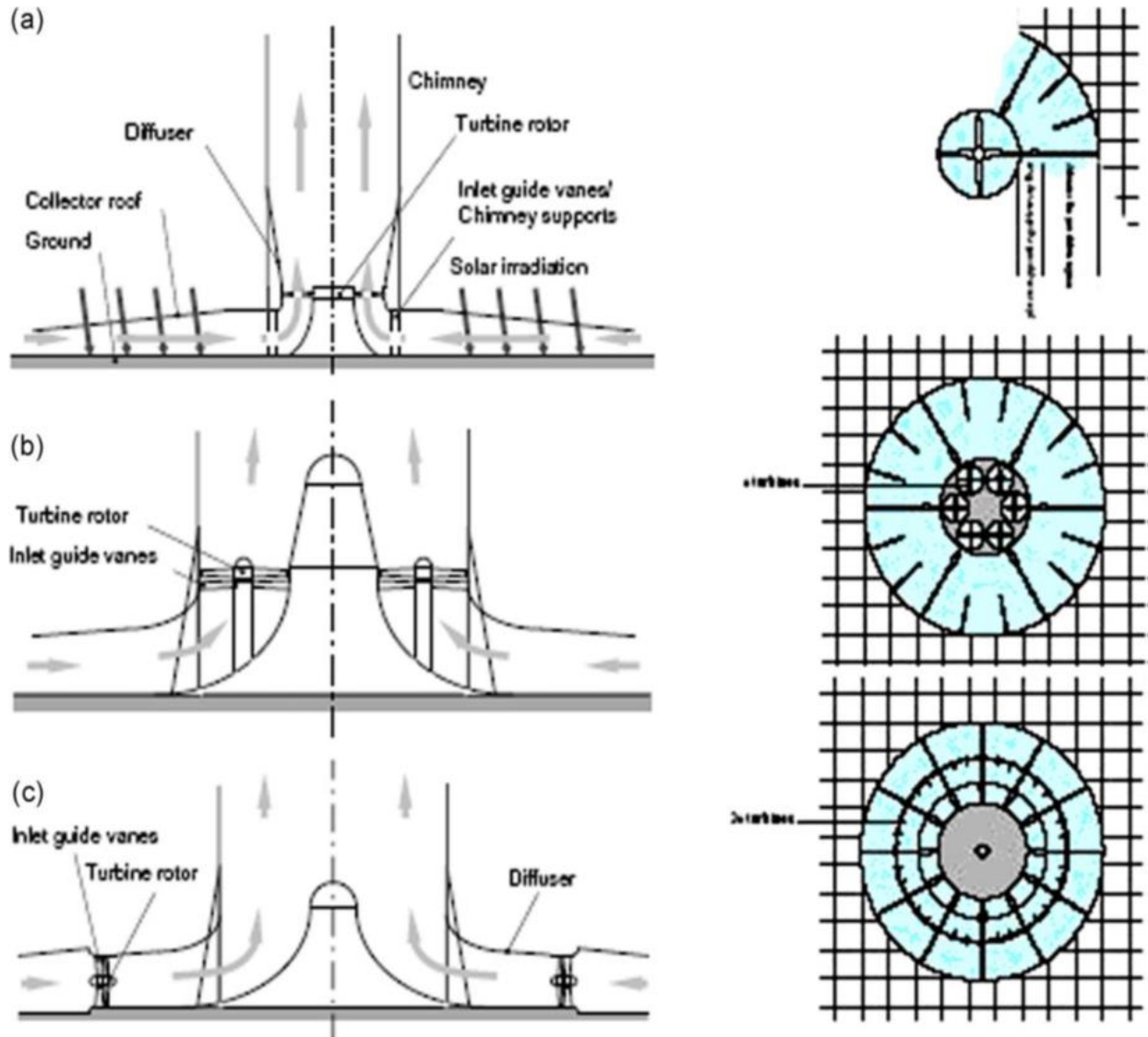


Fig. 2.12. Elevation view and top view of three turbine configurations: (a) single vertical axis type; (b) multiple vertical axis type; (c) multiple horizontal axis type (Dhahri and Omri, 2013)

2.4.1. Free vortex theory design

von Backström and Gannon, (2004) presented analytical equations in angle of turbine flow, degree of reaction, flow and load coefficient, this aims to reveal the influence of each coefficient on turbine efficiency. The analytical solutions find optimum degree of reaction, maximum turbine efficiency for required power and maximum efficiency for constrained turbine size. The characteristics of a 720 mm diameter turbine model is measured for validation the analytical model result. Application to a proposed large solar chimney plant indicates that a peak turbine total-to-total efficiency of around 90% is attainable, but not necessarily over the full range of plant

operating points. They also point out that the values for specific speed and diameter for a solar chimney turbine lie between the ones of gas turbines and wind turbines.

Denantes and Bilgen, (2006) combined a thermodynamic model for a solar chimney system and a solar radiation model, annual energy output of solar chimney systems to develop an efficient model for counter-rotating turbines. Two counter rotating turbines, one with inlet guide vanes, the other without, are presented and compared its performance to a single-runner system. The design and off-design performances are weighed against in three different solar chimney plant sizes. They conclude that the counter-rotating turbines without guide vanes have lower design efficiency and a higher off-design performance than a single-runner turbine. Based on the output torque versus power for various turbine layouts, advantageous operational conditions of counter rotating turbines are demonstrated.

Fluri and von Backström, (2008) compared the performance of various layouts for the turbo generator proposed in the previous researchers using analytical models and optimization techniques, and discussed the important design parameters. The turbine layouts under consideration are single rotor and counter rotating turbines, both with or without inlet guide vanes. Furthermore, a limit to the degree of reaction of the turbine has been introduced to avoid diffusion at the hub. They show that these slight changes in modelling approach have a significant impact on the performance prediction. Further conclusions that the single rotor layout without guide vanes performs very poorly; the efficiency of the other three layouts is much better and lies in a narrow band. The counter rotating layouts provide the highest peak efficiencies, but at relatively low speeds, which leads to an undesirable higher torque for the same power output.

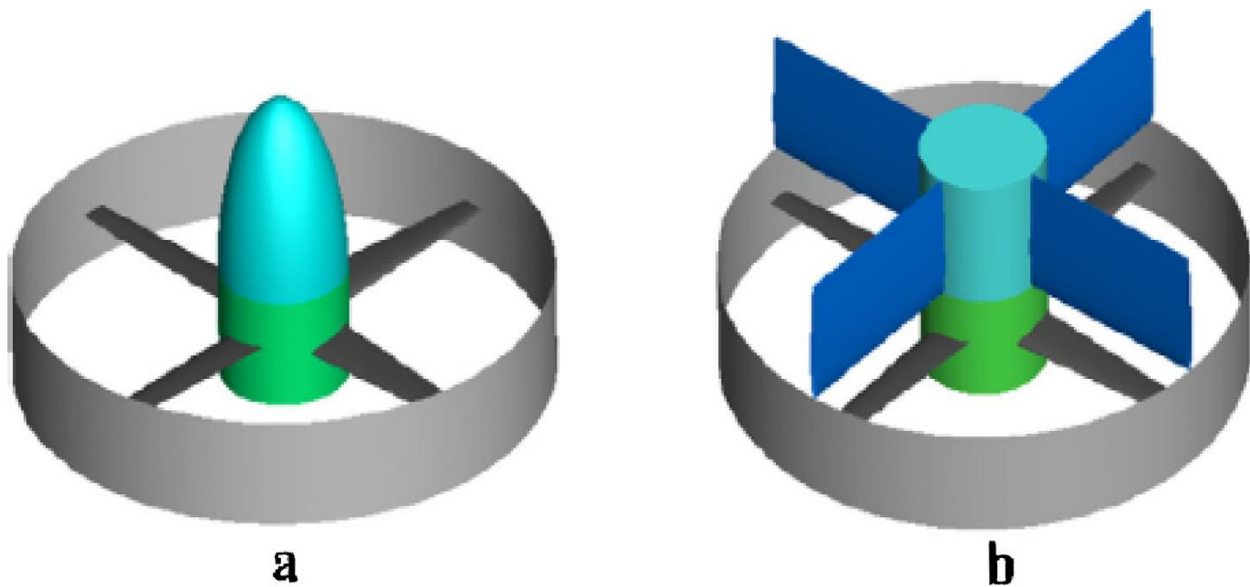


Fig. 2.13. Three-dimensional models of the guide cone and guide vane (Zuo et al., 2018)

2.4.2. Blade element theory design

Zhou *et al.*, (2016) designed a turbine applied to solar chimney power plant with a vertical collector, Based on the design theory of the wind turbine (BET). The NACA63-215 airfoil is chosen as the airfoil of the blade design, and Wilson design theory is adapted to solve parameters of each blade airfoil section. The performance of the wind turbine is measured by wind tunnel test, which is compared with the design power. The results point out that the experimental performance

is consistent with the designed performance. Then the number of blades and tip speed ratio are conducted, through the experimental method, the conclusion is the optimum blade number is 6, the optimum tip speed ratio is 1.9.

2.5. Aerodynamics of shrouded wind turbine

Recently, the development of wind turbines has been the focus of many researchers. A shrouded wind turbine is one of the improvements, which helps to increase the power coefficient of the wind turbine by surrounding a rotor of the wind turbine into the duct. The researcher aimed to modify the classic approach. Consequently, the design theory takes into account the effect of the surrounding duct that makes the shape of the blade more suitable for the surrounding duct and produces more output power in the same diameter. The new produced approach is nearly close to a case of the solar chimney. In this work, the shrouded wind turbine theory is used to design solar chimney turbine. The following section of the literature review surveys some of the research related to the shrouded wind turbine.

2.5.1. Studies shape duct and its effect

Igra, (1985) suggested that the wind turbine should be surrounded inside a specially designed shroud to take advantage of wind power as economically as possible. Various geometries of the shroud were studied that resulted from a significant power augmentation with using a fairly compact shroud. The use of a ring-shaped flap or boundary layer control technique was presented for improving the shroud performance, by using this technique lead up to 80% improvement in the shroud power augmentation. However, using proper bleeding of the shroud's external flow into its inner rear zone increased produced power augmentation by about 25%. Additionally, the design and performance of an axial flow turbine was presented and was the most suitable for the proposed shrouds. Based on the reported research with shrouds, a pilot plant producing 0.7457 kW at 5 m/s with a 3 m diameter. The designed turbine produced a fairly stable output for varying wind speeds while exhibiting a fairly high efficiency.

Gilbert and Foreman, (1983) developed the experimental prototype of the diffuser-augmented wind turbine (DAWT) without screen meshes. The prototype consists of a three-bladed constant chord, untwisted turbine model incorporated into a DAWT model, as shown in Fig. 2.14, which is tested in a 2 X 3 m wind tunnel. The real turbine characteristics of the DAWT are studied such as swirl, and centre body effects to the flow. The only turbine was also test to compare the performance with the ducted one, then demonstrate the gain of surrounding diffuser duct. The result showed that the model DAWT system increased the power output by more than 3.4 times that of the model turbine operating as a conventional wind energy conversion system(Gilbert and Foreman, 1979).

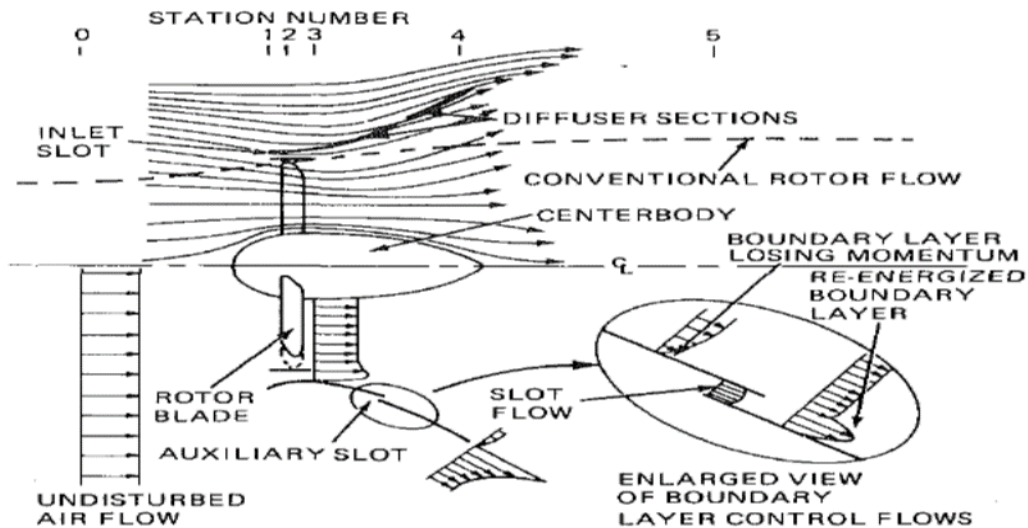


Fig. 2.14. Schematic of flow field for baseline DAWT configuration (Gilbert and Foreman, 1979)

Ohya et al. (2008) developed a new wind turbine system, which consists of a wind turbine rotor surrounded by a diffuser shroud with a broad-ring flange at the exit periphery. Fig. 2.15 is shown the developed system. The flange generates a low-pressure region in the exit neighbourhood of the diffuser by vortex formation and draws more mass flow to the wind turbine inside the diffuser shroud. As a result of that, the air flow is collected and accelerated by using the flanged-diffuser shroud to produce a higher power output of the shrouded wind turbine. The positioning the flange at the exit of a diffuser shroud is an essential parameter affect the performance of the wind turbine system. In addition to, the optimal shape of the flanged diffuser is studied by varying the diffuser open angle, flange height, hub ratio, centre body length, inlet shroud shape. A prototype wind turbine with a flanged diffuser shroud is tested in a field experiment and wind tunnel experiment. The performance output of the wind turbine with a flanged diffuser shroud agrees with expectation and produce about 4–5 times power compared to a standard (bare) wind turbine at same turbine diameter and wind speed.

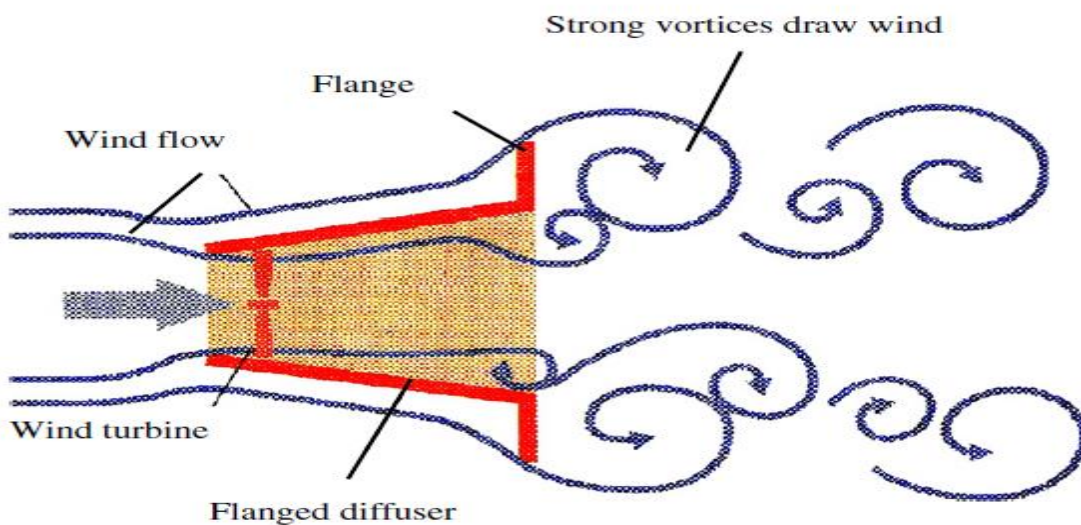


Fig. 2.15. Schematic view of a diffuser shroud with a broad-ring flange at the exit periphery (Ohya et al., 2008)

Hjort and Larsen, (2014) presented a new approach of diffuser augmented wind turbines (DAWTs). The new concept of the diffuser takes advantage of an aerodynamic principle for the creation of high-lift airfoil configurations that famous in the aircraft industry. The main objective of the developed approach obtains a compact power-efficient design of the DAWT, which capture energy potentials to exceed the power efficiency by 50% based on the diffuser exit area. The 1D momentum theory governing the DAWTs is presented and discusses upper limits for power extraction, similarity, the Betz limit that applies for bare Horizontal-Axis Wind Turbines (HAWTs). The inviscid axisymmetric panel code is used to drive the diffuser design towards higher power coefficients. The types of the stall are shown by the calculations of axisymmetric actuator disk Navier-Stokes. Unfortunately, the stall inhibits the functionality of the ideal inviscid optimum but leading the design towards the more improvement of DAWTs. The experimental of new DAWT performance are carried over time and creating confusion. The comparison with the performance of existing DAWTs designs is therefore emphasized that is ensured 50% higher than present state-of-the-art for any HAWTs or DAWTs.

2.5.2. Improvement of the blade shape

Chen, Liao and Cheng, (2012) develop a shrouded, small, horizontal-axis wind turbine for moving vehicles. Specifically, the effects of flanged diffusers on rotor performance of 30 cm wind turbines rotor diameter with different number of the blade (6 blades and 12 blades) and wind speeds (10–20 m/ s) is clearly investigated. A wind tunnel is used to experiment the rotor of the wind turbine with and without a flanged diffuser. The experimental results show that the flanged diffuser fairly well increases the torque output and rotor rotational speed of the wind turbine when compared with bare wind rotor, and largely depending on a number of blades and wind speed. For the 30%- and 40%-solidity rotors (6 blades), the flanged diffuser's effect plays a more important role in wind energy extraction than the blade's effect at wind speeds less than 20 m/s. For the 45%- and 60%-solidity rotors (12 blades), the blade's effect, in general, plays a more important role in wind energy extraction than the flanged diffuser's effect. This study also shows that the rotor solidity to achieve highest power coefficient of the investigated small wind turbine is around 35–40%, which is different from a conventional large wind turbine of less than 10%. Duquette and Visser, (2003) showed the solidity of 15–25% yielded higher power coefficient with rotor radius of 1 m. These results suggest that the smaller the rotor diameter, the larger the rotor solidity should be adopted for a higher power coefficient.

The effect of the gap flow modelling in ducted propeller performance predictions is studied in detail by Baltazar, Falcão de Campos and Bosschers, (2015) with a panel method, also known more recently as a boundary Element Method. The governing equation of steady potential flow on ducted propellers is solved by using a low order panel method. Many configuration models for the potential flow in the gap region are investigated: a tip leakage model with a vortex sheet shed along the blade, and tip non-zero and zero gap width. The analysis is carried out for two configurations: propeller Ka4-70 inside duct 19A and propeller 4902 inside duct 37. By studying the result, a strong influence of the gap model on the propeller and duct loads is clearly noted. The conclusion that the modelling of flow through the gap region is of the utmost importance for an accurate prediction of the forces on ducted propellers.

Kannan, Mutasher and Lau, (2013) aimed to optimize the diffuser design of Diffuser Augmented Wind Turbine (DAWT). Different diffuser design concepts were developed. The investigation of the effect of wind velocity on different shapes of flanged diffusers is done to develop the suitable

diffuser for the wind turbine. The characteristic of DAWT have been studied with the diffuser duct. Computational Fluid Dynamic (CFD) software ANSYS Fluent and software Solidworks are used for each design to carry out a comprehensive simulation. Results show that a 4 m/s inlet velocity a reasonable increase to reach 6.45 m/s final wind velocity in the redeveloped design with 61.25% over, which was achieved using 16° diffuser opening angle coupled with a 0.5 m diffuser splitter and a 4° splitter opening angle.

2.5.3. Calculation of system performance

Lawn, (2003) analysed the performance of a shrouded turbine using one-dimensional theory. At specified diffusion efficiencies, the analysis is carried out by varying the ducts upstream and downstream of the turbine as contractions or expansions. It is shown that there is an optimum turbine pressure drop for generating maximum power given diffuser efficiencies because the velocity ratio of the duct is proportional to the pressure drop of the turbine. The theoretical result Simple confirm by the experiment with static resistance elements in the duct and suggest that there is little to be gained by controlled diffusion at the inlet. However, applying more efficient controlled diffusion at the outlet can lead to power enhancements of more than 30 percent over an optimized turbine at the same diameter and the free stream velocity.

Matsushima, Takagi and Muroyama, (2006) aimed to introduce small wind turbine systems to radio relay stations as an independent power supply system. The improvement effects of a diffuser are studied on the output power of small wind turbine systems. According to economic standpoint and wind speed distribution, a frustum-shaped diffuser was chosen to improve the output power of the system. The 3-D simulation of the diffuser's shape surrounding the wind turbine was analysed by using the thermo-hydrodynamic analysis software program, I-DEAS, which showed that the wind speed in the diffuser has great sensibility by the length and expansion angle of the diffuser. Also, the simulation result concludes that maximum wind speed increased 1.7 times with the selection of the appropriate diffuser shape. Fig. 2.16 shown a field test using a real examination device with a diffuser. This is confirmed that the output power of the wind power generator increased by up to 2.4 times compared to that of a conventional turbine. Moreover, the gain of the diffuser has is emphasized especially where the wind direction was constant.

Moeller and Visser, (2010) carried out a numerical and experimental investigation of a Diffuser Augmented Wind Turbine (DAWT). Historically, higher material cost and less than stellar real-world performance lead to obstruct the advantages of DAWT concept. The new configuration is present, which combines a duct augmentation concept with an optimized, high solidity, twisted flat plate rotor, a relatively low tip speed ratio. It works a turbine towards a lower cost per kilowatt than other similar sized machines. An experimental test is carried out for WindTamer™ Initial Configurations to compare with a numerical blade element momentum analysis, which turbine efficiencies of 0.23–0.25 were resulted. To obtain efficiency approaching 0.4, an optimized flat plate blade geometry design is developed. When the optimized flat plate blade with the diffuser is combined, the experimental test exhibits system efficiencies greater than 0.60. The possibility of higher annual energy outputs is achieved. An additional benefit as, the turbine appears ability to self-regulate at higher wind speeds, eliminating the need for a furling mechanism.

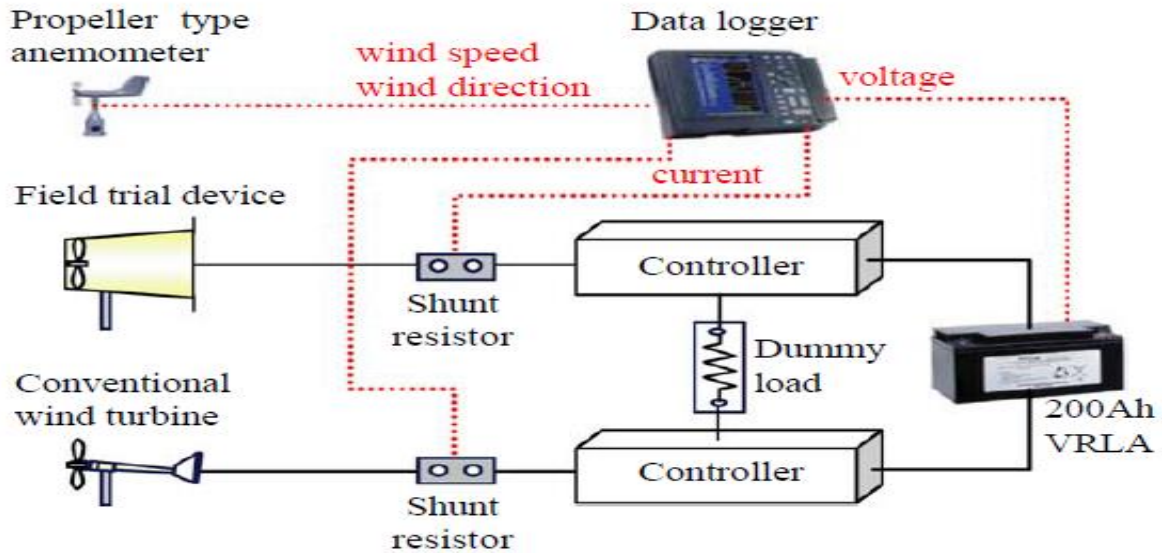


Fig. 2.16. Experimental apparatus(Moeller and Visser, 2010)

Michal, Maciej and Krzysztof, (2016) discussed simulation results of various wind turbine rotor models implemented in computational fluid dynamics (CFD), with particular emphasis on the interaction of a rotor with the surrounding airflow. A configuration of the model consists of a wind turbine rotor placed at the inlet of a divergent duct; a pattern known as Diffuser-Augmented Wind Turbine (DAWT). The Institute of Turbo machinery of Lodz University of Technology has recently an object of numerous studies related to this type of wind energy converter. They focused on their search of evaluation performance of wind turbine with method that combined high accuracy and tolerable time-to-results factor. The three different models of the DAWT is undertaken as FRM (Fully-resolved Rotor Model), ADM (Actuator Disk Model) and authors' modified approach to ALM (Actuator Line Model). All mentioned model methods are implemented by a commercial solver ANSYS CFX 15.0. The previous experimental data is used to find characteristics the wide spectrum of actuator models, and is compared it with 3D CFD rotor modelling. The comparison of the calculated results with available experimental data is done, to validate the result of CFD models, and to accurately estimate of turbine performance. The authors' proposal is the presentation of modified approach to ALM, which achieved the study goals from the viewpoint of the numerical effort by reduction computation time and resources necessary.

Shives and Crawford, (2011) presented a combination of blade element and computational fluid dynamics (CFD) method for performance analysis and optimization of ducted turbines. The presented model seems a model of standard blade element momentum theory, but the difference that the CFD replace the momentum equation to determine the induction factors. This method eliminates many assumptions used in applying the typical blade element momentum theory to a turbine and provides more detail information about the flow. The importance of the model clearly appears for modelling ducted turbines because there is no fundamental momentum theory model that includes the impact of the duct on the flow field. An axisymmetric domain is stimulated to increase computational efficiency. A simple algorithm was developed to determine the optimum rotor loading and tip speed ratio for a given duct geometry within a user-defined level of granularity. The conclusion that for certain ducts, a non-uniform loading over the disk can improve overall performance by limiting flow separation within the duct. Hansen, Sørensen and Flay, (2000) develop an actuator disc CFD model of the flow through a wind turbine surrounding by a

diffuser duct. Additionally, a simple 1D analysis is performed, which theoretically shown the Betz limit can be exceeded by a factor proportional. Because of the relative increase in mass flow through the rotor induced by the diffuser duct. The theoretical 1D result is verified by the CFD model

Vortex Energy, is company specialize in wind energy field, undertaken Research for developing an efficient Diffuser Augmented Wind Turbine (DAWT). Schaffarczyk and Phillips, (2001) carried out an extensive program of both computational and experimental work to characterize the DAWT performance. Computational models using the Navier-Stokes solvers CFX and FLUENT with the turbine modelled as an actuator disc are successfully predicted the performance of the DAWT. As main part of this program, the integration of a matched rotor within the diffuser has been investigated. A hotwire anemometry and flow visualization are used within Wind tunnel investigations of the Multi-Slotted Diffuser to establish the diffuser performance over a range of constant disc loading coefficients. A truncated conventional wind turbine blade, a genuine turbo-machinery type blade and an empirically designed DAWT blade are studied to evaluate the more suitable design theory integration with a diffuser duct. To validate the computational model result, the performances of the three types of blades is compared the wind tunnel result. The conclusion that the ordinary blade-element/momentum theory, with replaced the usual thrust induction factor relationship by one empirically derived from DAWT wind tunnel tests, provides the best results to date.

Aranake, Lakshminarayan and Duraisamy,(2013) carried out Computational analysis of diffuser-augmented turbines. the Shroud duct geometries, generated by the extrusion of airfoil profiles into the annular circumference of the tip wind turbine blade, and the main aim of this geometries is increasing on their ability to capture mass-flow through the interior of the shroud. Of the shapes considered, the Selig S1223 high-lift low- Re airfoil is found to best promote mass flow rate. The high-resolution grid is used for computations of the Reynolds Averaged Navier–Stokes equations supplemented with a transition model, as shown in Fig. 2.17. After that, the calculations of axisymmetric high-lift airfoil sections are carried out. The mass flows through a shroud increase nearly linearly with radial lift force, and nonlinear effects are examined in terms of the location of the leading-edge stagnation point.

Jafari and Kosasih, (2014) demonstrated significant power augmentation of diffuser shrouded horizontal axis wind turbine by comparing to bare one with the same swept area of the diffuser. A model of AMPAIR 300 wind turbine (Commercial type) is studied by using experimental and computational fluid dynamic (CFD) techniques. These studies found the degree of the augmentation is strongly dependent on the shape and geometry of the diffuser such as the length and the expansion angle. To prove that, the CFD simulations of a small commercial wind turbine have been carried out with a simple frustum diffuser shrouding. The various configuration of the diffuser is simulated with the aim to understand the effect of length and area ratio on power augmentation. Fig. 2.18 show a sub-atmospheric back pressure is found to be the most effective factor in power augmentation. The diffuser area ratio significantly affects the pressure drop in the diffuser. A flow separation in the diffuser can lead to reducing the pressure recovery coefficient which reduces the overall power coefficient. The length of the diffuser can be adjusted to eliminate the separation. The main aim of this study is present the methods for determining effective frustum diffuser geometries for a small wind turbine. These presented results are able to extend for any types of wind turbines designed for nominal wind speed.

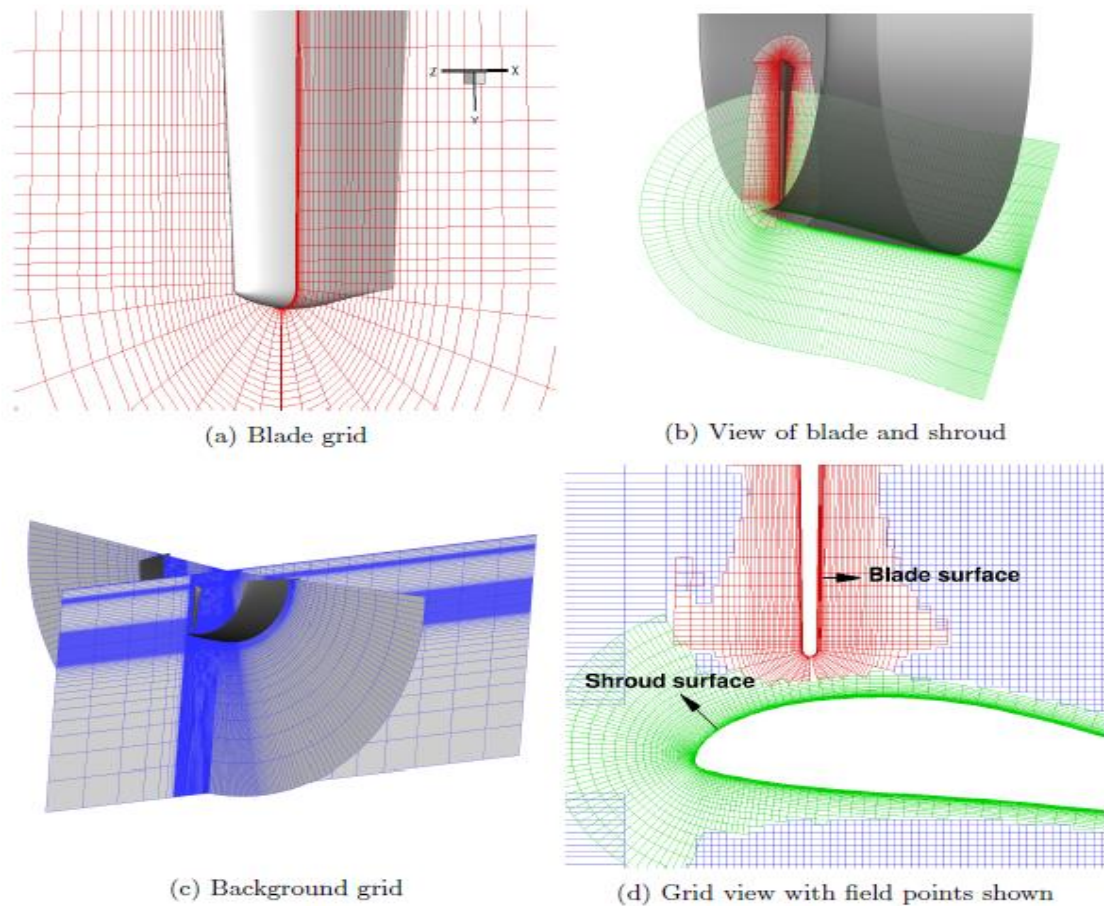


Fig. 2.17. Overset grids used for 3D computations(Aranake, Lakshminarayan and Duraisamy, 2013)

However, full three-dimensional simulations of shrouded wind turbines are performed for selected shroud geometries. To show the shroud duct effect, the results of the shrouded turbine are compared to bare turbine solutions. The ratio of the power generated by a shrouded turbine to the Betz limit (Augmentation ratios) reach up to 1.9 by the shrouded turbines. The Peak augmentation power occurs at the highest wind speed for which the flow over the bare turbine blade stays attached. Flow fields are studied in detail and the following aspects are investigated: regions with flow separation, the development of averaged velocity profiles, and the interaction between the helical turbine wake and shroud boundary layer. Finally, power augmentation is demonstrated to continue the increase in high wind velocities, at which the turbine blade would otherwise stall, if a tip speed ratio is of constant value.

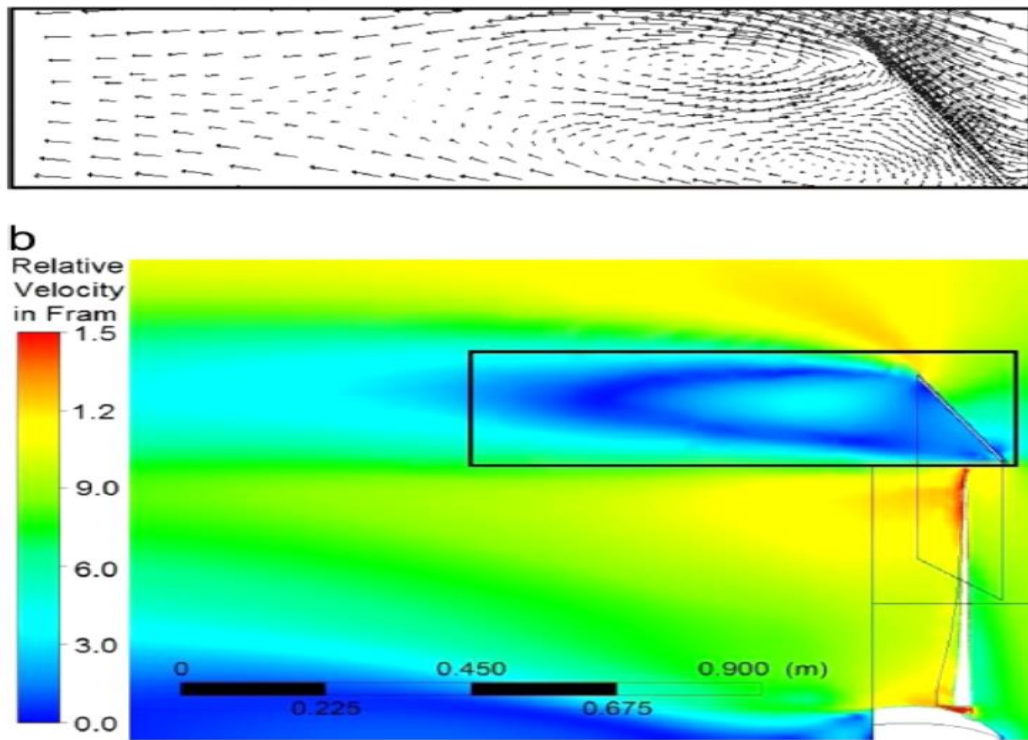


Fig. 2.18. (a) Velocity vectors and (b) velocity magnitude contour in separation region of AMPAIR 300 wind turbine with frustum diffuser(Jafari and Kosasih, 2014)

2.6. Timeline of the previous researches

The solar chimney power plant is a newfangled technology that utilizes solar energy to generate more clean energy. The principle of the SSCP operation is quite simple, combining wind turbine and the greenhouse effect with the chimney suction to achieve these purposes. Table 2.1 shows timeline and summarizes the literature of solar chimney.

Table 2.1. Summarize the literature of solar chimney

Authors	Year	Highlight
M. Simon	1976	the idea of the solar chimney for electricity generation was economically Studied
Haaf et al.	1979	the first prototype was developed with a designed peak output of 50 kW in Manzanares, Spain. This pilot plant ran from the year 1982 to 1989
Schwarz and Knauss	1981	The single vertical axis turbine layout without inlet guide vanes was designed for the pilot SSCP plant in Manzanares, Spanish
Yan et al.	1991	Overall efficiency is directly related to the height of the chimney and is shown to be about 1% for a height of 1000 m.
Pasumarthi and Sherif	1998	The experimental and mathematical were used model to study the effect of various parameters on the air temperature, air velocity, and power output of the solar chimney and two experimental configurations were tried on the collector.

2. Literature review

Gannon and Von Backström	2002	The single rotor with inlet guide vanes layout was presented, they used the method which was adapted from gas turbine literature.
Denantes and Bilgen	2006	two counter-rotating stage turbines with/without inlet guide vanes was presented and compared its performance to a single stage system.
Tingzhen et al.	2008	The findings result indicated that a better option for the operating condition is a slightly increase in the rotational speed on speed corresponding to maximum turbine efficiency to achieve maximum power output.
Tingzhen et al.	2008	A numerical simulation of the solar chimney power plant systems coupled with turbine was carried out by FLUENT
Fluri and von Backström	2008	the performance of various layouts for the proposed turbo generator was compared with the previous researchers using analytical models and shown optimization techniques, and discussed the important design parameters.
Zhou, Wang and Ochieng	2010	They proposed various layouts were proposed for turbines of the solar chimney, which show the turbine configurations include the single vertical axis, the multiple vertical axis, and the multiple horizontal axis turbine layouts with or without inlet guide fan.
Kasaeian, Heidari and Vatan	2011	a solar chimney pilot power plant was developed with 10 m collector diameter and 12 m chimney height, after designing and installing, measured the temperatures and air velocities inside the SCPP.
Li et al.	2012	the performance of SCPP was evaluated by developing the comprehensive theoretical model, this model is validated by comparing with the experimental data of the Manzanares, Spanish prototype
Hamdan and Rabbata	2012	a prototype of solar chimney draft tower was installed in Al Ain in United Arab Emirates, which is 8 m high of chimney with 100 m ² collector area and 0.75 m of high.
Li, Guo and Wang	2012	a comprehensive theoretical model for the performance evaluation of a SCPP was developed, and the validation of the presented model was done by comparing with the experimental data of the Spanish prototype.
Koonsrisuk and Chitsomboon	2013	The theoretical model was solved by the iteration techniques to calculate produced power and pressure difference around the turbine
Patel, Prasad and Ahmed	2014	The optimization a geometry of the major components of the SCPP was studied using a computational fluid dynamics (CFD) technique software ANSYS-CFX to investigate and improve the flow characteristics inside the SCPP.

2. Literature review

Li et al.	2015	a turbine performance with rotational speed was investigated for the power-regulating strategy option for solar chimney turbines
Y Zhou et al.	2016	The designed turbine is presented for applied to solar chimney power plant with a vertical collector, based on the design theory of the wind turbine (BET).
Zhou and Xu	2016	The pervious Literature was Summarized about a pressure drop around the turbine that show pressure drop of the turbine in range 16/27(Betz Limit) to 0.9 to obtain the maximum performance of SCPP.
De_Richter et al.	2017	The hybrid SCPP was presented various methods of the combination of Solar chimney and removal of greenhouse gases.
Ming et al.	2017	To increase the amount of heat adding to air, they added radial partition walls to collector and compared the SCPP performance with conventional horizontal canopy and sloped canopy design
Cao et al.	2018	a mathematical model of transient performances was presented to calculate the accumulated power generation for one year, this model was used to study two types of a solar chimney collector
Ismail et al.	2019	New approaches have been numerically examined for improving both flow field and heat transfer characteristics of a collector of an SCPP using passive flow control,
Alktranee and Yaseen	2019	Their conclusion that a contemporary construction of SCPP has no limitation for chimney height for producing the maximum attainable power of the SCPP technology, whereas, it has a limitation on the maximum collector radius in the same term
Toghraie et al.	2018	The optimization of the chimney radius was presented for achieving the maximum values for efficiency and output power.

Table 2.2 shown timeline and summarize the literature of the diffuser-augmented wind turbine aerodynamic.

Table 2.2 summarize the literature of shrouded wind turbine

Authors	Year	Highlight
Gilbert and Foreman	1983	the experimental prototype of the diffuser-augmented wind turbine (DAWT) without screen meshes was developed. The screen meshes employed various to simulate the energy extraction mechanisms of a wind turbine.
Igra	1985	The wind turbine should be surrounded inside a specially designed shroud to take advantage of wind power as economically as possible. Various geometries of the shroud were studied that resulted from a significant power augmentation with using a fairly compact shroud

2. Literature review

- Sørensen and Flay 2000 An actuator disc CFD model of the flow through a wind turbine surrounding was developed by a diffuser duct. Additionally, a simple 1D analysis is performed, which theoretically shown the Betz limit can be exceeded by a factor proportional.
- Schaffarczyk and Phillips 2001 An extensive program of both computational and experimental work was carried out to characterize the DAWT performance. Computational models using the Navier-Stokes solvers CFX and FLUENT with the turbine modelled as an actuator disc are successfully predicted the performance of the DAWT
- Lawn 2003 The performance of a shrouded turbine using one-dimensional theory was analysed. At specified diffusion efficiencies, the analysis is carried out by varying the ducts upstream and downstream of the turbine as contractions or expansions. It is shown that there is an optimum turbine pressure drop for generating maximum power given diffuser efficiencies because the velocity ratio of the duct is proportional to the pressure drop of the turbine.
- Matsushima, Takagi and Muroyama 2006 A small wind turbine system was introduced to radio relay stations as an independent power supply system. The improvement effects of a diffuser are studied on the output power of small wind turbine systems.
- Ohya *et al.* 2008 A new wind turbine system was developed, which consists of a wind turbine rotor surrounded by a diffuser shroud with a broad-ring flange at the exit periphery
- Moeller and Visser 2010 A numerical and experimental investigation of a DAWT was carried out. Historically, higher material cost and less than stellar real-world performance lead to obstruct the advantages of DAWT concept
- Shives and Crawford 2011 A combination of blade element and computational fluid dynamics (CFD) method was presented for performance analysis and optimization of ducted turbines. The presented model seems a model of standard blade element momentum theory, but the difference that the CFD replace the momentum equation to determine the induction factors
- Chen, Liao and Cheng, 2012 A shrouded, small, horizontal-axis wind turbine was developed for moving vehicles. Specifically, the effects of flanged diffusers on rotor performance of 30 cm wind turbines rotor diameter
- Aranake, Lakshminarayan and Duraisamy 2013 The Shroud duct geometries, generated by the extrusion of airfoil profiles into the annular circumference of the tip wind turbine blade, and the main aim of this geometries is increasing on their ability to capture mass-flow through the interior of the shroud.
- Kannan, Mutasher and Lau 2013 The diffuser design of Diffuser Augmented Wind Turbine was optimized. Different diffuser design concepts were developed.

		The investigation of the effect of wind velocity on different shapes of flanged diffusers is done to develop the suitable diffuser for the wind turbine.
Hjort and Larsen	2014	A new approach of diffuser augmented wind turbines was presented. The new concept of the diffuser takes advantage of an aerodynamic principle for the creation of high-lift airfoil configurations that famous in the aircraft industry.
Jafari and Kosasih	2014	significant power augmentation of diffuser shrouded horizontal axis wind turbine was compared to bare one with the same swept area of the diffuser. A model of AMPAIR 300 wind turbine (Commercial type) is studied by using experimental and computational fluid dynamic (CFD) techniques.
Baltazar, Falcão de Campos and Bosschers	2015	The effect of the gap flow modelling in ducted propeller performance predictions is studied with a panel method, also known more recently as a boundary Element Method
Michal, Maciej and Krzysztof	2016	Various wind turbine rotor models were implemented in computational fluid dynamics (CFD), with particular emphasis on the interaction of a rotor with the surrounding airflow. A configuration of the model consists of a wind turbine rotor placed at the inlet of a divergent duct; a pattern known as Diffuser-Augmented Wind Turbine (DAWT).

2.7.Characteristics of the solar chimney turbine

A turbine of the SCPP has characteristics between a gas turbine and wind turbine. This leads the researchers to use different theories for a design of the turbine. Gannon and Von Backström, (2002a , 2003, 2004b), Denantes and Bilgen, (2006) , and Fluri and von Backström, (2008) used the free vortex design. The free vortex approach is used in an axial flow gas turbine stage annulus and is assumed to be fully cascaded airfoil (two dimensions) when the flow parameters are functions of two space coordinates, in other words, the radial effect on the flow is ignored. The radial equilibrium assumption is reasonable in the case of typical short blades as front stages of gas turbines, whose a hub to tip ratio of the blade is greater than 0.8 which is the maximum limiting for achieving harmony with this assumption (Akeel and Najjar, 2013). Therefore, the weak point is revealed in using free vortex design, because of this hub to tip ratio is difficult to achieve in case of the SCPP.

On the other hand, Zhou *et al.*, (2016) used Wilson theory to design the SCPP turbine. The Wilson design is a classical theory to design horizontal axis wind turbines. The control volume is applied to a rotor (propeller) of the wind turbine. This theory assumes that the affected mass of air remains separate from the air which does not pass through the rotor of the turbine. In other words, the undergone rotor hasn't any surrounding wall border. So, the assumption is that the flow is completely free. In the case of the solar chimney, the flow is constricted inside the inner diameter of the chimney. It is clear now, that the assumptions of the Wilson design cannot be considered in the case of a solar chimney.

Recently, the development of wind turbines has been the focus of many researchers. A shrouded wind turbine is one of the improvements, which helps to increase the power coefficient of the wind turbine by surrounding a rotor of the wind turbine with a diffuser duct. The researchers aimed to modify the classic aerodynamic theories. Consequently, the design theory considers the effect of the surrounding diffuser duct that makes the shape of the blade more suitable for the surrounding duct and produces more output power in the same diameter. The newly developed approach is nearly close to a case of the solar chimney.

2.8. Summary of literature review evaluation

A comprehensive literature review of a solar chimney power plant (SCPP) reveals solar chimney approaches, and designs have been carried out. Various layouts have been proposed for the SCPP system, but no method is available to make an informed decision on which layout to choose. Consequentially, an integrated design of the various components and optimization of overall system performance is necessary. The optimization of the SCPP needs more effort to get the maximum output power, researchers used many techniques: experiment, mathematical models, and simulation. I have also reviewed the theory of aerodynamic of the shrouded wind turbine.

The main objective of this work is to approach a new design of axial flow turbine for working in solar chimney power plants (SCPP). The design of an axial flow turbine is presented based on the Blade Element Theory (BET), which I develop to improve the performance of the turbine of SCPP by the concept of Argument diffuse wind turbine (ADWT). My mathematical model considers the surrounding duct of the turbine and predicts the expected output power, according to the characteristics of the solar chimney turbine. An aerodynamic analysis accounting for the surrounding diffuser duct is presented, which determines the parameters of the design. My mathematical model depends on easily measurable quantities to estimate the performance of SCPP. Also, it calculates the temperature distribution of the collector and flow field inside the SCPP with fewer assumptions in the theoretical analysis.

The performance of SCPP system is accurately analysed by using the CFD simulation model, with fewer assumptions used in the theoretical calculation, but more detailed descriptions of pressure and flow field can be obtained. A 3D approach for SCPP prototype is carried out by using ANSYS CFX v18 with axial vertical flow turbine. To select the suitable theory of turbine design, I have to compare different theories with SCPP system. The 3D numerical simulation incorporating the radiation models and turbine models. Results from the mathematical model are compared with prototypes of Manzanares, Spain and Aswan, Egypt experimental results for model validation. I study the performance of SCPP with two different shapes of collector.

Experimental works provide an accurate and realistic performance of the physical system; however, we manufactured the solar chimney turbine with the 3D printing technology. The blade calculation is according to my comprehensive mathematical model. Tests of the turbine are carried out on a wind tunnel of 1m diameter and 8 m length. We measured the electrical output power, pressure difference around the turbine and airflow rate to calculate dimensionless parameters.

3.MATERIALS AND METHODS

Using sustainable energy has many scientific and technical challenges due to non- concentrated resources, which reduces the efficiency of devices that used to harvest renewable energy. Solar chimney power plant (SCPP) is a new technology that depends on renewable energy sources. To raise its reliability and expansibility, efficient design of the solar chimney system components is an utmost necessity. A turbine is a key component because it captures the mechanical energy from airflow. The conditions of operation of the turbine inside SCPP impose particular characteristics of the turbine, these characteristics for the turbine are between a gas turbine and wind turbine. The efficient design of the turbine achieves the maximum output power from the SCPP unit.

In this chapter, the materials and methods of the new solar chimney turbine design are proposed, my comprehensive mathematical model is also presented to determine the new design parameters, that calculate the flow field conditions on the critical point on SCPP system. The performance of SCPP is investigated by CFD model and experiments.

3.1. Aerodynamic analysis of a shrouded turbine

Wind turbine extracts kinetic energy from the wind. Kinetic energy in the wind is absorbed by wind turbine by slowing down the wind, as shown in Fig. 3.1. If it is assumed that mass of the air passing through the turbine is separated from the mass that is not passing through the turbine, then the separated part of the flow field remains a long stream tube, which lies upstream and downstream of the turbine. While the air passes through the wind turbine, the velocity of the air changes. The turbine absorbs the kinetic energy of air and the velocity of the air decreases following the turbine. Since mass flow rate is the same, to compensate this loss in the velocity, the stream tube extends after the turbine.

The aerodynamic analysis of the wind turbine consists of the actuator disc theory that applies the momentum concept on the infinite number of the blade rotor, the rotor disc theory that takes into account the rotation effect of the rotor, and the blade element theory (BET) that considered the force acting on an element of the blade. The analysis is incorporated with the diffuser duct effect to make the blade more sensitive and to have efficient performance during its working inside the duct. By solving equations of the BET theory, the chord distribution and twist angle are obtained presenting the final shape of the blade turbine.

Many authors derive a number of steady state wind turbine performance calculation methods. Betz and Glauert develop the classical analysis method in 1930 (Song, 2012). In this method, Blade Element and Momentum theories are combined into a strip theory. The theory enables the calculation of the performance characteristics of an annular section of the rotor.

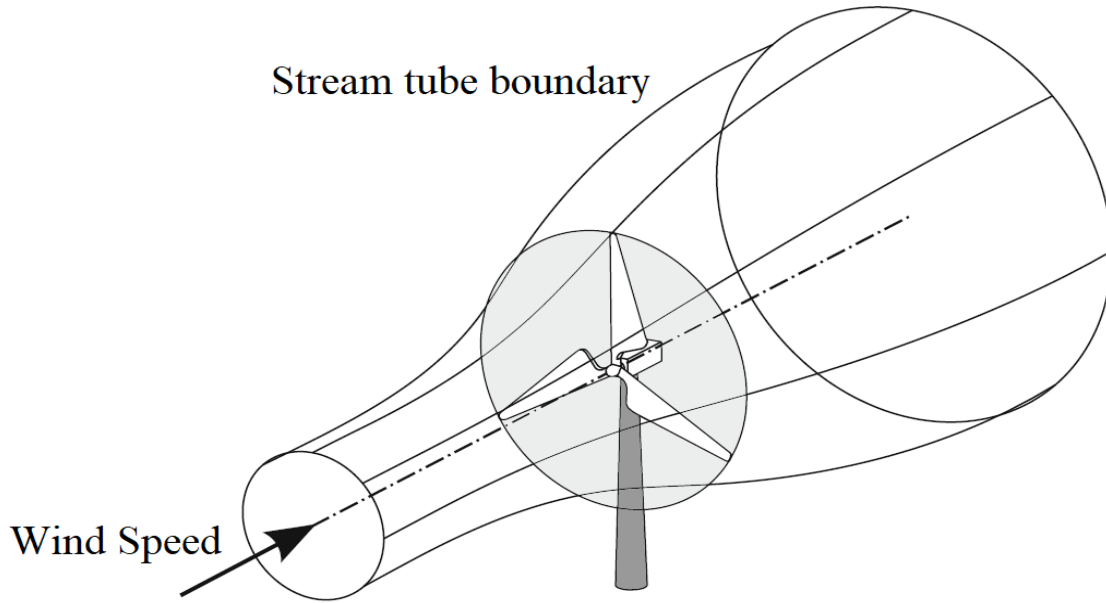


Fig. 3.1. Stream tube generated through wind turbine

3.1.1. Actuator disc theory considering surrounding duct

Before studying the blade geometry by using the blade element theory, the momentum theory of actuator disc and wake rotation effect should be taken into account to define essential terms. Fig. 3.2 shows the control volume, which is incorporated in the diffuser duct with the actuator disc theory. The momentum theory ignores the frictionless air flow through the control volume and assumes that the air flow is parallel to the axis without rotation in the wake. Consequently, the velocity that acts on the disc is expressed (G.J.W. Bussel, 1999) as:

$$V_1 = V_2 = (1 - a)V_{max} = \gamma(1 - a)V_0, \quad (3.1)$$

where, a is axial induction factor, γ is the ratio of the maximum axial velocity of flow in the diffuser by the free stream velocity $\gamma = V_{max} / V_0$ which is called the diffuser velocity speed-up ratio. V_1 , V_2 and V_0 are the air velocity at plane 1, 2 and 0 on Fig. 3.2 respectively.

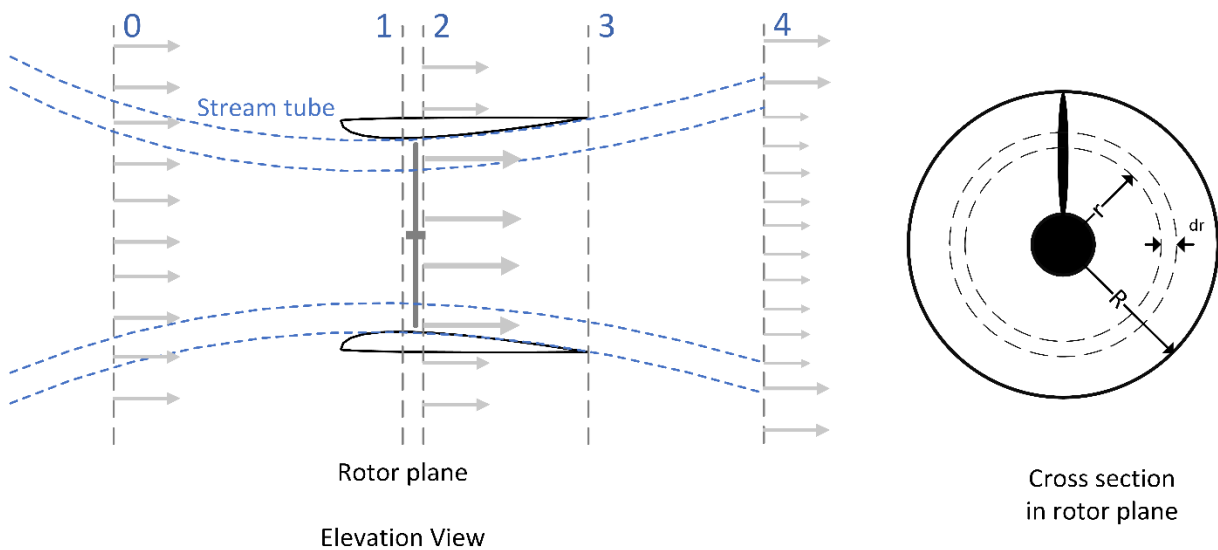


Fig. 3.2. The control volume of actuator disc theory with diffuser

By modifying the classical theory with diffuser, the power coefficient is defined as (Vaz and Wood, 2016) and (Phillips, 2003) :

$$C_P = \varepsilon \left[1 - \left(\frac{V_4}{V_0} \right)^2 - (1 - \eta_d)(1 - \beta^2)\varepsilon^2 \right], \quad (3.2)$$

where ε is the velocity speed-up ratio, $\varepsilon = \frac{V_1}{V_0} = \gamma(1 - a)$, β is the exit area ratio in Fig. 3.2, $\beta = A_1 / A_3$, A_1 and A_0 are the area at plane 1 and 0 on Fig. 3.2 respectively, and η_d is the diffuser efficiency, $\eta_d = \frac{p_3 - p_2}{\frac{1}{2}\rho(V_2^2 - V_3^2)}$.

The energy balance is applied at the downstream of the diffuser exit to obtain connection between the velocity V_4 and free- stream velocity:

$$\left(\frac{V_4}{V_0} \right)^2 = \varepsilon^2 \beta^2 + c_{p3}, \quad (3.3)$$

where c_{p3} is the pressure coefficient, which is define by (Tavares Dias Do Rio Vaz et al., 2014) as:

$$C_{p3} = \frac{p_3 - p_0}{\frac{1}{2}\rho V_0^2}. \quad (3.4)$$

Using definition of the velocity in Eq. 3.1, the pressure coefficient becomes:

$$C_{p3} = (1 - \gamma^2 \beta^2)(1 - a^2) + a(3a - 2). \quad (3.5)$$

Applying the energy balance equation on the disk shown in Fig. 3.2, the thrust coefficient is obtained by

$$C_T = \frac{T_d}{\frac{1}{2}\rho A V_0^2} = \frac{\frac{1}{2}\rho A (V_0^2 - V_4^2)}{\frac{1}{2}\rho A V_0^2} = 4a(1 - a). \quad (3.6)$$

Substituting Eqs. 3.5 and 3.3 into Eq. 3.2 to obtain the power coefficient:

$$C_P = \gamma(1 - a^2)[4a + \gamma^2(1 - a)(\eta_d - 1)(1 - \beta^2)]. \quad (3.7)$$

By neglecting the loss in the diffuser $\eta_d = 1$, then Eq. 3.7 become

$$C_P = 4a \gamma(1 - a)^2. \quad (3.8)$$

Comparing C_P with the bare wind turbine, $C_{P,Bare}$, proves that the power coefficient of the DAWT is greater than the power coefficient of the bare one by γ times, $C_P = \gamma C_{P,Bare}$ (γ is usually greater than 1). In classic actuator disc theory for bare wind turbine, maximum value of C_P is achieved while axial induction factor, a , is $1/3$ according to Betz limit. The power coefficient C_P of the DAWT is more than the maximum of Betz limit. $C_{P,Max} = \gamma \frac{16}{27}$. In other words, we can say, the diffuser duct increases the produced power with the same diameter in the same operational conditions, and this effect is controlled by the diffuser velocity speed-up ratio, γ .

3.1.2. Rotor disc theory considering surrounding duct

The actuator disk theory does not consider the wake rotation, but the rotation of the wake is an essential effect to produce the power. It defines the tangential induction factor, a' , that has an enormous influence on the shape of the blade turbine and subsequently its performance. By undergoing an infinitesimal control volume of an area $dA = 2\pi r dr$, to apply the angular momentum equation the elementary available torque dM can be obtained as:

$$dM = \rho V_1 w r^2 dA = 2\rho a' \gamma (1 - a) V_0 \Omega r^2 dA \quad (3.9)$$

where r is the radial position on the blade from hub to tip, w is the angular velocity of air in the near- wake, $w = 2\Omega a'$, and Ω is the rotor angular velocity (Burton *et al.*, 2011).

The torque coefficient is defined as:

$$C_M = \frac{dM}{\frac{1}{2} \rho V_0^2 dA} = \frac{4a' \gamma (1 - a) \Omega r^2}{V_0} \quad (3.10)$$

The elementary produced power is calculated by:

$$dP = \Omega dM = 2\rho a' \gamma (1 - a) V_0 \Omega^2 r^2 dA \quad (3.11)$$

By integrating this expression across the rotor from $r = 0$ to $r = R$, the power coefficient is obtained by:

$$C_P = \frac{P}{\frac{1}{2} \rho A V_0^3} = \frac{8}{\lambda^2} \int_0^\lambda \gamma a' (1 - a) x^3 dx, \quad (3.12)$$

where λ is the tip-speed ratio, $\lambda = \Omega R / V_0$, and x is the local-speed ratio, $x = \Omega r / V_0$.

3.1.3. Blade element theory considering surrounding duct

After studying the effect of the diffuser on the turbine performance using the actuator disc theory and rotation effect, forces acting on the blade are obtained by applying the blade element theory (BET). The BET suggests that the blade is to be divided into N sections, there is no aerodynamic interaction between blade sections. The blade sections are called blade elements. The forces acting on the blade elements are determined solely by the drag and lift coefficient of 2D aerofoils of the blades. Consequently, the aerodynamic forces which have an effect on the turbine blades are also expressed as a function of lift and drag characteristics of the aerofoil and the aerofoil's characteristics depend on the angle of attack and Reynolds number. Fig. 3.3 shows the velocity diagram and forces acting on the section of the rotor blade element.

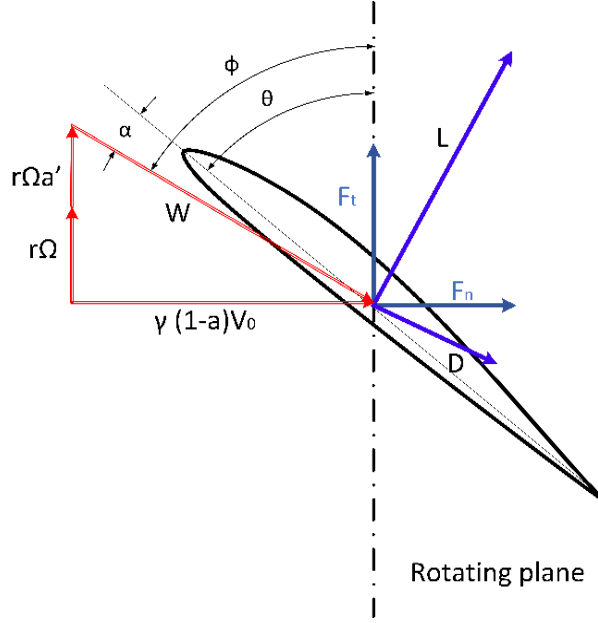


Fig. 3.3. Blade Element forces and velocity diagram

The flow angle can be obtained by the velocity diagram shown in Fig. 3.3:

$$\tan \phi = \gamma \frac{(1-a)V_0}{(1+a')\Omega r} = \gamma \frac{(1-a)}{(1+a')x}. \quad (3.13)$$

From Fig. 3.3, the elemental normal and tangential force coefficients at any section of a blade are defined as:

$$C_n = \frac{F_n}{\frac{1}{2}\rho W^2 c} = C_l \cos \phi + C_d \sin \phi \quad (3.14)$$

and

$$C_t = \frac{F_t}{\frac{1}{2}\rho W^2 c} = C_l \sin \phi - C_d \cos \phi \quad (3.15)$$

respectively. Where C_l and C_d are the lift and drag coefficients of the airfoil respectively.

The thrust and torque coefficient can be expressed for the number of the blades, B , as:

$$C_T = \gamma^2 (1-a)^2 \frac{\sigma_s C_n}{\sin^2 \phi} \quad (3.16)$$

and

$$C_M = \gamma(1-a)(1+a')x \frac{\sigma_s C_t}{\sin \phi \cos \phi} \quad (3.17)$$

respectively.

where σ_s is the local solidity, $\sigma_s = Bc/2\pi r$, and c is the local blade chord.

By combining Eqs. 3.16 with 3.6, the axial induction factor can be obtained:

$$\frac{a}{1-a} = \gamma^2 \frac{BcC_n}{8\pi r \sin^2 \phi}. \quad (3.18)$$

By combining Eqs. 3.17 with 3.10, the tangential induction factor can be obtained:

$$\frac{a'}{1+a'} = \frac{BcC_t}{8\pi r \sin \phi \cos \phi}. \quad (3.19)$$

The actuator disc theory assumes an infinite number of blades for a turbine rotor, however, Prandtl introduced the concept of a tip loss to account for the difference between a real turbine or propeller that having a finite number of blades and theoretical one (Clifton-Smith, 2009). To determine the optimum blade shape for maximum produced power, the refinement of BET by tip loss corrections is important. The tip loss factor, F , is defined as the ratio of the azimuthally averaged axial induction factor, a , to the axial induction factor local to the blade, a_r .

The induced velocities and the mass flux influence by the tip loss correction, sequentially, Eqs. 3.18 and 3.19 is corrected according to Shen *et al.*, (2005):

$$\frac{a_r F (1 - a_r F)}{(1 - a_r)^2} = \gamma^2 \frac{BcC_n}{8\pi r \sin^2 \phi}, \quad (3.20)$$

$$\frac{a' F (1 - a_r F)}{(1 + a'_r)(1 - a_r)} = \frac{BcC_t}{8\pi r \sin \phi \cos \phi}. \quad (3.21)$$

Vaz and Wood, (2016) expressed the tip loss factor that take into consideration the diffuser duct by term the diffuser velocity speed-up ratio, γ , as :

$$F = \frac{2}{\pi} \cos^{-1} e^{-f}, \quad (3.22)$$

where $f = \frac{B}{2r\gamma(1-a_r)V_0} \frac{W(R-r)}{}$

the above discussion clearly shows the effect of the diffuser duct on the blade element theory by the diffuser velocity speed-up ratio term. The main challenge is a way to obtain this value, γ . Vaz and Wood, (2016) used the average of the experimental data, which was carried out by ten Hoopen, (2009) to obtain the value of the diffuser velocity speed-up ratio. On the other hand, Barbosa *et al.*, (2015) described the internal velocity for different configuration of the conical diffusers by developing a mathematical model based on the Biot–Savart law to take into account the characteristics of flow around them. In this study, the mathematical model of the solar chimney (SC) is developed to calculate the diffuser velocity speed-up ratio, γ , and the free stream velocity, V_0 . This makes the blade shape of the turbine more suitable for working in solar chimney system.

3.2. Mathematical model of Solar Chimney

Solar chimney power plants (SCPPs) convert solar energy first into thermal energy then into kinetic energy and finally into electrical power. According to the operational principle mentioned in the introduction section, a mathematical model is presented here to study physical phenomena for main SCPP plant components (collector, chimney and turbine). The aim of this model is to calculate the essentials terms of the turbine design. The analysis used in this analysis is based on the following simplifying assumptions:

- The flowing humid air is considered as an ideal gas, the pressure specific heat capacity per unit mass, c_p , is as consequence function of temperature only;
- The heat losses through the wall of the chimney are neglected
- The flow in the collector is considered as a flow between two parallel plates;
- The frictional effect is ignored since the velocity in this region is quite low;
- The gas radiation is not taken into consideration due to low range of temperatures inside the collector;
- The uniform solar radiation acting on the collector surface (the sun's altitude angle is neglected)

The mathematical model studies the performance of the SCPPs by obtaining the properties of the flowing air at the critical points, which are indicated in Fig. 3.4. Point ① has known value, it is the ambient condition. I presented a new approach of heat transfer patten inside the collector to develop the mathematical model that can elevate the performance of SCPP with more accuracy. In the next sections, the properties of air in other points will be determined.

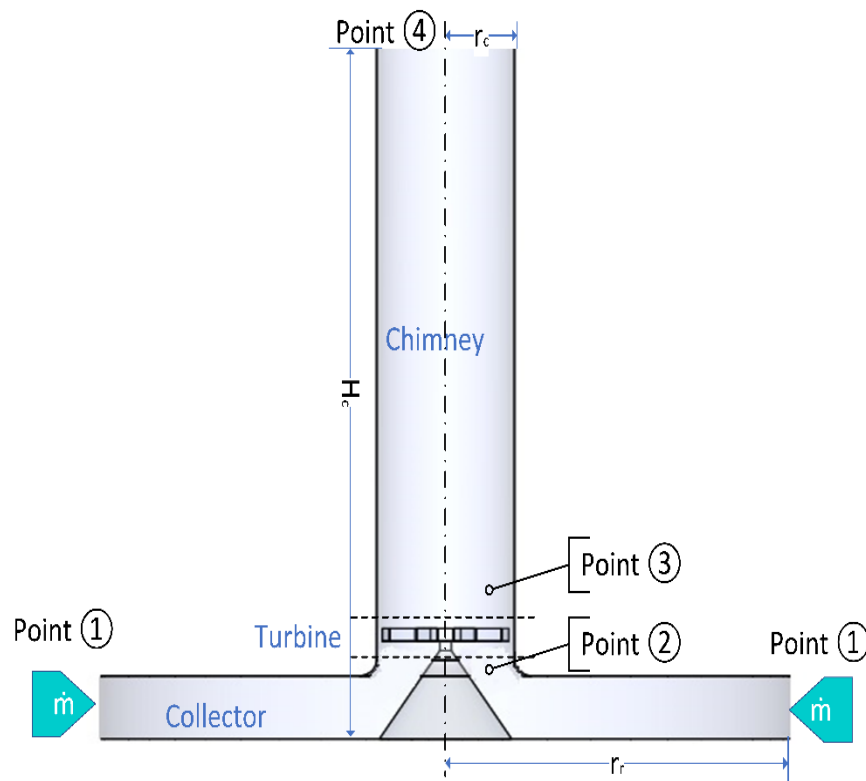


Fig. 3.4. Schematic mathematical layout of solar chimney power plant

3.2.1. Collector

As mentioned, one of the major components of a solar chimney power plant unit is the solar collectors, so I focused my study on the investigation of its performance then its influence on performance overall of the SCPP. Solar collectors are special kind of heat transfer tools, which utilize solar radiation to increase internal energy of the transport medium (ambient air). Direct and diffuse solar radiation fall on the transparent roof, where specific fractions of the energy are transmitted, absorbed and reflected. These fractions are a function of the solar incidence angle and optical characteristics of the glass, such as the thickness, refractive index and extinction coefficient and radiation wavelength. The solar radiation has a wavelength range from 0.3 to 3 μm , which is significantly shorter than the emitted radiation from most heat-absorbing surfaces (Duffie and

Beckman, 2013). However, the structure of a collector changes according to consideration of architectural and civil design (Dahri and Omri, 2013).

I have been studied thermal analysis for the solar collector in considerable detail to understand the performance of the SCPP and I have been developed the thermal network to demonstrate the different heat transfer patterns inside the solar collector of SCPP. Fig. 3.5.a shows the different surface of the collector and heat coefficients undergo it, and Fig. 3.5.b shows the equivalent thermal network.

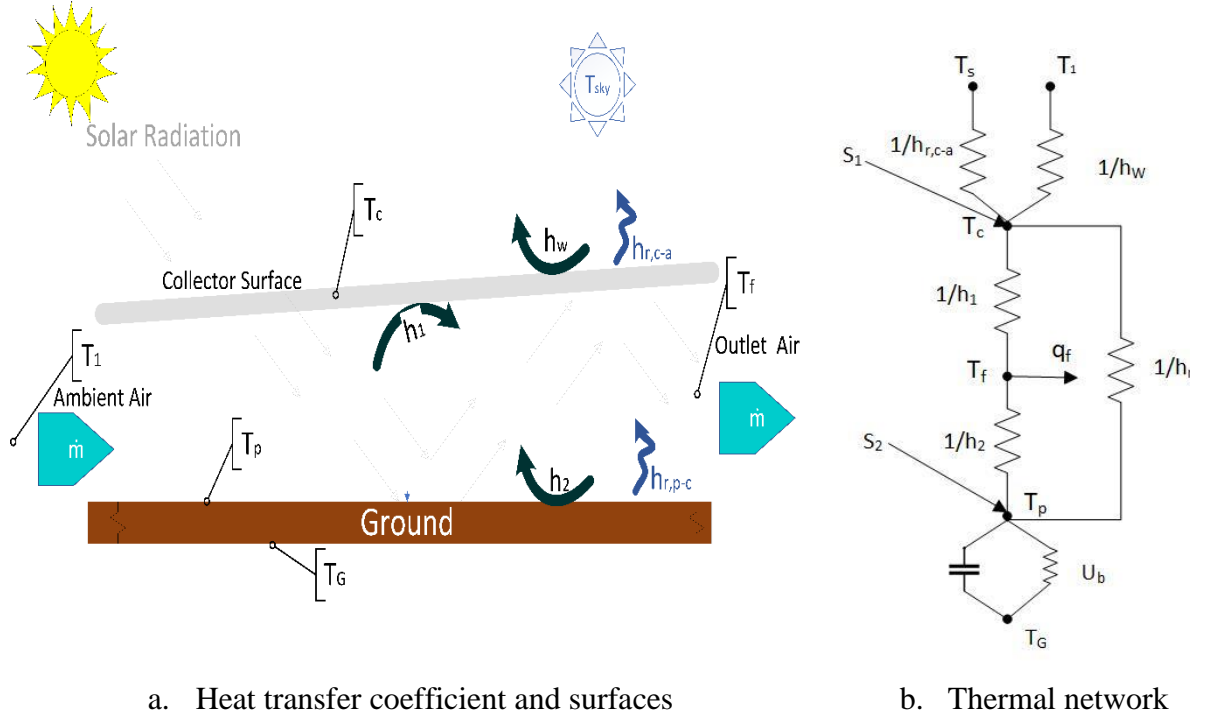


Fig. 3.5. Thermal model for the collector

By applying the heat balance on the critical point as:

$$\text{at point } T_c: S_1 + h_1(T_f - T_c) + h_{r,p-c}(T_p - T_c) = h_w(T_c - T_1) + h_{r,c-s}(T_c - T_s) \quad (3.23)$$

$$\text{at point } T_f: h_1(T_c - T_f) = q_f + h_2(T_f - T_p) \quad (3.24)$$

$$\text{at point } T_p: S_2 = h_2(T_p - T_f) + h_{r,p-c}(T_p - T_c) + U_b(T_p - T_G) \quad (3.25)$$

Where, S_1 and S_2 are the solar radiation which reach to collector cover and surface of the ground respectively. h_w is the convection heat transfer between the surrounding and the outer surface of the cover. $h_{r,c-a}$ is the radiation heat transfer coefficient between the outer surface of the cover and surrounding. h_1 and h_2 are the convection heat transfer coefficient between the inner surface of the cover and the air, and the surface of the ground and the air respectively. q_f is the gain useful heat in the air. $h_{r,p-c}$ is the radiation heat transfer coefficient between the surface of the ground and the inner surface of the cover. U_b is the ground heat transfer coefficient.

The temperature of the air changes with the radial position of the collector. Thus, Eqn. 3.23-3.25 should be solved in different radial positions to find the temperature distribution inside the collector. The arithmetic means of the air temperature, T_f , is defined as:

$$T_f = \frac{T_{f,o} - T_{f,i}}{2}. \quad (3.26)$$

The useful heat can be expressed as a function of the air temperature as:

$$q_{r,i} = \frac{\dot{m}c_p}{A_i}(T_f - T_{f,i}) = \mu_i(T_f - T_{f,i}) \quad (3.27)$$

Where \dot{m} is the mass flow rate through the SCPP, and A_i is the area of the collector at the radial position. i is a radial position of the collector in the range r_r to r_c .

By substituting Eqn 3.26 and 3.27 into Eqn 3.23-3.25 and rearranging, a 3x3 is matrix obtained:

$$\begin{bmatrix} (h_1 + h_{r,p-c} + h_w + h_{r,c-s}) & -h_1 & -h_{r,c-s} \\ +h_1 & -(h_1 + h_2 + \mu_i) & +h_2 \\ -h_{r,p-c} & -h_2 & (h_2 + h_{r,p-c} + U_b) \end{bmatrix} \begin{bmatrix} T_c \\ T_f \\ T_p \end{bmatrix} = \begin{bmatrix} S_1 + h_w T_a + h_{r,c-s} T_s \\ \mu_i T_{f,i} \\ S_2 + U_b T_G \end{bmatrix}.$$

For simplicity, the above matrix can be expressed as: $[H][T] = [S]$, the mean temperature vector can be calculated using matrix inverse technique as:

$$[T] = [H]^{-1}[S]. \quad (3.28)$$

The calculation of the temperature vector [T], is accomplished by assuming an initial value of temperatures, because the matrix coefficient [H], depended on the resultant temperatures vector [T], while computing the final value by employing iterative techniques, now, the temperature of the point ② is determined, which equal the temperature at, r_c , the smallest radial position, T_f . To calculate the condition of point ②, the equations for continuity, momentum and energy of the flow under the roof were applied by Koonsrisuk and Chitsomboon, (2013), which is expressed as:

$$p_2 = p_1 + \frac{\dot{m} q_r}{2\pi H_R^2 \rho_1 c_p T_1} \ln \frac{r_r}{r_c} - \frac{\dot{m}^2}{2\rho_1} \left(\frac{1}{A_2^2} - \frac{1}{A_1^2} \right). \quad (3.29)$$

To describe the performance of a solar collector, an energy balance analysis indicates the distribution of incident solar energy into useful energy gain, thermal losses, and optical losses. In steady state analysis, the solar radiation absorbed by a collector per unit area of absorber I is equal to the difference between the incident solar radiation and the optical losses, which can be expressed as:

$$q_r = I(\alpha_c) - U_t \Delta T \quad (30)$$

Where α_c is absorptivity of glass cover, U_t is collector loss coefficient ($W/m^2 K$), ΔT is the temperature difference between the air inside and outside a solar collector.

3.2.2. Heat transfer coefficient calculation

To solve the system of the matrix equation, the coefficient of heat transfer should be determined according to the geometry of SCPP. The equivalent sky temperature model is used to calculate the solar radiation exchange between the outer of the surface of the collector and the sky. Swinbank, (1963) presents the formula between the sky temperature, T_s , and the ambient temperature, T_1 ,

$$T_s = 0.0552T_1^{1.5}. \quad (3.31)$$

The radiation heat transfer coefficient can be expressed as:

$$h_{r,c-a} = \frac{\sigma \varepsilon_c (T_c + T_s)(T_c^2 + T_s^2)(T_c - T_s)}{(T_c - T_1)}, \quad (3.32)$$

where σ is Stefan–Boltzmann constant, which equals 5.67×10^{-8} and ε_c is an emissivity of the material cover.

The radiation heat transfer coefficient between the inter surface of the collector cover and the ground surface is considered heat transfer between two parallel plates, which is

$$h_{r,p-c} = \frac{\sigma(T_p^2 + T_c^2)(T_p + T_c)}{\frac{1}{\varepsilon_p} + \frac{1}{\varepsilon_c} - 1}. \quad (3.33)$$

The ground heat transfer coefficient is $U_b = 2b/\sqrt{\pi t}$, where $b = \sqrt{K\rho c_p}$, involve the heat transfer resistance and thermal storage effect, the experimental data of Haaf, (1984) shown the temperature of the ground is 35° (constant) at 50 cm depth, with ground heat transfer coefficient is around 1.4 W/m K at same depth(Tingzhen, Wei and Yuan, 2007).

The free convection heat transfer coefficient between the outer surface cover and the ambient is determined by formula:

$$h_w = 2.8 + 3.0 V, \quad (3.34)$$

where V is the wind speed in m/s, which is put in this model as an average value of Manzanares, Spain. This equation considers the effects of solar radiation and free convection are involved in this formula, (Duffie and Beckman, 2013) and(Pasumarthi and Sherif, 1998a).

Due to the effects of the chimney, h_1 and h_2 are force convection heat transfer coefficients. Petukhov and Popov(dos S. Bernardes, Voß and Weinrebe, 2003) obtained the mean Nusselt numbers, Nu_m , for the case of parallel plates which is valid in range $5 \times 10^5 < Re < 10^7$ and $0.6 < Pr < 2000$ as:

$$Nu_m = \frac{0.037Re^{0.8}Pr}{1+2.443Re^{-0.1}(Pr^{2/3}-1)} \quad (3.35)$$

and the convection heat transfer can be calculated as:

$$h = \frac{K}{L} Nu. \quad (3.36)$$

The optical properties have great influence on the performance of SCPP by changing the absorbed amount of the solar radiation, which is described by the following relation:

$$S_1 = \alpha_c I \quad (3.37)$$

and

$$S_1 = \tau_c \alpha_p I \quad (3.38)$$

Where I is the direct solar radiation, α_p is the absorptivity of the ground, and α_c and τ_c are the absorptivity and transmissivity of the cover material respectively.

3.2.3. Chimney

The cylindrical tower, which acts like a large chimney, is located at the centre of the canopy of the collector. It utilizes a difference in density, which results in a temperature difference between the cool air at the top and the heated air at the bottom. This creates the chimney effect, which draws air upwards from the bottom of the tower out at the top. To evaluate the change of atmospheric pressure with height, the barometric elevation formula is used that defines the atmospheric pressure p as a function of ambient pressure on ground level, p_0 , and elevation z (Kobayashi and Delahanty, 2014):

$$p(z) = p_0 e^{\frac{-g}{RT_0} z} \quad (3.39)$$

as well-known that the flow inside the chimney follows up a dry adiabatic lapse rate, thus, pressure and temperature variation of air is calculated using an adiabatic expansion process and general equations for ideal gases, and can be expressed as:

$$T_4 = T_3 - \frac{g}{c_p} H_c, \quad (3.40)$$

$$p_4 = p_1 \left(1 - \frac{g}{c_p T_1} H_c \right)^{\frac{c_p}{R}}. \quad (3.41)$$

In Fig. 3.4, Point ④ is now determined by Eqs. 3.35 and 3.36, then, point ③ requires backward calculation to determine its pressure and temperature. Therefore, by rearranging the momentum and continuity equations for the flow through a constant area chimney of height, h_c , the maximum pressure difference through the solar chimney can be expressed (Krätzig, 2013) as:

$$\Delta p_{max} = \frac{\rho_1 g h_c \Delta T}{T_1 + \Delta T}. \quad (3.42)$$

Where ΔT the temperature difference in the collector and g is gravitational acceleration. From Eq. 3.42, p_3 can be calculated as:

$$p_3 = p_4 + \frac{1}{2} (\rho_3 + \rho_4) g h_c + \left(\frac{\dot{m}}{A_c} \right)^2 \left(\frac{1}{\rho_4} - \frac{1}{\rho_3} \right). \quad (3.43)$$

By accounting the efficiency of the turbine, η_t , the temperature is:

$$T_3 = T_2 \left[1 + \eta_t \left(\left(\frac{p_3}{p_2} \right)^{\frac{k-1}{k}} - 1 \right) \right], \quad (3.44)$$

where k is specific heat ratio.

3.2.4. Turbine

A turbine of the solar chimney has an enormous influence in the SSCP plant as that extracts the kinetic energy from the hot air and transmits it to the generator. The conventional layout of the solar chimney turbine is of the axial flow type. The specifications for large wind turbines are in

many aspects similar to those ones of solar chimney turbines (Tingzhen *et al.*, 2008a) (Zhou *et al.*, 2016). The solar chimney turbine and traditional wind turbines both convert large amounts of kinetic energy in the airflow at low temperature to mechanical energy.

From the energy equation and Gibbs relation from classical thermodynamics, the theoretical power extracted by the turbine can be calculated as:

$$P = \dot{m} \int v dp = \frac{\dot{m}}{\rho_{tur}} \Delta p_{tur} = 2 \dot{m} \frac{(p_2 - p_3)}{(\rho_2 - \rho_3)}. \quad (3.45)$$

The streamline of the flow subject to change in direction by 90° at the entrance to the chimney, thus, the flow area becomes less than the chimney area which is known as vena contracta phenomena. Consequently, the highest velocity in the chimney is located near the entrance of the chimney where we have the location of the smallest flow area. This phenomenon is shown clearly in the result of computational fluid dynamics (CFD) by A. Elmagid and Keppler, (2017). The contraction coefficient, CC , is a ratio between the vena contracta area and the entrance (original) area. Batchelor, (2000) applied the streamline theory for two dimensional cases by supposing that the orifice is simply a hole in a plane wall of small thickness, then, the conclusion that the contraction coefficient is 0.61, which agrees with the experimental data. The contraction occurs within a distance from the aperture of 0.4 of its diameters.

To obtain the diffuser velocity speed-up ratio, the continuity equation is applied between point ② and ③ in Fig. 3.4 :

$$\dot{m} = A_2 V_0 \rho_2 = 0.61 A_2 V_t \rho_3 \quad (3.46)$$

Then

$$\gamma = \frac{V_t}{V_0} = \frac{\rho_2}{0.61 \rho_3} \quad (3.47)$$

Eq. 3.47 calculates the diffuser velocity speed-up ratio, which is the parameter making the blade to be sensitive to surrounding duct. So, a more suitable blade for SSCP environment can be designed by above design procedure. The mathematical model and aerodynamic design are a function of the mass flow rate that is taken from experimental data.

3.3. Optimal design of blade geometry

The main purpose of most turbines is to extract as much energy from the flow of the fluid as possible, and the different components of the turbine has to be optimized for achieving that goal. Thus, optimizing a blade design is a substantial aim of this study using a suitable solution to blade element-momentum equations, Eq. 3.11, which is incorporated with the diffuser duct. Additionally, making this design efficiently works inside SC by defining design terms of SC parameters.

The maximization of the power coefficient is done by maximizing the integrand of $a'(1 - a)$ in Eq. 3.12 as:

$$\frac{d}{da} [a'(1 - a)] = (1 - a) \frac{da'}{da} - a' = 0 \quad (3.48)$$

Eq. 3.48 is valid only if the aerofoil works under the stall region. Consequently, the relative velocity and acting force on the aerofoil are acting in the same direction as shown in Fig. 3.3,

according to notes by Wood, (2015). He also showed that λ should be around 1 or greater ($\lambda > 1$). Under this condition, (Vaz and Wood, 2016) expressed:

$$x^2 a' (1 + a') = \gamma^2 a (1 - a). \quad (3.49)$$

Using the differential Eqs. 3.12 and 3.48:

$$(1 + 2a') \frac{da'}{da} \left(\frac{x}{\gamma}\right)^2 = 1 - 2a. \quad (3.50)$$

The optimum relation between a and a' is given by combining Eqs. 3.48, 3.49, and 3.50 as:

$$a' = \frac{(1 - 3a)}{(4a - 1)}, \quad (3.51)$$

the same relation for a bare turbine is derived by Glauert, (Vaz and Wood, 2016).

To find the optimum relation between x and a , Eqs. 3.48 and 3.51 are substituted to obtain:

$$16 a^3 - 24 a^2 + \left[9 - 3 \left(\frac{x}{\gamma}\right)^2\right] a + \left[\left(\frac{x}{\gamma}\right)^2 - 1\right] = 0. \quad (3.52)$$

The optimal design of the blade is implemented by solving the blade element theory at a different radial position using MATLAB. Vaz and Wood, (2016) used the initial guess and damping error technique to solve Eq. 3.49, but in I have been used the *root* command in MATLAB my model to find exact solution of Eq.3.52. To obtain the correct root of the equation, the range from 0.2 to 0.5 is set according to results of Wood, (2015). The optimization procedure of the blade can be considered as a function of the induction factor, a , once the blade element lift and drag are available. So, *Xfoil.m* is a MATLAB function that works as a system called to run *XFoil* program. It then loads the results data of the aerofoil into a structure which you can then use in iterative algorithm. I developed the algorithm found in Fig. 3.6, The MATLAB code follows up the algorithm for the calculation of the optimum chord and the twist angle of the blade for SC turbine.

3.4. CFD model of solar chimney

Nowadays, using computational fluid dynamic (CFD) is possible to model the whole solar chimney system. However, principles of solar chimney power plants depend on many physical phenomena such as heat storage, turbomachinery, and radiation heat transfer, which increase the level of the complexity of analysing the system. To solve the governing equations of a solar chimney system, we used ANSYS CFX v18.1, which solves the conservation equation of energy, momentum, and mass with K-omega turbulence model.

3. Materials and Methods

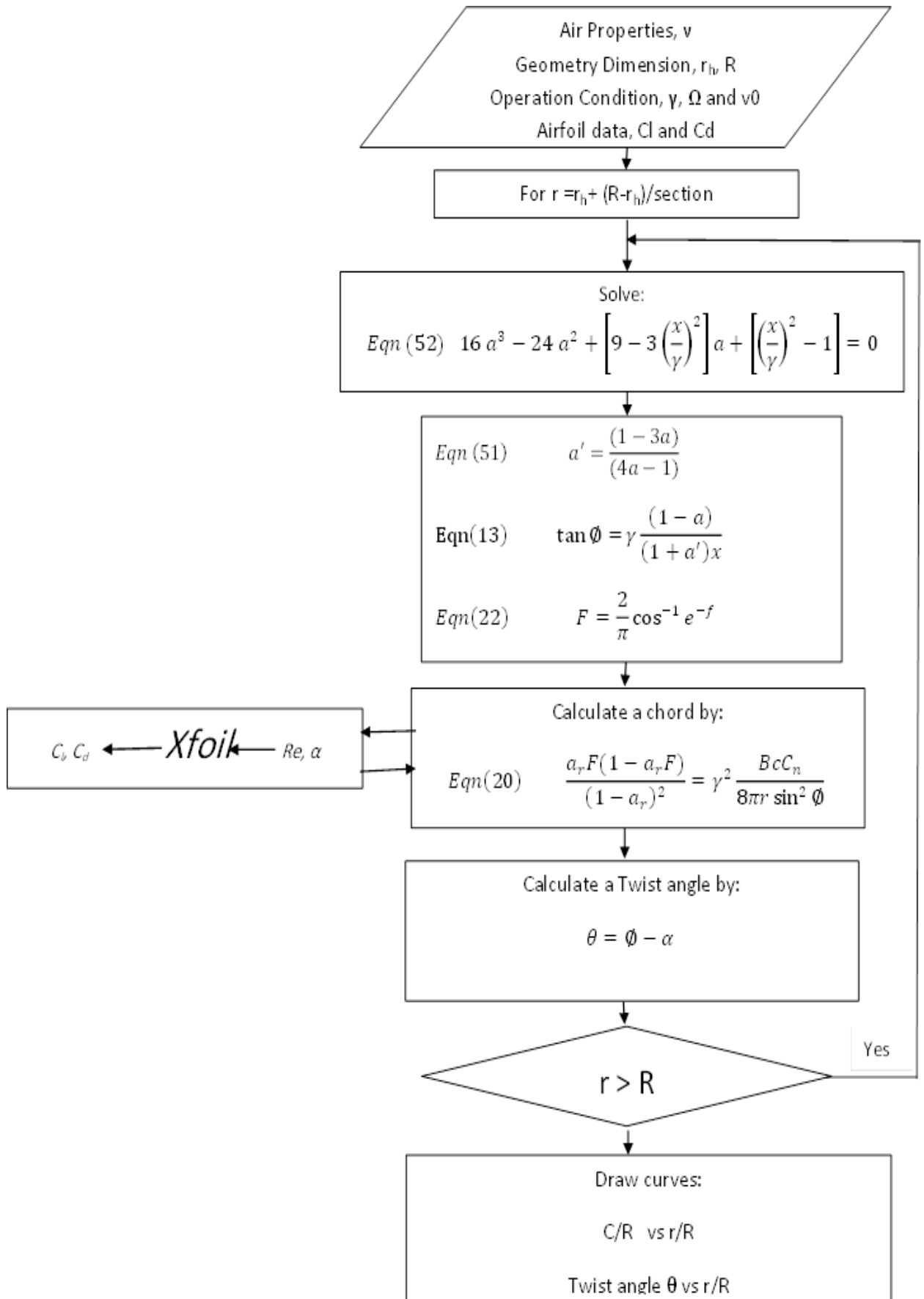


Fig. 3.6. Flow chart of the implementation of optimal design

The instantaneous equation of mass (continuity), momentum, and energy conservation are presented below:

- Mass conservation:

$$\frac{\partial \rho}{\partial t} + \nabla \cdot (\rho \vec{v}) = 0 \quad (3.53)$$

where ρ is density of the fluid, \vec{v} is the velocity vector, and t is time.

- Momentum conservation:

$$\frac{\partial(\rho \vec{v})}{\partial t} + \nabla \cdot (\rho \vec{v} \vec{v}) = -\nabla p + \nabla \cdot (\bar{\tau}) + \rho \vec{g} + \vec{F} \quad (3.54)$$

where p is the pressure, $\bar{\tau}$ is the stress tensor (described below), $\rho \vec{g}$ is the gravity force and \vec{F} are the other external body forces. By assuming the Stokes' hypothesis for Newtonian fluids, the stress tensor $\bar{\tau}$ is given by $\bar{\tau} = \mu \left[(\nabla \vec{v} + \nabla \vec{v}^T) - \frac{2}{3} \nabla \cdot \vec{v} I \right]$ Eq (3.54) are named as Navier-Stokes (NS) equations, (Carcangiu, 2008)

- Energy conservation:

$$\rho \frac{De}{Dt} = \frac{\partial(\rho e)}{\partial t} + \nabla \cdot (\rho e \vec{v}) + \nabla \cdot (\vec{v} \cdot \tau) + \vec{v} \cdot S_m \quad (3.55)$$

Where e is energy of the fluid, which write by total enthalpy $h + v^2/2$, the term $\nabla \cdot (\vec{v} \cdot \tau)$ represents the work due to viscous stresses and is called the viscous work term. This models the internal heating by viscosity in the fluid, and is negligible in most flows, and the term $\vec{v} \cdot S_m$ represents the work due to external momentum sources and is currently neglected.

To calculate radiation heat transfer, we use two radiation model: P-1 model solve the fluid domain and Monte Carlo model solve the solid domain as Surface-To-Surface configuration. The interface between turbine domain that has the rotational motion with collector and chimney domains involve the sliding mesh. We should apply frozen rotor model to solve this sliding mesh.

The buoyancy phenomena have an enormous effect in the solar chimney system, so, the buoyancy model is used. Buoyancy effects can be simulated using one of two available models in ANSYS CFX; Full Buoyancy Model (Density Difference) and Boussinesq Model, it switches between them according to the properties of a fluid.

Full Buoyancy Model (Density Difference): For single-phase flows, this model is used when the fluid density is a function of temperature or pressure (which includes all ideal gases and real fluids). Significant density variations with temperature occur for most gases. You should specify a Buoyancy Reference Density as an approximate average value of the expected domain density.

Boussinesq Model: For many applications involving buoyancy, it is sufficient to assume a constant fluid density when the change in density over the expected range of conditions is relatively small. This is often true for many liquids. When the fluid density is not a function of pressure or temperature, the Boussinesq model is employed. The Boussinesq model uses a constant density

fluid model, but applies a local gravitational body force throughout the fluid that is a linear function of fluid thermal expansivity, and the local temperature difference with reference to a datum called the Buoyancy Reference Temperature. You should specify the reference temperature as an approximate average value of the expected domain temperature (ANSYS CFX-Solver theory guide).

In commercial codes, a friendly interface gives the user the possibility of easy setting the various options and analyses the results. Three large parts are generally indicated of a CFD code, which correspond to three phases of the problem analysis. As an example ANSYS CFX, is used in present study. Fig. 3.7 shows components of ANSYS CFX v18, which present the three phases of the problem analysis.

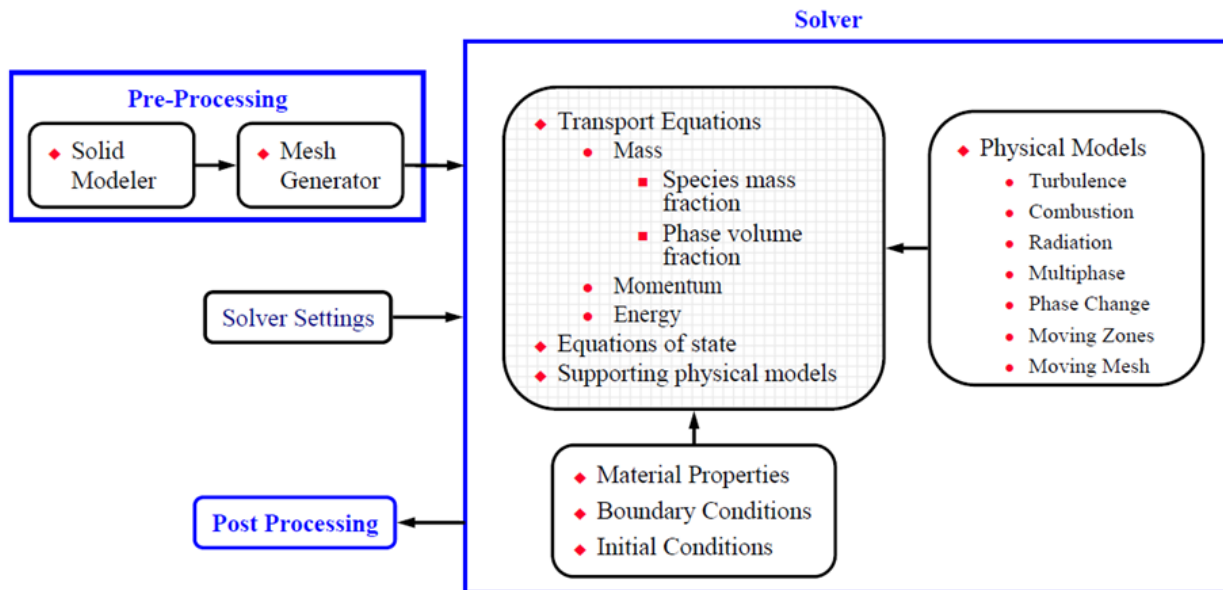


Fig. 3.7. ANSYS CFX Component

When approaching the study of fluid dynamics problems, the mathematical model is based on the fundamental mass, momentum and energy conservation principles. The Reynolds’s Averaged Navier-Stokes (RANS) equations for the compressible fluid flow are included the equations of the conservation of mass and momentum.

3.4.1. Turbulent modelling

Theoretical analysis and prediction of turbulence are being studied, and to this date still is under researching, the fundamental problem of fluid dynamics, particularly of CFD. The major difficulty arises from the random or chaotic nature of turbulence phenomena. Because of this unpredictability, it has been customary to work with the time averaged forms of the governing equations, which inevitably results in terms involving higher order correlations of fluctuating quantities of flow variables. The semi-empirical mathematical models introduced for calculation of these unknown correlations form the basis for turbulence modelling. The complexity of the mathematical models increases with the amount of information required about the flow field, and is reflected by the way in which the turbulence is modelled, from simple mixing-length models to the complete solution of the full Navier-Stokes equations.

Concerning the study of viscous flows, a laminar regime exists only at low Reynolds number. Indeed, when the Reynolds number grows, the flow field structures change and time fluctuating

velocity and pressure components appear, even though boundary conditions are still steady in a time-averaged sense. When the flow regime of Reynolds number becomes turbulent, the fluid motion looks disorganized and single particles follow a winding path. This being even if the mean are well-established paths, which is properly defined as mainstream flow. A turbulent flow has often high-level vorticity, which means also that diffusion phenomena come out for all the physical properties of the flow, both vector (e.g. momentum) and scalar (e.g. temperature).

The K-omega based Shear-Stress-Transport model (SST) was also used because of the treatment of the near-wall condition at low-Reynolds number computations. One of the great features of the K-omega turbulent model is that the model does not involve the complex nonlinear damping functions required for the K-ε model and is, therefore, more accurate and more robust. A low-Reynolds K-ε model would typically require a near-wall resolution of $y^+ < 0.2$, while a low-Reynolds number K-omega model would require at least $y^+ < 2$. It allows for smooth shift from a low-Reynolds number form to a wall function formulation (ANSYS CFX-Solver theory guide).

The first step in formulating the k-ε model is in the consideration of the second variable. Since ε has already been defined by:

$$\varepsilon = \nu \frac{\overline{u'_i u'_i}}{\partial x_k \partial x_k} \quad (3.56)$$

The starting point for calculating the second variable should be the exact equation for ε. This can be done by performing the operation:

$$L(\cdot) = \nu \frac{u'_i}{\partial x_j} \frac{\partial}{\partial x_j} (\cdot) \quad (3.57)$$

to both sides of the instantaneous, incompressible, Navier-Stokes equations.

$$\begin{aligned} \rho \frac{\partial \varepsilon}{\partial t} + \rho U_j \frac{\partial \varepsilon}{\partial X_j} &= -2\mu [\overline{u'_{i,k} u'_{j,k}} + \overline{u'_{k,i} u'_{k,j}}] \frac{\partial U_i}{\partial X_j} - 2\mu \overline{u'_k u'_{l,j}} \frac{\partial^2 U_i}{\partial X_k \partial X_j} \\ &\quad - 2\mu \overline{u'_{i,k} u'_{l,m} u'_{k,m}} - 2\mu \nu \overline{u'_{l,mk} u'_{l,mk}} \\ &\quad + \frac{\partial}{\partial X_j} \left(\mu \frac{\partial \varepsilon}{\partial X_j} - \overline{\mu u'_j u'_{l,m} u'_{l,m}} - \overline{\nu p'_m u'_{j,m}} \right) \end{aligned} \quad (3.58)$$

The physical processes represented in the ε equation involve several double and triple correlations of fluctuating velocity components. While somewhat formidable, the following physical interpretations exist for the terms in the epsilon equation. The first two terms on the right-hand side of Eqn. 3.58 represent the production of dissipation due to interactions between the mean flow and the products of the turbulent fluctuations. The next two terms on the right-hand side represent the destruction rate of dissipation due to the turbulent velocity fluctuations. Finally, the last three terms in Eqn. 3.58 represent the transport or spatial re-distribution of dissipation due to viscous diffusion, turbulent fluctuations, and pressure-velocity fluctuations.

As already mentioned, the k-ε turbulence model is based on Eqn. 3.58. It should be realized that what is actually needed in the model is a length or time scale relevant to the large, energy containing eddies, which are responsible for the majority of the turbulent stresses and fluxes.

However, the mechanism of the smallest eddies, which physically accomplishes the dissipation, are what is actually represented by Eqn. 3.58. This leads to some questions as to how relevant the exact dissipation equation is when the desired quantity is a length scale, characteristic of the large eddies. A counter-argument that the energy transfer from the large scales determines ε , and that Eqn. 3.58 builds a link between the small-scale motion and the large eddies. Actually, since the closure approximations used in modelling Eqn. 3.58 are based primarily on large-eddy scales, it is implied that the modelled equation is actually more of an empirical equation representing the transfer of energy from the large eddies to the small eddies (Celik, 1999).

The k equation is going to be used for any purpose other than lending some physical insight into the behaviour of the energy contained by the turbulent fluctuations; some way of obtaining its solution must be sought. Therefore, if the k equation is to be solved, some correlation for the Reynolds stresses, dissipation, turbulent diffusion, and pressure diffusion must be specified in light of physical reasoning and experimental evidence. The specification of these terms in the specific turbulent kinetic energy equation is generally the starting point in all one and two equation turbulence models. The method used to model the ε -equation will be considered here. The first term on the RHS side of Eq. 3.58 is given by:

$$P_\varepsilon = -2\mu[\overline{u'_{i,k}u'_{j,k}} + \overline{u'_{k,i}u'_{k,j}}] \frac{\partial U_i}{\partial x_j} - 2\mu\overline{u'_k u'_{i'j}} \frac{\partial^2 U_i}{\partial x_k \partial x_j} \quad (3.59)$$

the k - ω model solves for only the rate at which that dissipation occurs. Dimensionally, ω can be related to ε by $\omega \propto \varepsilon / k$. Another interpretation is the inverse of the time scale on which dissipation takes place, which is set by the largest eddies. The equation governing ω has traditionally been formulated based on physical reasoning in light of the processes normally governing the transport of a scalar in a fluid. Considering the processes of convection, diffusion, production, and destruction or dissipation, the model equation for ω is given by Wilcox, (1988) as

$$\rho \frac{\partial \omega}{\partial t} + \rho U_j \frac{\partial \omega}{\partial x_j} = \frac{\partial}{\partial x_j} \left((\mu + \sigma \mu_t) \frac{\partial \omega}{\partial x_j} \right) + P_\omega + D_\omega \quad (3.60)$$

where the production (P_ω) and dissipation (D_ω) of ω are modelled by $P_\omega = \alpha \frac{\omega}{k} \tau_{ij} \frac{\partial U_j}{\partial x_j}$ and $D_\omega = \beta \rho \omega^2$ respectively.

Combining these with the ω equation and the modelled k -equation gives the k - ω model (Wilcox, 1988) as the k -equation:

$$\rho \frac{\partial k}{\partial t} + \rho U_j \frac{\partial k}{\partial x_j} = \frac{\partial}{\partial x_j} \left(\left(\mu + \frac{\mu_t}{\sigma_k} \right) \frac{\partial k}{\partial x_j} \right) + \tau_{ij} \frac{\partial U_i}{\partial x_j} - \beta^* \rho k \omega \quad (3.61)$$

and the ω -equation:

$$\rho \frac{\partial \omega}{\partial t} + \rho U_j \frac{\partial \omega}{\partial x_j} = \frac{\partial}{\partial x_j} \left(\left(\mu + \frac{\mu_t}{\sigma_\omega} \right) \frac{\partial \omega}{\partial x_j} \right) + \alpha \frac{\omega}{k} \tau_{ij} \frac{\partial U_i}{\partial x_j} - \beta \rho \omega^2 \quad (3.62)$$

and the eddy viscosity: $\mu_t = \frac{\rho k}{\omega}$. Finally the constant α , β , β^* , σ_ω , and σ_k are define by Celik, (1999).

For the prediction of solar chimney performance in this study, the k - ω turbulence models have been chosen which type of Two-equation models. Two-equation models have been the most

3. Materials and Methods

popular models for a wide range of engineering analysis and research. These models provide independent transport equations for both the turbulence length scale, or some equivalent parameter, and the turbulent kinetic energy. With the specification of these two variables, two-equation models are complete; no additional information about the turbulence is necessary to use the model for a given flow scenario. While this is encouraging in that these models may appear to apply to a wide range of flows, it is instructive to understand the implicit assumptions made in formulating a two-equation model (Celik, 1999). The method is to solve for the characteristic turbulent velocity scale proportional to the square root of the specific kinetic energy of the turbulent fluctuations. This quantity is usually just referred to as the turbulence kinetic energy and is denoted by k . ω can be defined either as the rate at which turbulent kinetic energy is dissipated or as the inverse of the time scale of the dissipation. Table 3.1 shows the Physics models that are applied to our SCPPs simulations.

Table 3.1. physical models of SCPP simulations

Domain – chimney and collector	
Materials	
Air at 25 °C	
fluid definition	Material library
morphology	Continuous fluid
Settings	
Buoyancy model	Buoyant
buoyancy reference temperature	3.7735e+01 [C]
gravity x component	0.0000e+00 [m s ⁻²]
gravity y component	0.0000e+00 [m s ⁻²]
gravity z component	-9.8100e+00 [m s ⁻²]
buoyancy reference location	Automatic
Domain motion	Stationary
Reference pressure	1.0000e+00 [atm]
Heat transfer model	Total energy
include viscous work term	True
Thermal radiation model	P 1
spectral model	Gray
Turbulence model	K omega
Turbulent wall functions	Automatic
high speed model	Off
Domain - turbine	
Materials	
Air at 25 °C	
fluid definition	Material library
morphology	Continuous fluid

3. Materials and Methods

Settings	
Buoyancy model	Buoyant
buoyancy reference temperature	3.7735e+01 [°C]
gravity x component	0.0000e+00 [m s ⁻²]
gravity y component	0.0000e+00 [m s ⁻²]
gravity z component	-9.8100e+00 [m s ⁻²]
buoyancy reference location	Automatic
Domain motion	Rotating
angular velocity	rpm
axis definition	Coordinate axis
rotation axis	Coord 0.3
Reference pressure	1.0000e+00 [atm]
Heat transfer model	Total energy
include viscous work term	True
Thermal radiation model	P 1
spectral model	Gray
Turbulence model	K omega
Turbulent wall functions	Automatic
high speed model	Off
Domain - cover	
Type	Solid
Settings	
Domain motion	Stationary
Domain - ground	
Type	Solid
Settings	
Domain motion	Stationary
Domain interface – collector to cover	
Interface type	Fluid solid
Settings	
Interface models	General connection
Heat transfer	Conservative interface flux
Mesh connection	Automatic
Domain interface – collector to turbine	
Interface type	Fluid Fluid
Settings	
Interface models	General connection

frame change	Frozen rotor
Mass and momentum	Conservative interface flux
Mesh connection	GGI
Domain interface – ground to collector	
Interface type	Fluid Solid
Settings	
Interface models	General connection
Heat transfer	Conservative interface flux
Mesh connection	Automatic
Domain interface – turbine to chimney	
Interface type	Fluid Fluid
Settings	
Interface models	General connection
frame change	Frozen rotor
Mass and momentum	Conservative interface flux
Mesh connection	GGI

3.4.2. Grid generation

Grid generation converts the geometry into a format that can be understood by the CFD solver. It is often the most time consuming and tedious jobs in achieving the CFD solution. Grid generation is the most important before pre-processing step.

A structured grid is a collection of regular repeating elements. Such grids are generally represented by quadrilateral elements in 2D and hexahedral elements in 3D. Since the elements are arranged in a regular repeating pattern; the connectivity information of the elements is stored implicitly. Each cell in the grid is directly addressed by the index (i, j) in 2D or (i, j, k) in 3D. This helps in saving a lot of computational effort while performing calculations. In order to improve the overall accuracy of the CFD solution, these grids can be made finer by stretching in a particular direction so that there are a large number of closely spaced grid points in a region where large gradients need to be solved. The downside of using such grids is their inability to resolve finely around complicated geometries and over refinement away from the bodies (Digraaskar, 2010).

Unstructured meshes consist of arbitrarily shaped elements, which do not have any regularity among them. Such type of grids is mostly used to perform finite volume and finite element calculations. The main advantage of using unstructured meshes is their ability to resolve finely around very complex geometric topologies. Such type of meshes is generally represented by triangles in 2D and tetrahedrons in 3D geometries. Since there is no repeating pattern of the elements, the connectivity information of the elements needs to be stored explicitly. This comes at some additional computational cost since extra memory is utilized in storing the mesh connectivity information. The advantage is that, algorithms exist to fill any space, no matter how complex the shape is, with an unstructured mesh.

With the latest developments in the meshing algorithms, various mesh generators are equipped with advanced meshing options that give the user considerable control in generating very accurate unstructured meshes. Fig. 3.8 shows a cylindrical domain with typical unstructured (tetrahedral) mesh around a 3D finite cylinder. Unstructured meshes are used throughout this research so that accurate CFD calculations can be performed over the wind turbine blades, which have reasonably complex geometry,(Digraskar, 2010).

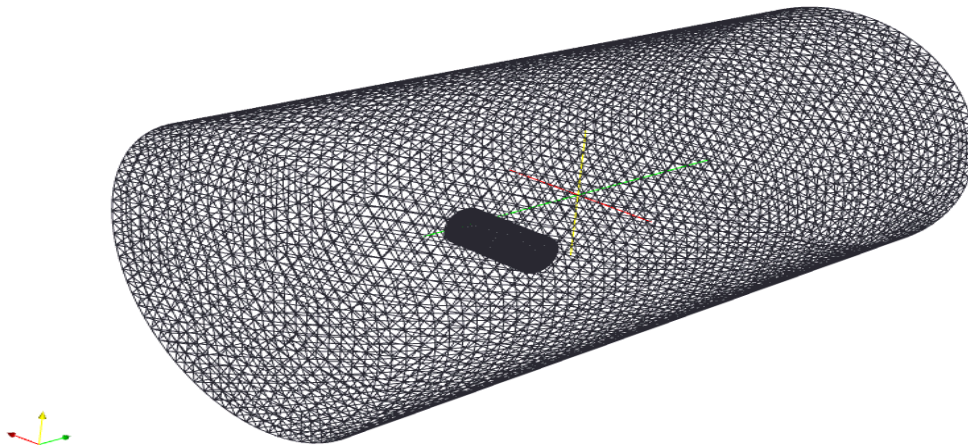


Fig. 3.8. A 3D unstructured grid around a finite cylinder consisting of tetrahedral elements(Digraskar, 2010)

As mentioned, the SCPP unit consists of ground, cover collector, chimney and fluid zone. All component geometry is drawn as 3D using SOLIDWROKS, as shown in Fig. 3.9 (light green is Cover collector, blue is Fluid zone and yellow is ground area). The ANSYS Design Modeler is used to enter CAD file, which is a part of ANSYS Workbench 18. It able to read CAD file and transfer data reading to grid generation program such as Meshing or turbo grid. However, ANSYS Meshing is used that suitable for SCPP geometry. This technique has many advantages, reading shape with high accuracy and save time and labour needing to enter data. The geometry of SCPP in Fig. 3.9 is divided into three zones: the first zone is the fluid section that has a blue colour, the second zone is the ground section that has a brown colour and the third zone is the glass cover of the collector that has a green colour. This division process gives us the ability to use different materials domain on the ANSYS CFX model. Additionally, similar methods are applied for creating collector has a circular shape.

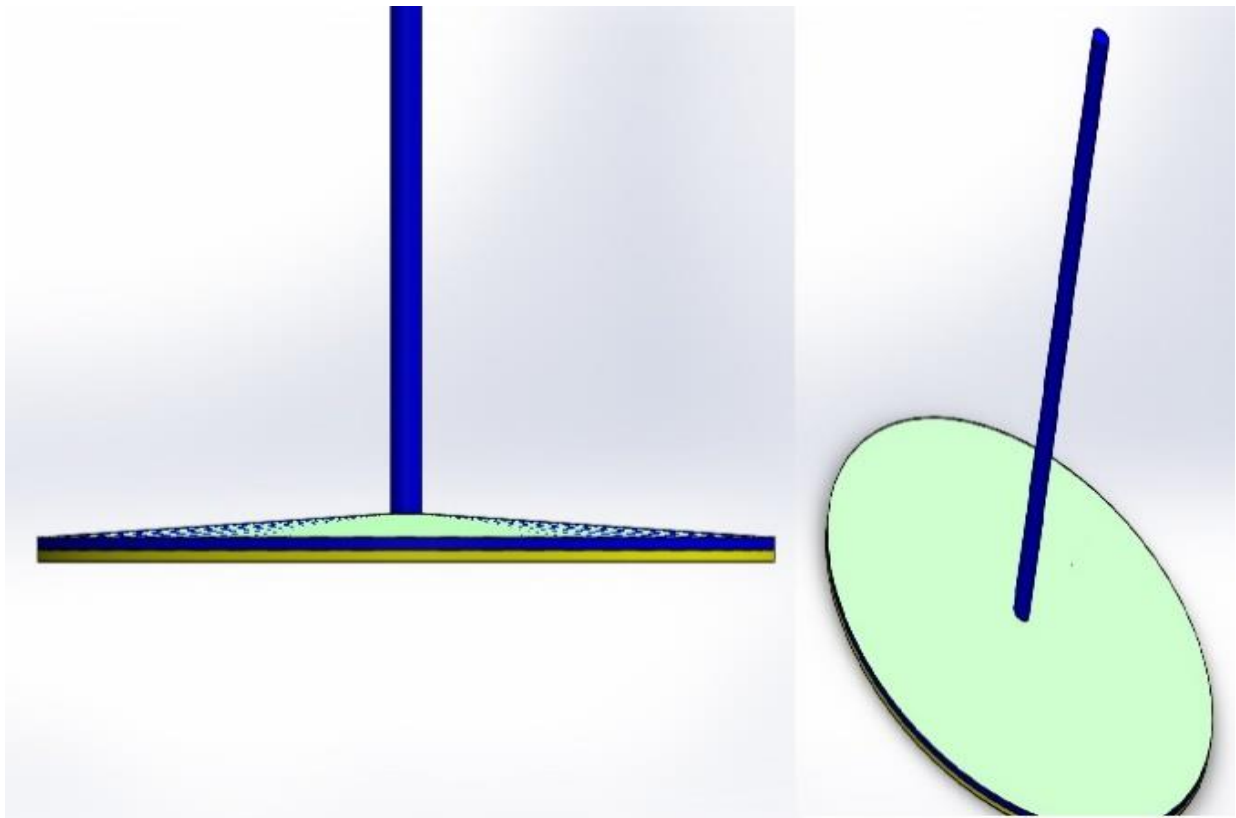


Fig. 3.9. Three-dimension geometry of solar chimney prototype

Grid generation is very important to generate accurate grids for the solver to obtain correct results. The accuracy of the CFD solution depends on the quality of the grid used to perform the calculations. Fig. 3.10 show the overall model grid. The accuracy of the CFD calculations depends on the quality of the grid that is used. The turbine domain needs a finer grid, as shown in Fig. 3.11, because it includes the rotating blade. The rotation of the turbine blade gives rise to the high intensity of the turbulence in the flow field.

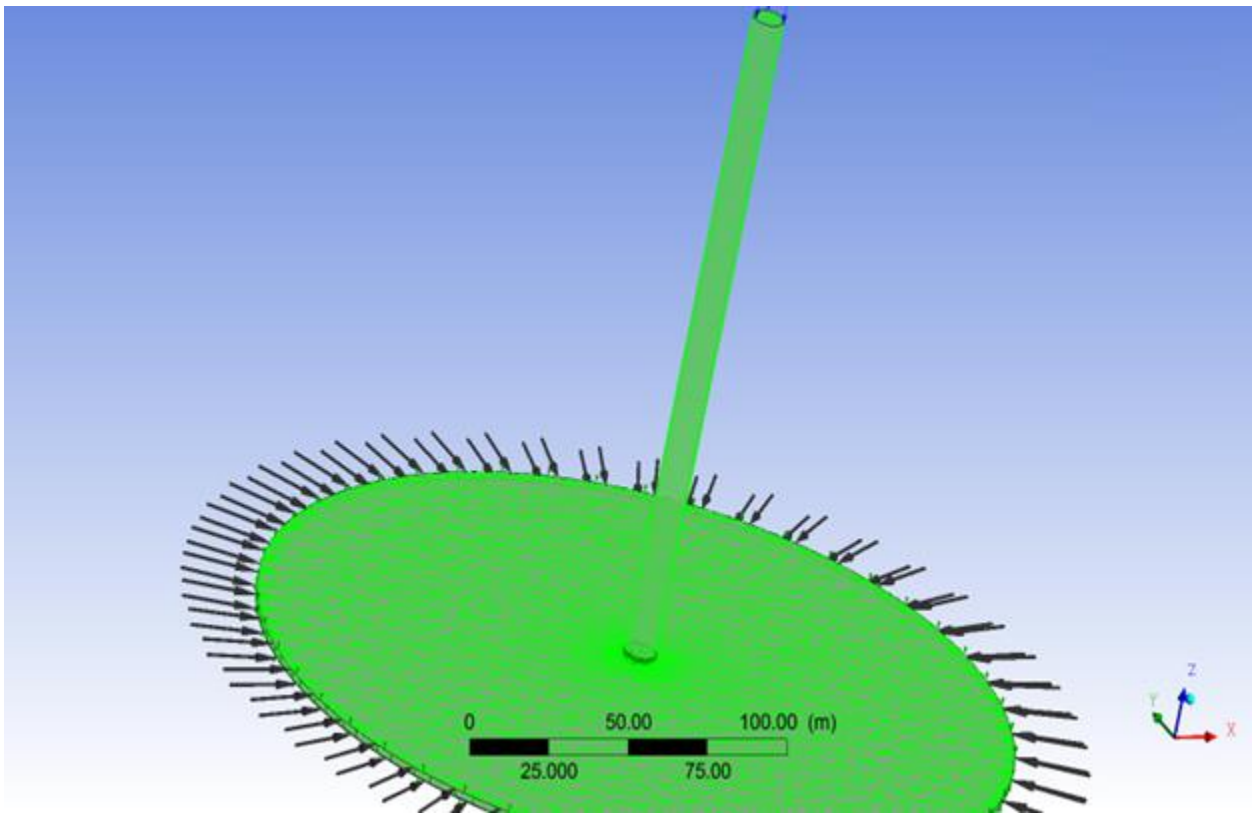


Fig. 3.10. Grid of the solar chimney unit

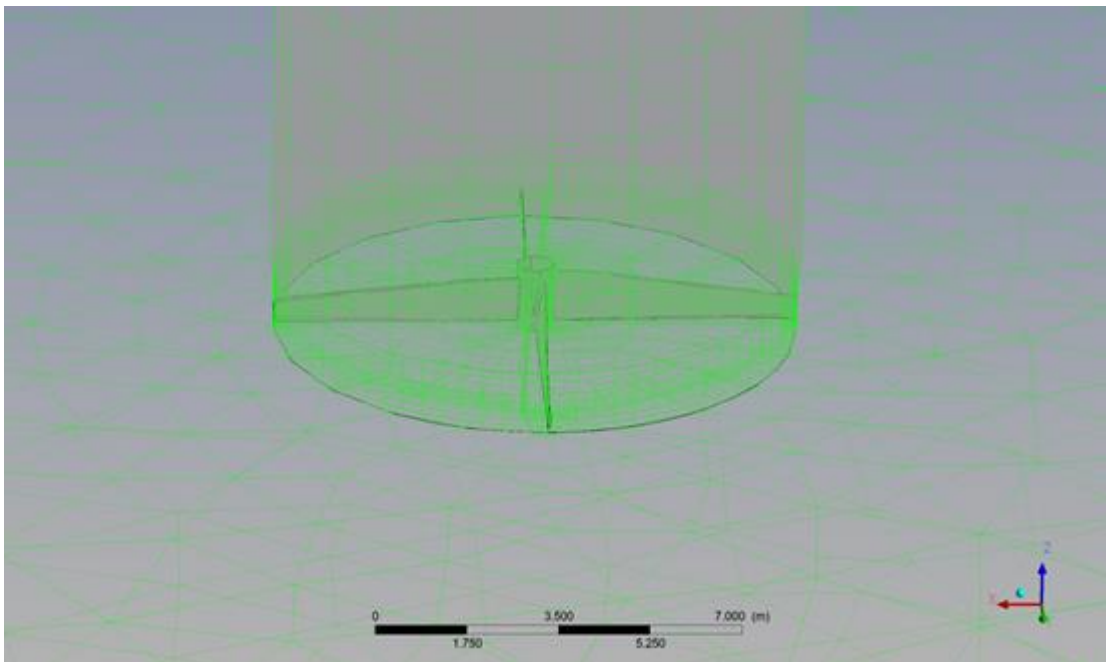


Fig. 3.11. Mesh of the turbine domain

The calculation of the model with different number of nodes has been carried out as show in Fig. 3.12 The theoretical outpower and mass flow rate through the turbine is chosen to compare the output results and decide the appropriated number of nodes, the calculation show that the around 2.5 million of the nodes is qualified for this simulation and we used 3 million number of nodes in this model calculation. Table 3.2 shows inlet parameters for model to make grid independence test and the full detail of the boundary conditions are demonstrated in Section 3.4.3.

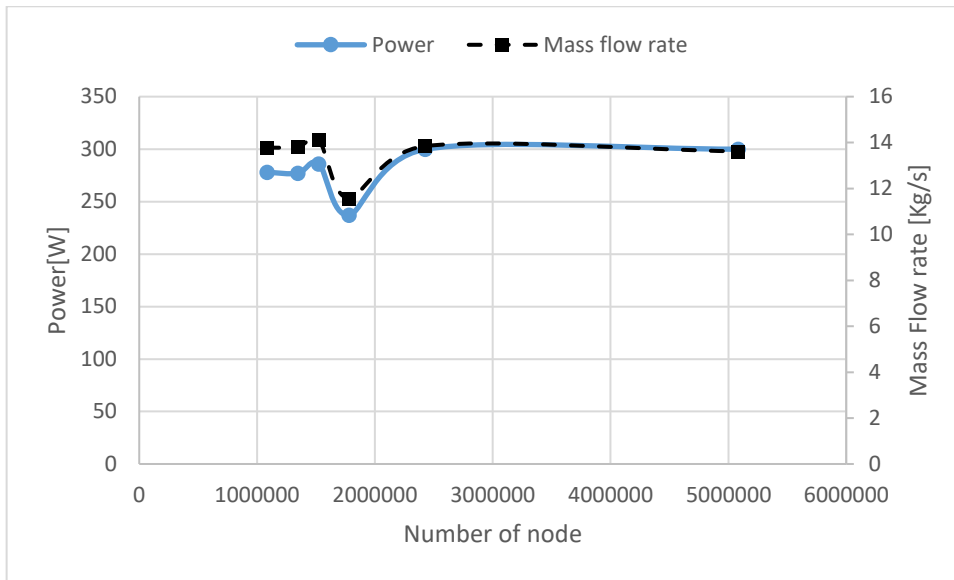


Fig. 3.12. Grid- independence test calculations

Table 3.2 Inlet parameters for grid-independence test

Inlet velocity	8 m/s
Number of turbine blades	4
Rotational speed of the turbine	840 rpm
Diameter of the turbine	1m
Height of chimney	30 m

3.4.3. Boundary conditions

Boundary conditions have serious implications on the CFD solution. This further reinforces the requirement to define suitable boundary conditions that appropriately mimic the real physical representation of the fluid flow. In many real applications, there is always great difficulty in defining in detail some of the boundary conditions at the inlet and outlet of a flow domain that is required for an accurate solution. A typical example is the specification of turbulence properties (turbulence intensity and length scale) at the inlet flow boundary, as these are arbitrary in many CFD problems. Nevertheless, by carrying out an uncertainty analysis, the reader can develop a good feel of the appropriateness and inappropriateness of the boundary conditions that are being imposed within the physical context of the CFD problem being solved.

The pursuit of setting proper physical boundary conditions like in the section of local refinement and solution adaptation also governs the computational stability and the numerical convergence of the CFD problem. In many real applications, there is always great difficulty in prescribing some of the boundary conditions at the inlet and outlet of the computational domain. Boundary conditions fields with the pressure distribution. In the context of CFD, defining suitable boundary conditions generally encompasses the specification of two types of boundary conditions: the

Dirichlet and Neumann boundary conditions. For brevity, the Dirichlet boundary condition can be simply defined for the transport property, ϕ , as the requirement of specifying the physical quantity over the boundary (Tu, Yeoh and Liu, 2018), such as the following:

$$\phi = f(\text{analytic}) \quad (3.63)$$

The Neumann boundary condition involves, however, the prescription of its derivative at the boundary given by

$$\frac{\partial \phi}{\partial n} = 0 \quad (3.63)$$

The step in the Pre-processing is setting up the boundary condition. Boundary condition will be different for each case. In Cartesian coordinate, the location of boundary condition feature (inlet, outlet, shroud, etc.) can be linked to name objects defined during the grid generation procedure. This obviates the need to enter the coordinate twice: one when defining the grid, and again when specifying boundary condition. As general rule, a physical meaningful boundary condition, such as a specified pressure should be used at out flow boundaries whenever possible.

The accuracy of the simulation model results substantially depends on the imputed boundary condition. Table 3.3 shows the location and value of the used boundary condition in Aswan SCP model. The height of the chimney is considered by evaluating the change of atmospheric pressure with height as well-known that the flow inside the chimney follows up a dry adiabatic lapse rate. Direct radiation and rotational of the turbine are taken from experimental data, because of continuously changing with time. The surface of the ground that contact with air exposed to solar radiation less than outer cover surface by glass transmissivity. To clarify the different performance of collectors within various shapes, we use the boundary condition in Table 3.3 for two CFD models.

Table 3.3. The boundary condition of the CFD models

Domain	Boundaries	
Chimney	Boundary - domain interface 2 side 2	
	Type	Interface
	<i>Settings</i>	
	Heat transfer	Conservative interface flux
	Mass and momentum	Conservative interface flux
	Thermal radiation	Conservative interface flux
	Turbulence	Conservative interface flux
	Boundary - outlet	
	Type	Opening
	<i>Settings</i>	
	Flow direction	Normal to boundary condition
	Flow regime	Subsonic
	Heat transfer	Opening temperature
	Opening temperature	3.7735e+01 [c]

3. Materials and Methods

	Mass and momentum	Opening pressure and direction
	Relative pressure	1.0110e+05 [pa]
	Thermal radiation	Local temperature
	Turbulence	Medium intensity and eddy viscosity ratio
Collector	Boundary – collector to cover side 1	
	Type	Interface
	<i>Settings</i>	
	Heat transfer	Conservative interface flux
	Mass and momentum	No slip wall
	Boundary - domain interface 1 side 1	
	Type	Interface
	<i>Settings</i>	
	Heat transfer	Conservative interface flux
	Mass and momentum	Conservative interface flux
	Thermal radiation	Conservative interface flux
	Turbulence	Conservative interface flux
	Boundary – ground to collector side 2	
	Type	Interface
	<i>Settings</i>	
	Heat transfer	Conservative interface flux
	Mass and momentum	No slip wall
	Boundary - inlet	
	Type	Opening
	<i>Settings</i>	
	Flow direction	Normal to boundary condition
	Flow regime	Subsonic
	Heat transfer	Static temperature
	static temperature	4.5940e+01 [c]
Mass and momentum	Opening pressure and direction	
relative pressure	1.0000e+00 [atm]	
Thermal radiation	Local temperature	
Turbulence	Medium intensity and eddy viscosity ratio	
Cover	Boundary – collector to cover side 2	
	Type	Interface
	<i>Settings</i>	
	Heat transfer	Conservative interface flux
	Boundary – inlet of solar radiation	

	Type	Wall
	<i>Settings</i>	
	Heat transfer	Adiabatic
Ground	Boundary – ground to collector side 1	
	Type	Interface
	<i>Settings</i>	
	Heat transfer	Conservative interface flux
Turbine	Boundary - domain interface 1 side 2	
	Type	Interface
	<i>Settings</i>	
	Heat transfer	Conservative interface flux
	Mass and momentum	Conservative interface flux
	Thermal radiation	Conservative interface flux
	Turbulence	Conservative interface flux
	Boundary - domain interface 2 side 1	
	Type	Interface
	<i>Settings</i>	
	Heat transfer	Conservative interface flux
	Mass and momentum	Conservative interface flux
	Thermal radiation	Conservative interface flux
	Turbulence	Conservative interface flux
	Boundary - rotor	
	Type	Wall
	<i>Settings</i>	
	Heat transfer	Adiabatic
	Mass and momentum	No slip wall
	Wall roughness	Smooth wall

3.4.4. Coupled fluid–structure interaction simulations

Generally, wind turbines are subjected to rapid variations in wind speed and direction. This stochastic inflow, associated with the architecture of the rotor leads to a 3D unsteady aerodynamics and dynamic stall. The dynamic stall results in fluctuating blade force and blade oscillations, known as aeroelastic phenomena. Problems of aeroelastic stability can be encountered on the new large wind turbine blades as well as on the rotating wind turbine blades and on parked wind turbine blades at high wind speeds (Guerri, Hamdouni and Sakout, 2008). Coupled fluid-structure interaction (FSI) simulations at full scale are essential for accurate modelling of turbine blades. The motion and deformation of the turbine blades depend on the air flow, and the air flow patterns depend on the motion and deformation of the blades. A significant computational challenge is the

high air velocity, complex and sharp geometric features and sizes of turbines under consideration (Bazilevs *et al.*, 2011).

There are generally two types of methods used to calculate the fluid–structure interaction problems in the time domain; in these methods, the fluid and structure governing equations are loosely coupled or fully coupled. In a loosely coupled model, the structural response lags behind the flow field solution. This type of method may be limited to first-order accuracy in time, regardless of the temporal accuracy of the individual solvers. In the fully coupled model, the flow field and structure always respond simultaneously by exchanging the aerodynamic forcing and structural displacement within each iteration. Obviously, only the fully coupled model is rigorous in the physical sense (Chen and Zha, 2005).

The solar chimney turbine acquires enormous importance from its task in the SCPP plant, converting the kinetic energy of air into mechanical energy, and then transmitting it to the generator. The blades of such turbines are so designed that they generate lift from wind and thus rotate. The motion and deformation of the wind turbine blades depend on the rotational speed and air flow velocity, and the air flow patterns depend on the motion and deformation of the blades. Thus, coupled fluid–structure interaction (FSI) simulations at full scale are essential for accurate modelling of solar chimney turbine blades. The main aim of this calculation is the analysis of the stresses resulting from aerodynamic forces in addition to the computation of the first natural frequencies of the rotor blade.

This is as a primary step towards fabrication of the blades for experimental work. After an in-depth study of the aerodynamic configuration by ANSYS CFX in our previous study, the finite element analysis of a solar chimney turbine blade is carried out using ANSYS Mechanical Model. Solar chimney turbine blades were designed by solving blade element theory with a diffuser to obtain the optimization of the turbine blade chord and twist angle distributions in the presence of a diffuser. Most of the structure failures of wind turbines occur in the blade root section. Hence, the representation of the exact geometry of the turbine rotor (hub and blades) have been analysed. pressure distribution of the airflow and rotation speed act the rotor of solar turbine and generate the most of the load on the rotor material, so, the boundaries condition on the mechanical model.

3.5. Experimental apparatus

The experimental work aims to demonstrate that the designed turbine can operate efficiently over the required range of mass flows and pressure drops that saved by Solar chimney power plants (SCPPs). Additionally, the experiment assists to quantify the turbine performance and gain a better understanding of the turbine operation. The experimental results can also find differences in predicted and real operations, this leads to further improvements in the turbine design. The following points show the main finding of this experimental work:

- Demonstration that the solar chimney turbine operates effectively over the predicted design range.
- Quantification of the performance of the turbine over the design range and also performance outside of the design range.
- Verification of design performance prediction and comparison of simulated and experimental results.
- Verification of design assumptions and possible modification of these.

- Use of results to improve turbine prediction model and suggestion of improvements to turbine design.

3.5.1. Layout of experimental rig

The rig of the experiment should allow for a detailed investigation of the turbine performance and satisfy the design objectives listed above. In this study, we chose the wind tunnel technique to test the solar chimney turbine, a wind tunnel is usually used for testing turbomachines because it saves the criteria of the operation condition during testing by strictly controlling inflow conditions. The blades and hub are a main construction of the conventional axial flow turbine; the blade consists of the aerofoils that interact with the hot air and convert the power in the air to mechanical power. The geometry and dimensions of the blades are determined by characteristics flow of SCPP to make it an optimum. 3D printing is used to manufacture blades of turbine prototype according to calculations that is shown in detail in above sections 3.1 and 3.3. Appendix A.3A.3 shows the full dimensions of my design blade and engineering drawing of the hub.

The tested prototype comprises the four-blade turbine rotor, which connects to the electrical generator that working as the load of the turbine. The hub is the part that transmits all the power and loads from the blades to the generator shaft. We designed the hub as two parts that makes it can change the angle of the blades, and easy to manufacture and assemble by 8 bolts. Fig. 3.13 shows the 3D of one side of the hub, and Fig. 3.14 shows the prototype hub, which manufactured of polyethylene.

The electric system takes a part of our measurement, comprises the generator and electric heater, works as a load of the turbine. A 1800A007 Mitsubishi Alternator was used on the measurement, it is designed for the car Diesel engine, therefore; the challenge comes. The range of the rotational speed of the car engine is higher than the turbine ones. I get a lot of help from Mr. Gábor Bércesi, a Ph.D. student to modified the exiting circuit of the generator. This change makes the generator is more suitable for a rotational speed range of the turbine.



Fig. 3.13. 3D of the turbine hub

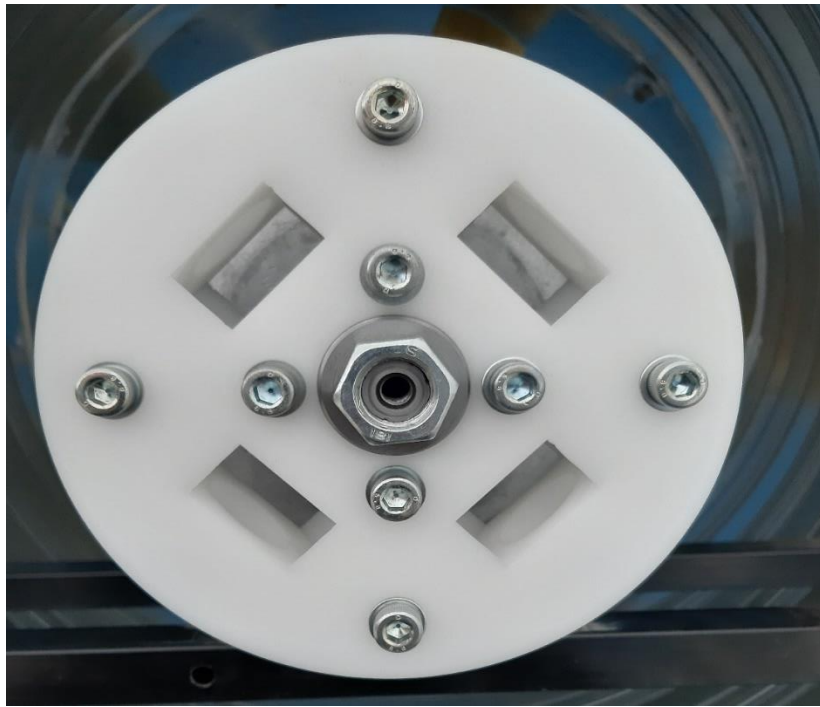


Fig. 3.14. The hub of the tested turbine

The experiment is carried out in the energy laboratory, Szent István University at Gödöllő campus. We used the wind tunnel, 8 m of length and 1 m of the square/circle cross-section, as shown in Fig. 3.15. Its first block from the inlet side has the laminar basket for damping the inference of surrounding. The draft fan connects with the suitable inverter, the inverter saves a proper control of the rotational speed of the fan, consequence, providing the control of the airflow velocity.



Fig. 3.15 The wind tunnel at Szent István University at Gödöllő campus

3.5.2. Measurement strategy

To evaluate the performance of the solar chimney turbine from the experimental rig, certain physical properties have to be measured, then, the dimensionless variables have to be determined from this measured quantity. The Physics quantity as:

- Airflow velocity, v_{in}
- Pressure drops around turbine, $\Delta p_{tur,st}$
- DC Voltage, V
- DC Current, I
- Outside Air temperature and humidity
- Reference pressure
- Rotational speed of the turbine

Fig. 3.16 shows the schematic and layout of the wind tunnel testing for the designed turbine. After fixation the rotor of the turbine on the generator shaft and the prob of the sensors as shown in Fig. 3.16, the procedure of the solar chimney turbine will be carried out by following the next steps:

- 1- Turn on the fan on the low speed and check the sensors reading on the laptop screen.
- 2- Adjust the fan on the required speed by setting frequency as 10, 15, 20, 25 then 30 Hz and waiting for few minutes to achieve steady state operation.
- 3- Change excitation voltage of the generator
- 4- Start recording the data logger and manual reading (Cooling water temperature, electric power, voltage, and current) for about 15 minutes
- 5- Stop the fan and prepare to the next reading
- 6- Repeat the above steps with a new speed

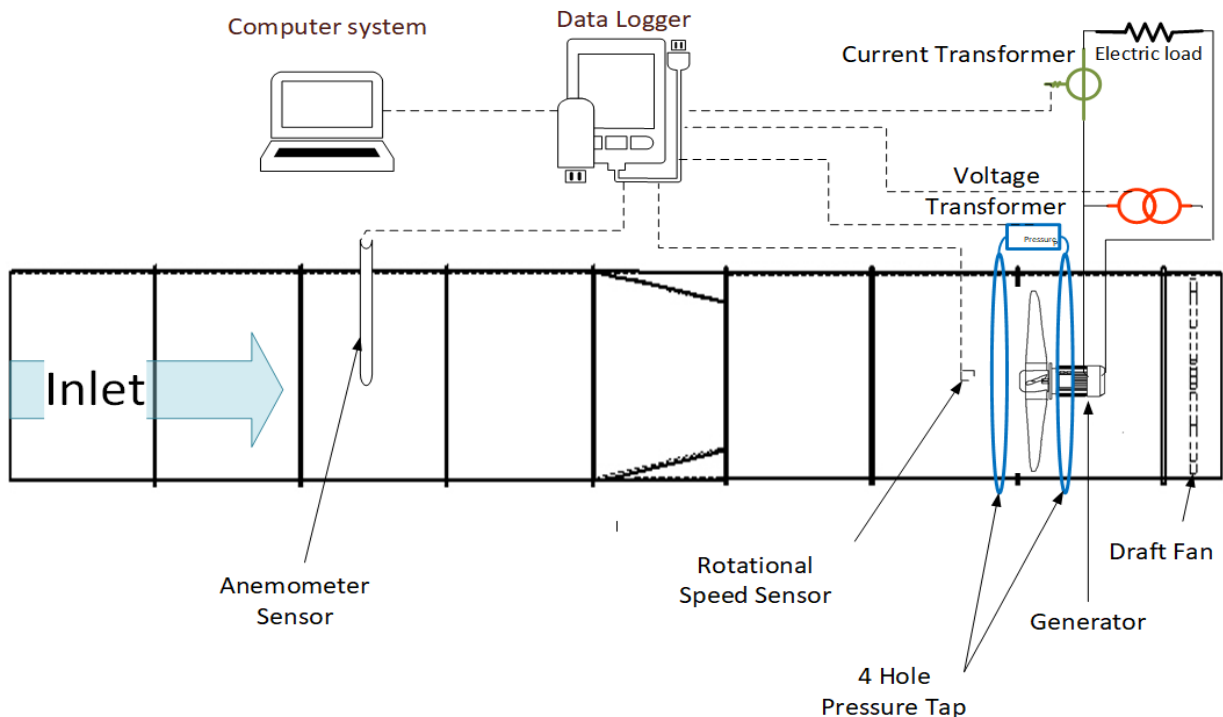


Fig. 3.16. Schematic diagram of testing the turbine within wind tunnel

3.5.3. The sensors of the measurements

Many sensors were used in this work, all sensors connect to the data logger of ALMEMO 2590-9, which has 8 channels for sensors, as shown in Fig. 3.17 and two channels for communication computer or other data logger. ALMEMO Control 5.20 software is used on the computer system to read the recorded value, then making it presentable. Fig. 3.18. Locations of the sensors on the wind tunnel

19 shows the location of the sensors inside the wind tunnel the more details about each sensor as following:

- *Anemometer*

One of the main parameters that affects the performance of the turbine is the inlet air velocity. FVAD 15-H series hot-wire anemometer instrument was used to measure the air velocity then the air mass flow can be calculated by multiplying with the cross-section area and the air outlet density. The measuring range is 0.3 to 40 m/s. The anemometer works with ALMEMO 2590-9 Data logger. The accuracy is $\pm 2\%$ with mentioned working range. The air flow rate had been measured 2.5m from the inlet of the wind tunnel as shown in Fig. 3.18.

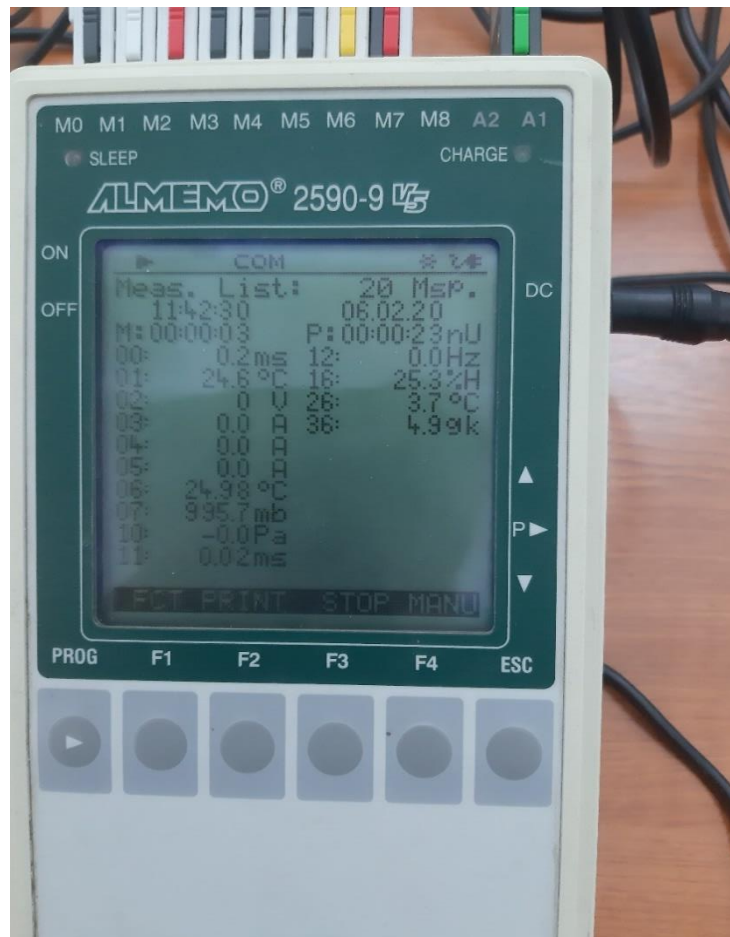


Fig. 3.17. The data logger

3. Materials and Methods

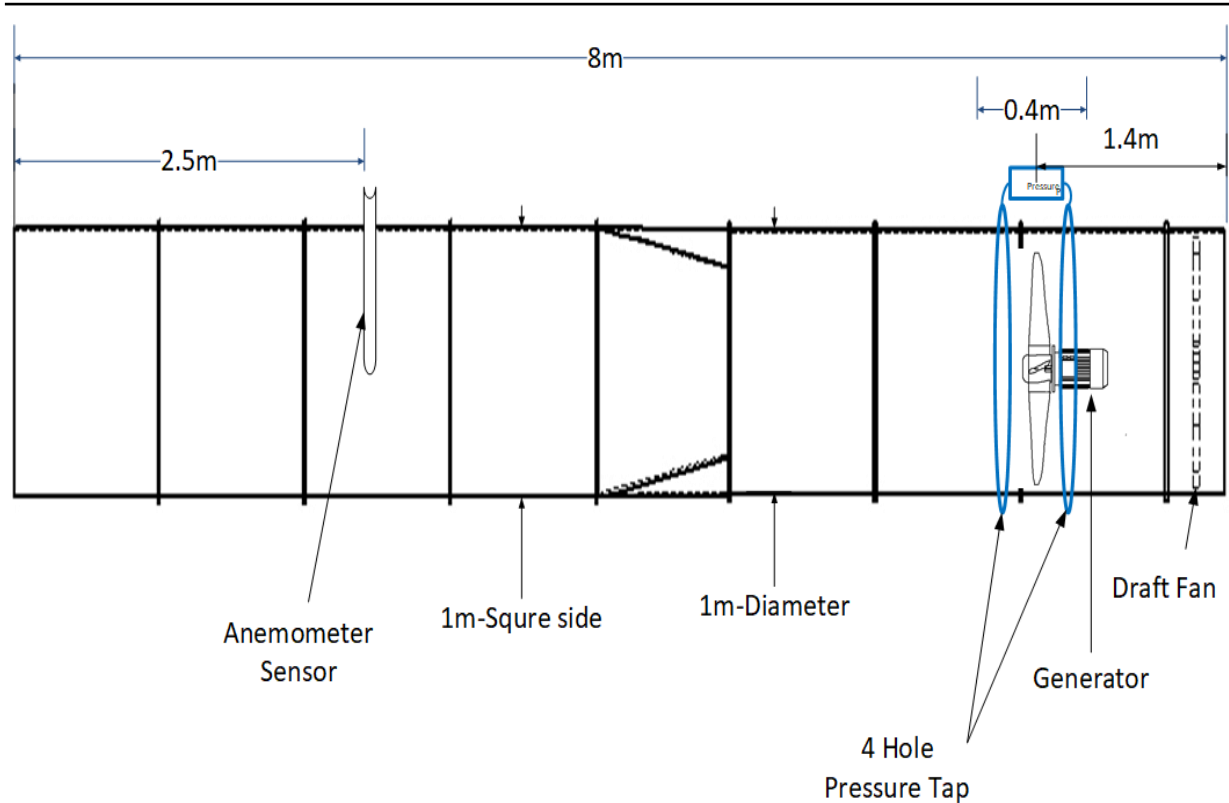


Fig. 3.18. Locations of the sensors on the wind tunnel

- *Pressure gauge*

The effect of the turbine on the airflow reveals by the pressure drop of it, the pressure difference around the turbine indicates to us; the quantity of power that the turbine can absorb from the airflow. An FDA 602 S1K / S6K Differential pressure is used to measure the pressure drop around the turbine, it has Max. common mode pressure 700 mbar within -10 to +60 °C, 10 to 90% RH, and its dimension is 74 x 20 x 8.8 mm. Fig. 3.19 shows the pressure sensor, which also can work with ALMEMO 2590-9 Data logger and its Accuracy is $\pm 0.5\%$ of final value in range zero to positive final value.



Fig. 3.19. Differential pressure sensor

- *Room condition*

The surrounding environment of the wind tunnel (room condition) influences the accuracy of reading: So, it was monitoring to sure it is a constant. Thus, a FDAD 12 SA atmospheric pressure sensor and a FHA 646 E1C capacitive humidity sensor are used to achieve this purpose. Table 3.4 show the instruments specifications.

3. Materials and Methods

Table 3.4. specification of room condition monitoring sensors

Parameter	Atmospheric pressure sensor	Humidity sensor
Measuring range	300 to 1100 mbar	0 to 100 % rh
Accuracy	± 2.5 mbar in the range	$\pm 2\%$ rh in the range $< 90\%$
Connection with data logger	yes	yes
Extension cable	no	yes
Size	62 x 20 x 7.6 mm	12 ϕ x 155 mm

4. RESULTS AND DISCUSSIONS

In this chapter, the theoretical results of both mathematical and CFD models of a solar chimney power plant (SCPP) are presented and discussed. We explain how to use the presented result in aerodynamic theories to get the turbine. The main finding of this study is a new design of the solar chimney turbine that is also presented in this chapter. Finally, the results are shown the performance of SCPP with new turbine.

4.1. The mathematical model of solar chimney power plant

As showing the comprehensive mathematical model that I improve on many points, it depended on easily measured parameters such as ambient conditions and up-wind velocity of the chimney, additionally optical material properties. Table 4.1 shows Manzanares SCPP prototype dimensions that are adopted from results of Haaf, (1984) and constant values that are used on the calculations. The measured data was carried out at noon (12:00) of September 2nd, 1982. The optical properties of the SCPP material was found in detail in (Haaf *et al.*, 1983) and (dos S. Bernardes, Voß and Weinrebe, 2003). To validate the mathematical model, calculated results are compared with the experimental results of the prototype from Manzanares, Spain, as shown in Table 4.2 accorded at 12:00. The deviation of the collector loss coefficient, the collector exit temperature, the pressure drops of the turbine, and output power are 1.808%, 5.943%, 6.668% and 0.5909% respectively, which are acceptable value.

Table 4.1. Geometrical dimensions and constant value of the pilot plant in Manzanares, Spain

Geometrical dimensions	
Mean roof radius, r_r	122 m
Average roof height, h_R	1.85 m
Tower height, h_c	194.6 m
Tower radius, r_c	5.08 m
Physical constant value	
Thermal conductivity, k	0.0321 W/m K
kinematic viscosity, ν	24.11e-6 m ² /s
Collector absorption coefficient, α	0.6897
Cover emittance (Glass optical properties), ε	0.9
Stefan-Boltzmann constant, σ	5.6697e-8 W/m ² K ⁴
Constant Pressure Heat coefficient, cp	1000.5 J/Kg.k

Table 4.2. Comparison between measured data and theoretical results

	Measured	Calculated	Error
Collector loss coefficient, U_t (W/m ² K)	15	14.7288	1.808%
Temperature at collector exit, T_2 (°C)	38	40.2583	5.943%
Pressure difference of turbine, Δp_{tur} (mbar)	0.75	0.7	6.668%
Power, P (kW)	48.4	48.686	0.591%

Using Eq. 3.47, the main aim of the mathematical model is achieved by obtaining the value of the diffuser velocity speed-up ratio be 1.6403 at the design point that is shown by Haaf *et al.*, (1983). Fortunately, this value is near the value shown by Phillips, (2003). Also, he found that the diffuser efficiency of 0.8, the optimal value are an $a_{opt}=0.4$ and $\gamma_{opt} = 1.6$ that achieve $C_{P,opt}= 0.76$. Additionally, according to Eq. 3.8 increasing γ causes more increase to the power coefficient of the turbine.

4.1.1. Temperature profile of the collector

The solar Chimney Power Plant (SCPP) is influenced by many parameters that influence the performance of the turbine; however, the solar radiation and mass flow rate are essential variables, which should be studied. The collector is divided into sections at radial position and I applied Eqs. 3.28 and 3.26 on every section, I calculate variation of the temperature through the radial direction of the collector. Fig. 4.1 shows the variation of the temperature profile with solar radiation at constant mass flow rate of 796.96 Kg/s. The increase in the solar radiation causes more increase in the outlet temperature of the collector, but the temperature differences between the inlet and the outlet of the collector, ΔT_C , are 8.66, 15.17 and 19.80°C at solar radiation 650, 850, and 1050 W/m² respectively. Fig. 4.1 clearly shows that the temperature difference is reverse proportional to the solar radiation, because of the increase the heat loss into a surrounding with increasing temperature. For generating more power, the solar radiation also suffers from other limitation; it depends on the weather condition so this variable is not controllable.

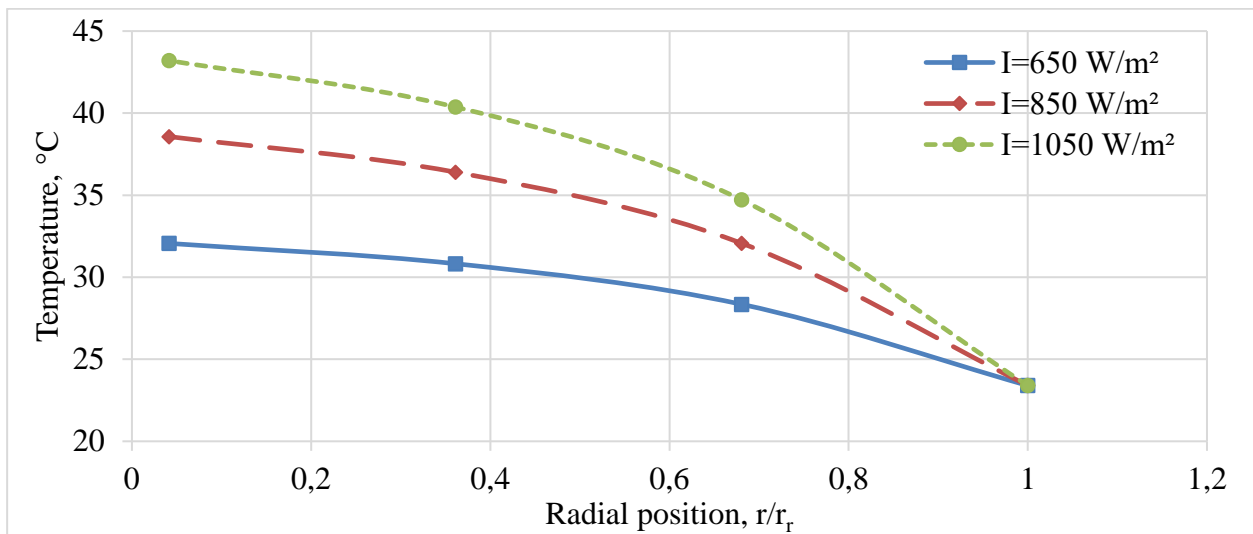


Fig. 4.1. Temperature profile inside the collector at different solar radiation

Fig. 4.2 shows the variation of the temperature profile at the different mass flow rate with the constant solar radiation of 850 W/m². The outlet temperature of the collector, T_2 , is reverse proportional to the mass flow rate. On the other hands, the mass flow rate is directly proportional to the produced power according to Eq. 3.45. Thus, the optimization value of mass flow is investigated for generating more produced power.

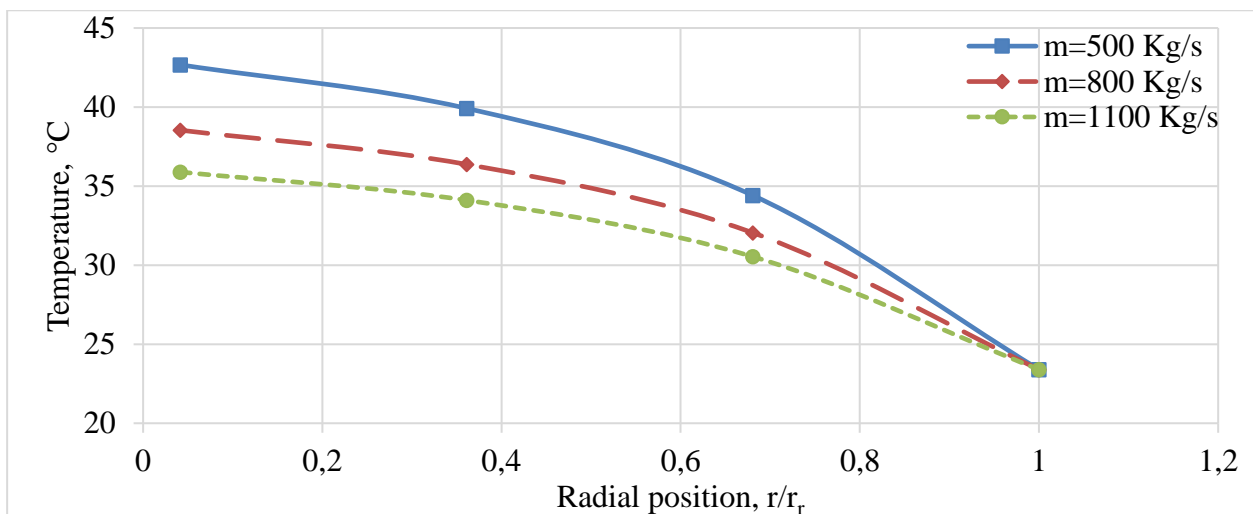


Fig. 4.2. Temperature profile inside the collector at different mass flow rate

4.1.2. The effect of mass flow rate

The influence of the mass flow and solar radiation on the output power is shown in Fig. 4.3. The behaviour of the curves is in good agreement with the result that was achieved by Koonsrisuk and Chitsomboon, (2013). The maximum power output is a function of the mass flow and solar radiation. So, the recommendation for optimum operation of the SCPP follows up the line of the maximum power, which is shown in Fig. 4.3. This can be applied by changing the turbine speed or changing the blade setting angle.

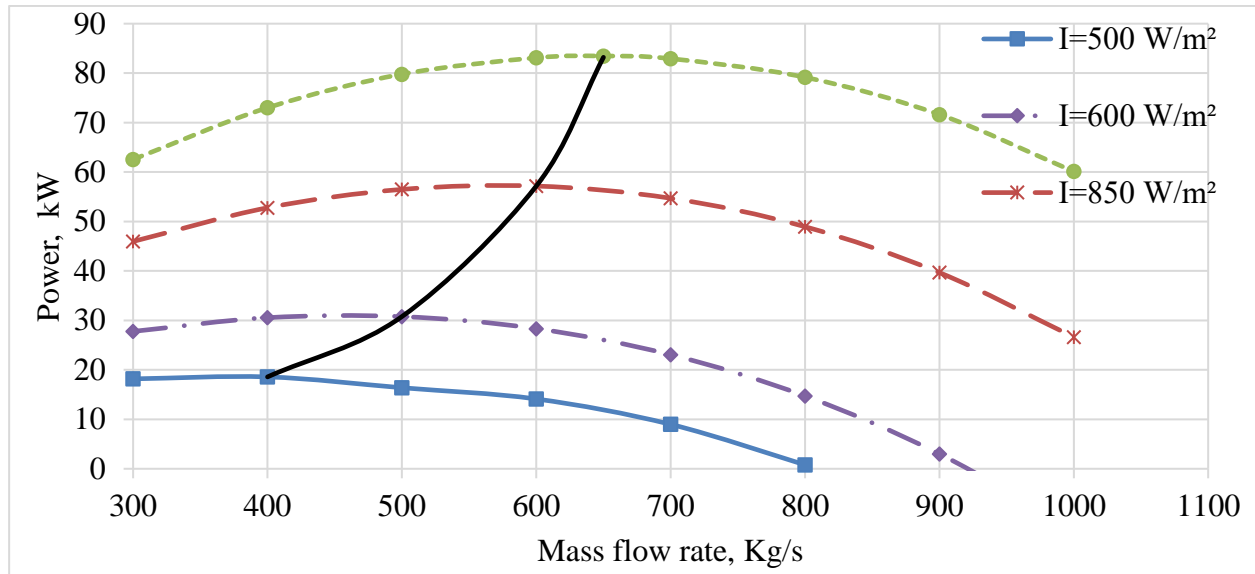


Fig. 4.3. Influence of the mass flow and solar radiation on the outlet power

The variation of the diffuser velocity speed-up ratio, γ , with mass flow and solar radiation is shown in Fig. 4.4. We can clearly notice that the range value of γ is insignificant variation from 1.6423 to 1.639 about 0.2012%. And the above-calculated value of γ is approximately equal to the average range, as shown in Fig. 4.4. As a consequence of this discussion, I will take γ equal 1.6403a new design.

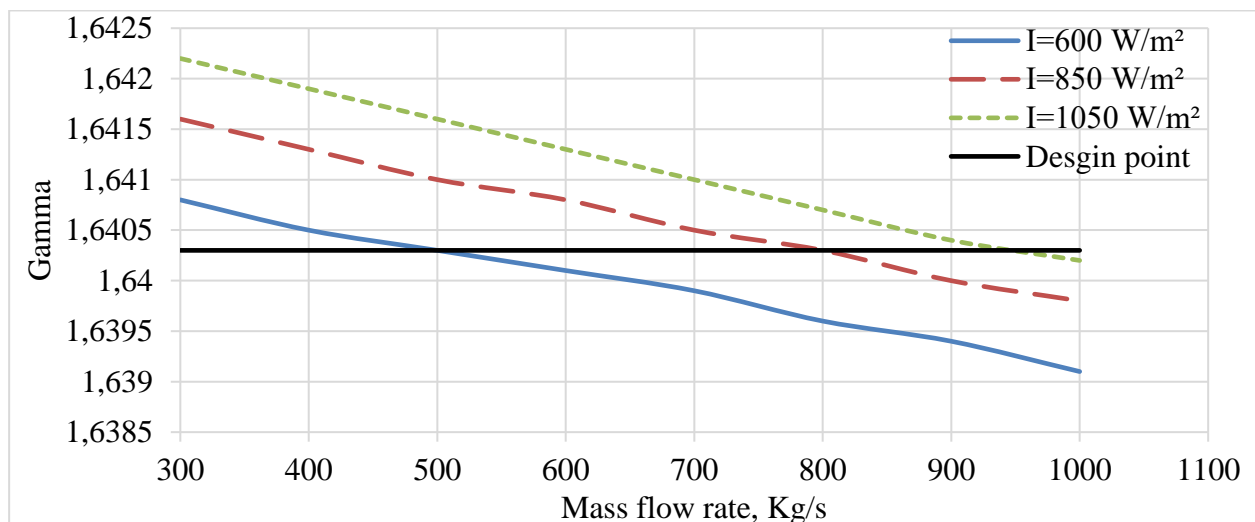


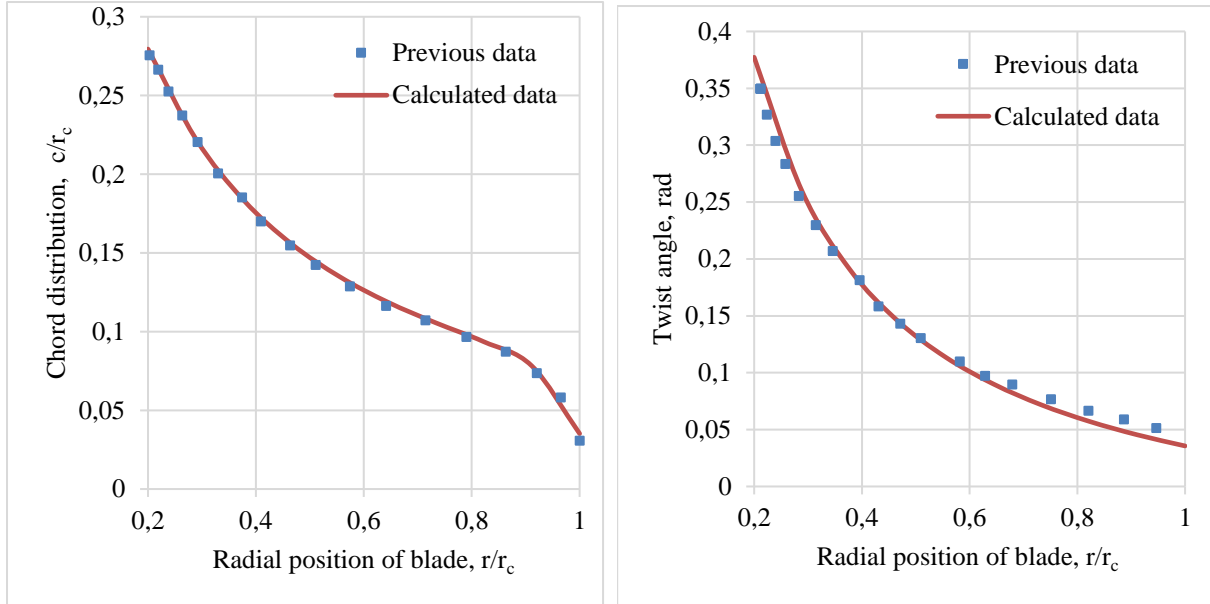
Fig. 4.4. Variation of the diffuser velocity speed-up ratio with mass flow and solar radiation

4.2. The methodology of turbine design working on SCPP

Based on the aerodynamic analysis and the optimization of a shrouded turbine blade, I implemented it within the MATLAB code to calculate the chord distribution and twist angle of the

4. Results

blade. This code also applies tip loss correction as from of Shen *et al.*, (2005). To validate the code, the comparison of its result and result of Vaz and Wood, (2016) that I have done using the same input data that is shown in reference(Vaz and Wood, 2016), as shown in Fig. 4.5. Vas and Wood compared data from their optimization and National Aerospace Laboratory (NAL) design to show the improvements that were achieved by using their optimization.

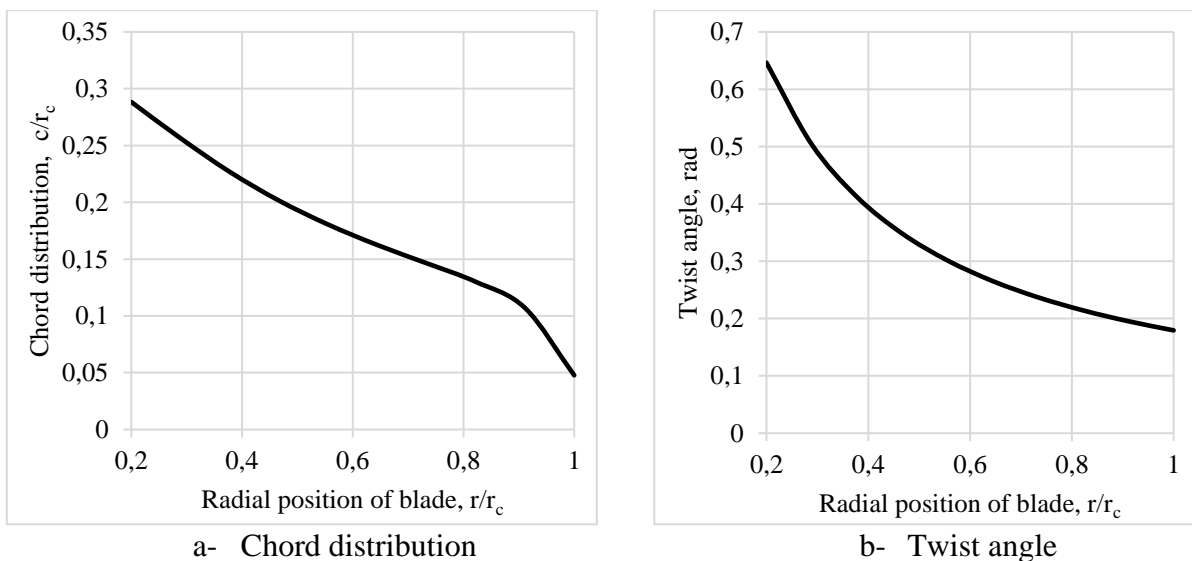


a- Chord distribution

b- Twist angle

Fig. 4.5. Comparison of calculated data and data of (Vaz and Wood, 2016)

Finally, the chord distribution and twist angle of optimization blade shape of SCPF is shown in Fig. 4.6 using the design parameter in Table 4.3. The main aim of the new design is achieving more power than the previous turbine. An integration of Eq. 3.12 using the trapezoidal method calculate the power coefficient of the new design is 0.45, and then calculate the theoretical output power is 55.752 kW. The increase in the output power is 15.19% compared to the original design. I have been created the 3D of the design blade using SOLIDWORK that shown in Fig. 4.7.



a- Chord distribution

b- Twist angle

Fig. 4.6. The Designed blade shapes

Table 4.3. design parameter using by optimization code

Turbine radius, R_t	5 m
Hud radius , R_h	1 m
Number of blades , B	4
Blade airfoil	FX W-151-A
Turbine speed , Ω	100 rpm

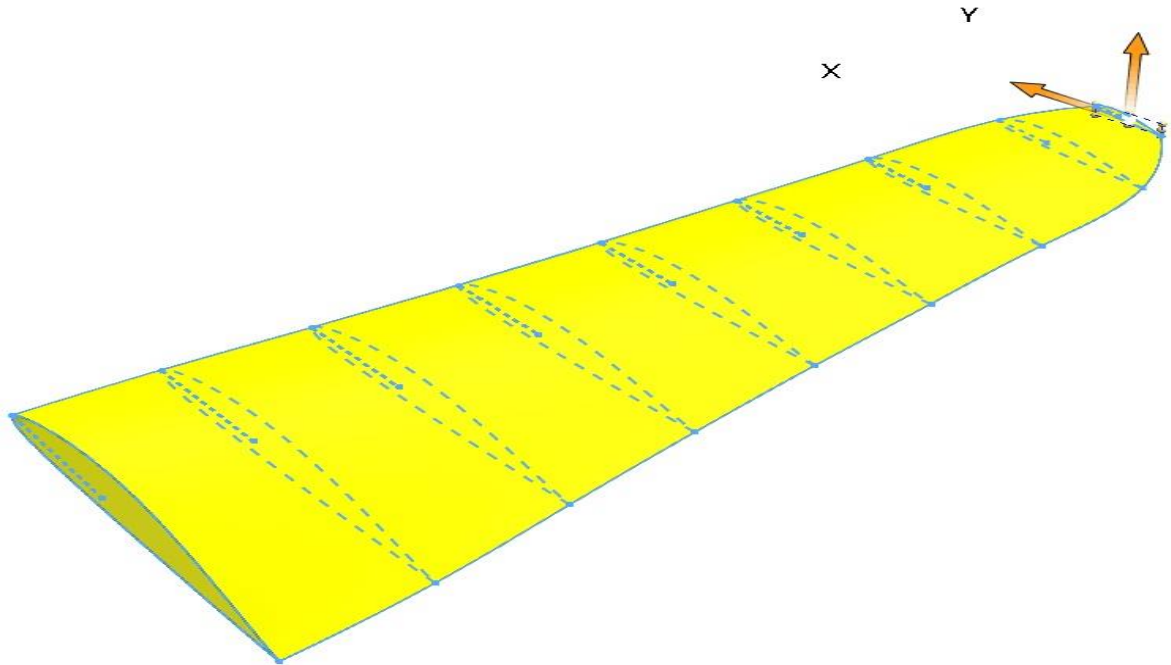


Fig. 4.7. 3D of designed blade for SCPP

4.3. Simulation SCPP with radiation models and turbine

Computational fluid dynamic (CFD) is a powerful tool to analyse a physical system. As mentioned in the literature review section 2.2, many searchers use the capabilities of the CFD technique to analyse complicated physics systems. To achieve that purpose, authors use ANSYS CFX software for solving the governing equation with the k-omega turbulence model. I made the 3D model of the whole SCPP with turbine and radiation model to study velocity and temperature distribution inside collectors.

The objective of this model is to accurately analyse the SCPP system by using CFD simulation model, my new approach depends on a few assumptions and provides more detailed descriptions of pressure and flow field. A 3D approach for SCPP prototype is carried out by using ANSYS CFX v18 with axial vertical flow turbine. The turbine is designed of using free vortex and the matrix throughflow method.

To validate the CFD model, calculated results were compared with the experimental results of the prototype from Manzanares, Spain. The measured data on September 2nd, 1982 are adopted from Reference (Haaf, 1984). The plant dimensions are given in Table 4.4. The comparisons between the calculation results and the experimental values are presented in Table 4.5. There is good agreement between measurement and calculation results, which are acceptable value.

4. Results

Table 4.4. Geometrical dimensions of the pilot plant in Manzanares, Spain

Mean roof radius	122 m
Average roof height	1.85 m
Tower height	194.6 m
Tower radius	5.08 m

Table 4.5. Comparison between measured data and theoretical model results

	Measured	Calculated	Percentage
Different temperature at the collector, °C	17.1	14.25	-16.6 %
Upwind velocity, m/s	9.045	9.11784	0.81 %
Output power, kW	36	36.1552	0.41%

The air velocity is calculated at different locations in the whole domain of the SSCP unit. The upstream and downstream lines of the air velocity are calculated. As shown Fig. 4.8, the maximum velocity according at near close to the chimney entering, and uniform airflow in the collector region. The range of the velocity in the chimney is approximately 4 times the range of velocity in the collector. To capture more output power, the turbine should be located at high air velocity, which is achieved in near enter of the chimney.

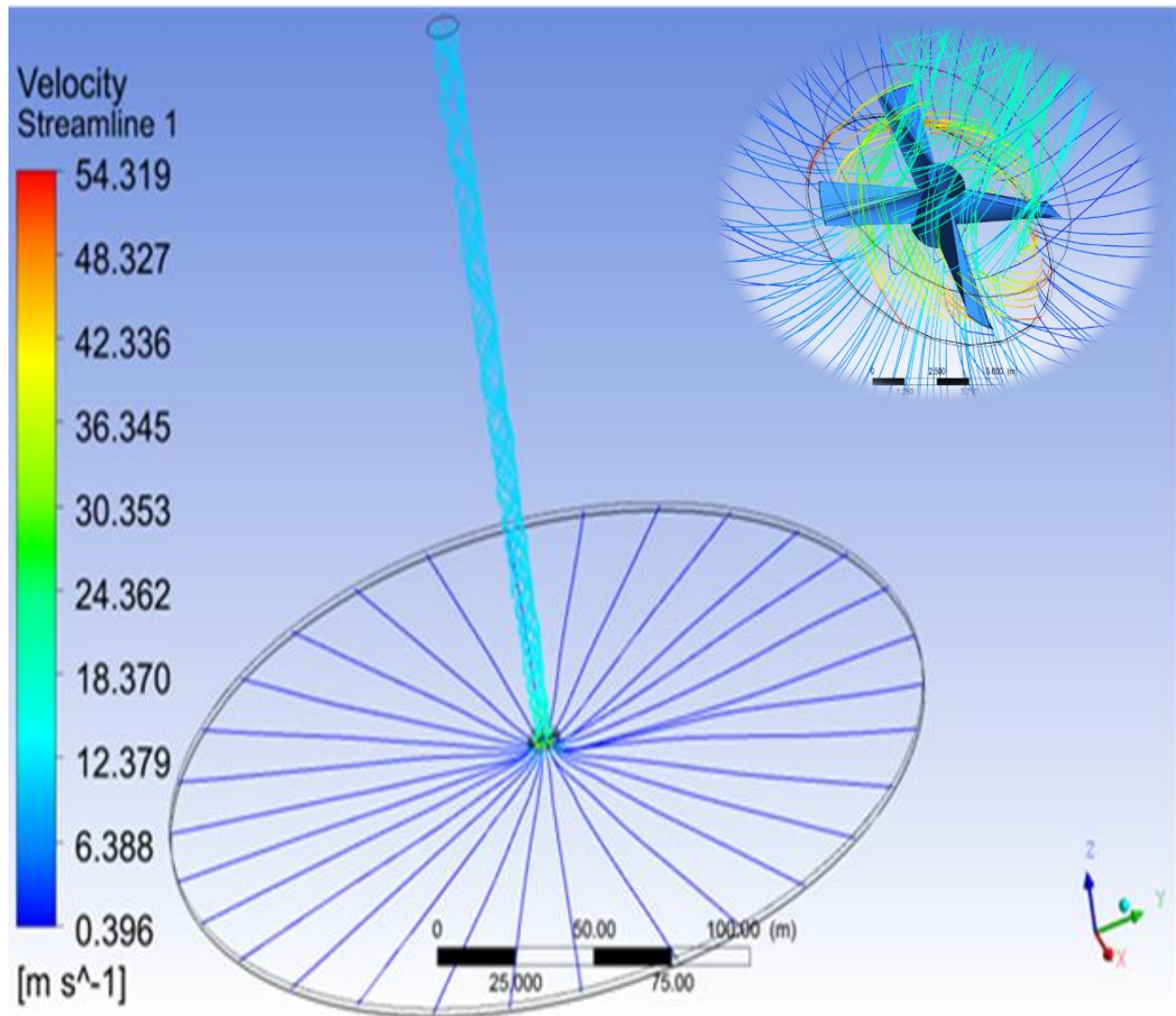


Fig. 4.8. Streamline of air in SSCP model

4. Results

Fig. 4.9 illustrates contours of the pressure distribution at different zones of the chimney in a vertical intersection. The pressure around turbine has significant influence of the SCP performance. Fig. 4.9 shows that the pressure increases gradually as the air is flowing inside the chimney. It indicates also that the minimum static pressure is reached near the chimney base at the exit of the turbine due to extract the energy from the flow by the turbine.

The blade of an axial turbine flow depends on the aerofoil theory. The blade consists of the aerofoils that interact with the hot air and convert the power in the air to mechanical power. The pressure distribution around the aerofoil surface controls in the lifting properties of the aerofoil. Fig. 4.10 show the pressure distribution at different lengths of the blade. As shown, the tip section of the blade has enough large pressure difference between the upper and lower surface. On other hands, the hub section has less pressure difference between its surfaces. Consequently, static pressure increases from root to tip. The degree of reaction control of the pressure distribution, which increases from root to tip according to free vortex assumption. However, the power production is constant a long of the blade. The energy production and degree of reaction is an agreement of the free vortex principle.

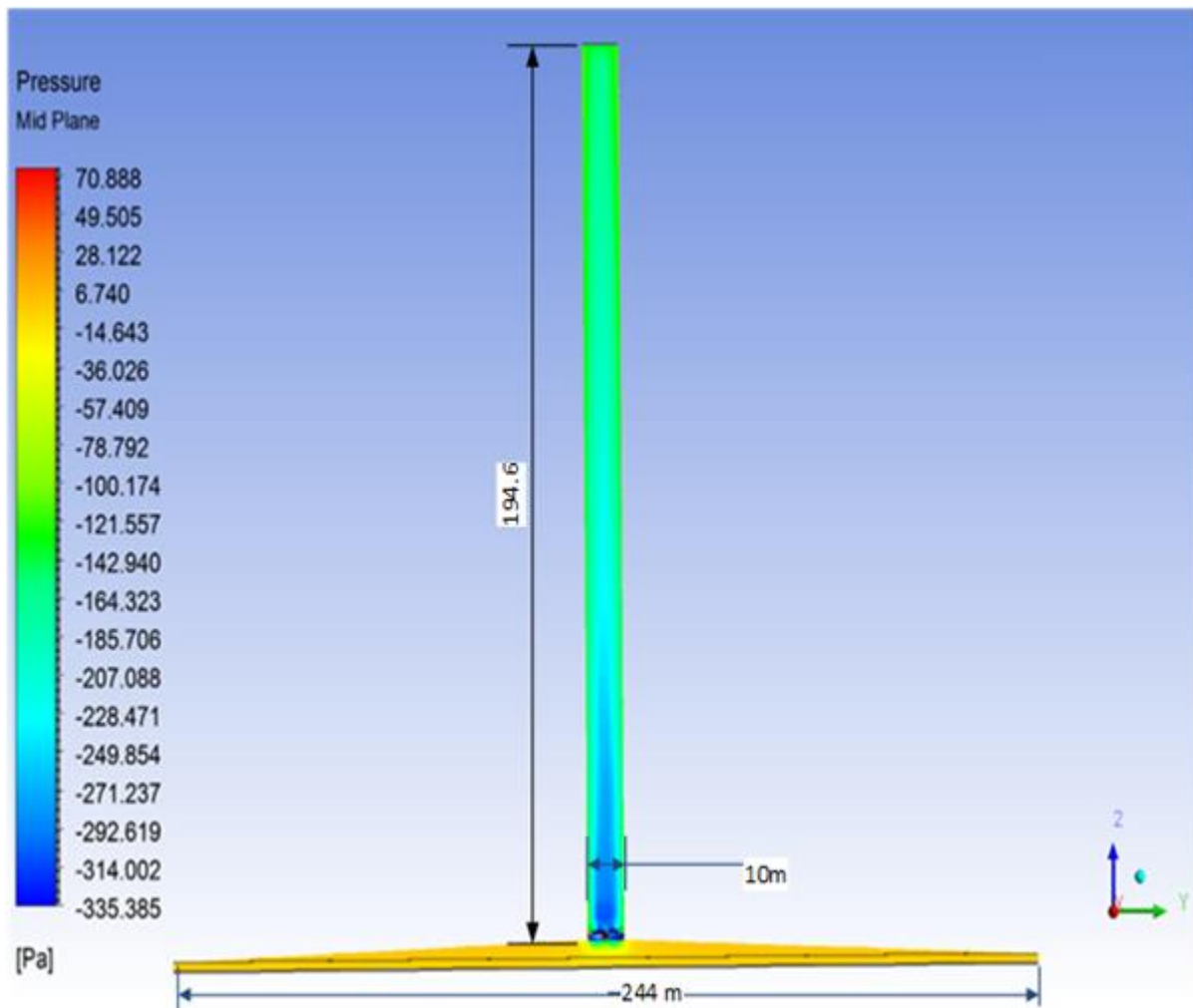


Fig. 4.9. Contours of static pressure at different zones of the chimney

4. Results

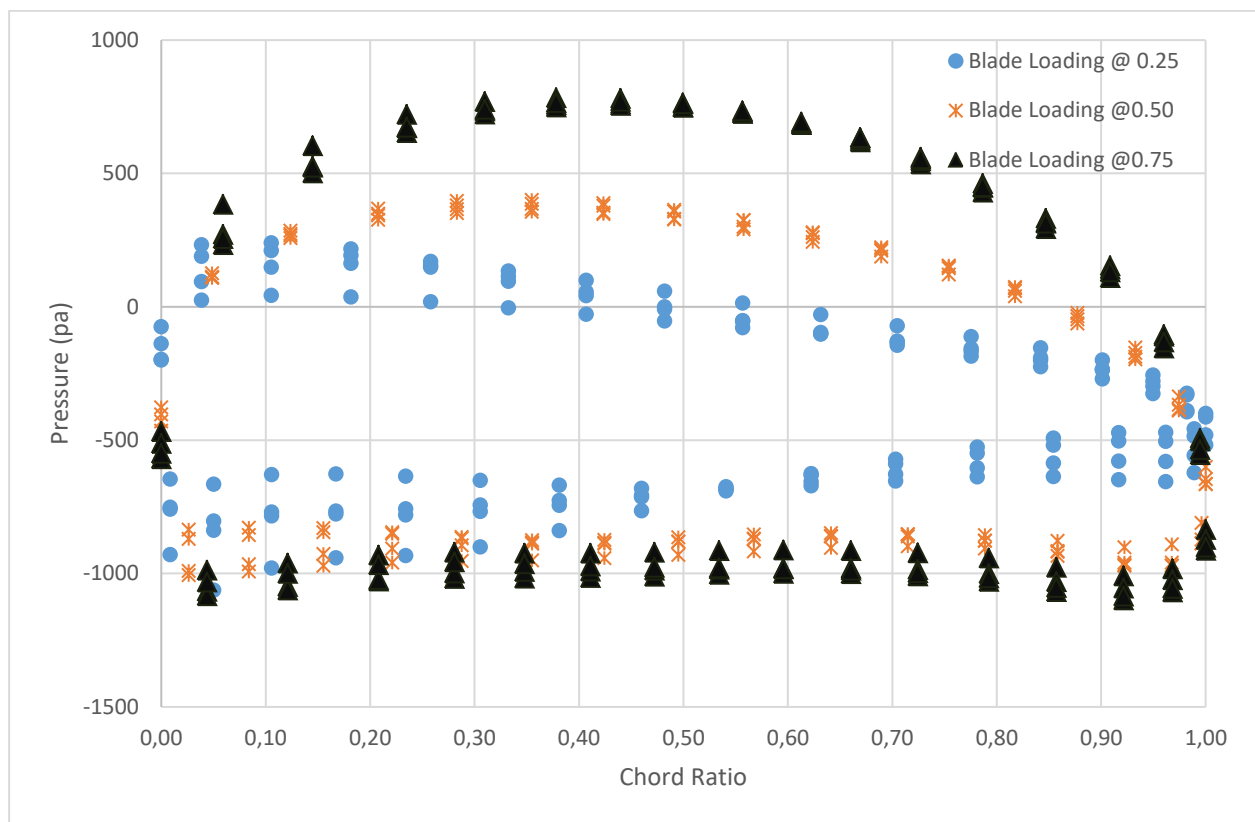


Fig. 4.10. pressure distribution at different length of the blade

4.4. The influence of the solar collector shape

The solar chimney power plant system is proposed to produce electric power on a large-scale, utilizes solar heating and chimney effect for increasing kinetic energy of the ambient air that drives wind turbines to produce electric power. High insolation and over 90 % available desert lands are two main conditions that motivated the development of thermal solar power plants as generally, and solar chimney power plant especially for electrical energy productions (Mostafa, Sedrak and Dayem, 2011). Thus, thermal solar electricity project is a perfect solution to utilize the Aswan weather condition, that motivated Science and Technology Development Fund (STDF) of Egypt and Federal Ministry of Education and Research (BMBF) of Germany funded prototype of SCPP in Aswan, Egypt as a joint project. The experimental work is carried out on the Aswan prototype that is A small-scale solar chimney type. Table 4.6 shows the dimension of this prototype.

Table 4.6. Dimension of Aswan solar chimney prototype

Location	Dimension	Description
Diameter of chimney	1m	Steel tube of 0.8 mm thickness
Height of chimney	20 m	
Solar collector	28.5 m side length	Square shape collector
The height of inlet collector	1.25m	
The height of outlet collector	1.5m	

The collector has two common shapes: circular collector and square shaped collector, for studying the more efficient shape, we made the CFD model for both shapes. Table 4.7 shows the calculated results of both shapes of the collector. The geometric calculation shows the square shape collector increases the inlet area by 11.4 % than the circular collector. The airflow isn't a uniform

distribution on the inlet area because of low inlet air velocity, the reverse airflow takes a place on the geometric inlet area and the effective inlet area present the actual part of a geometric inlet area that allows the airflow inside the collector. The square collector increases the effective inlet area by approximately 30% at the same inlet height, the mass flow rate of square shape is consequently increased by 4.3 %. However, solar radiation exposed to the same surface area in both cases, but the circular shape achieves 0.683 °C higher than the square shape collector of the average exit temperature. Due to the increase in the mass flow rate, the output power that produces increases by 7.6 % based on the square calculation results.

Table 4.7. CFD results of circular and square collectors

	Circular collector	Square collector	Percentage
Geometric inlet area, m ²	151.55	171	11.4%
Effective inlet area, m ²	101.026	144.3	30%
Mass flow rate, Kg/s	13.4487	14.0507	4.3%
Outlet temperature of collector, °C	45.124	44.441	-1.5%
Output power, W	329.237	356.151	7.6%

4.4.1. The square shape collector

Using a velocity vector tool in ANSYS CFX-Post, we can get more analysis of the air velocity inside the collector. Fig. 4.11 shows the velocity vector field at height 0.65 m from the ground (approximately mid-span) and radial direction of the velocity vector field of the square collector. Fig. 4.11-a shows the shortest radial direction from the mid-span of the square side to the centre of the collector and Fig. 4.11-b shows the longest radial direction from the corner of the square side to the centre of the collector. The differences between Fig. 4.11-a and Fig. 4.11-b results from the different length of the airflow path.

The velocity distribution has a considerable effect in creating temperature distribution inside the collector. Fig. 4.12 shows the temperature contour at approximately mid-span from the ground (the same plane of the velocity vector) and the radial direction of the temperature contour of the square collector.

4.4.2. The circular shape collector

For demonstrating the difference of the performance between the circular shape and square shape collectors, we follow the similar pattern of the calculated result for the circular shape collector. Fig. 4.13 shows the velocity vector field at height 0.65 m from the ground (approximately mid-span) and radial direction of the velocity vector field of the circular collector. The airflow suffers from a high turbulence and some reverse flow at the inlet as shown in Fig. 4.13-b and Fig. 4.13-a, both of these paths have the same length. However, the longest paths from corners to the centre of the collector has more smooth airflow at the inlet area, as shown in Fig. 4.11-a. Consequently, the square shape collector achieved a larger mass flow rate of air.

Fig. 4.14 shows the radial direction of the temperature contour of the circular collector and the temperature contour at approximately mid-span from the ground (the same plane of the velocity vector). The temperature distribution inside the circular shape collector is exceedingly regularly, as shown in Fig. 4.14-a. The turbulent flow assists to increase the heat transfer by an increasing the length of flow streamline and mixing processes of a laminate of the fluid. However, the square

4. Results

shape collector has a more turbulent flow pattern, as shown in Fig. 4.12, it achieves less the average exit temperature of the collector by -1.6 % than the circular collector, because of the higher mass flow rate.

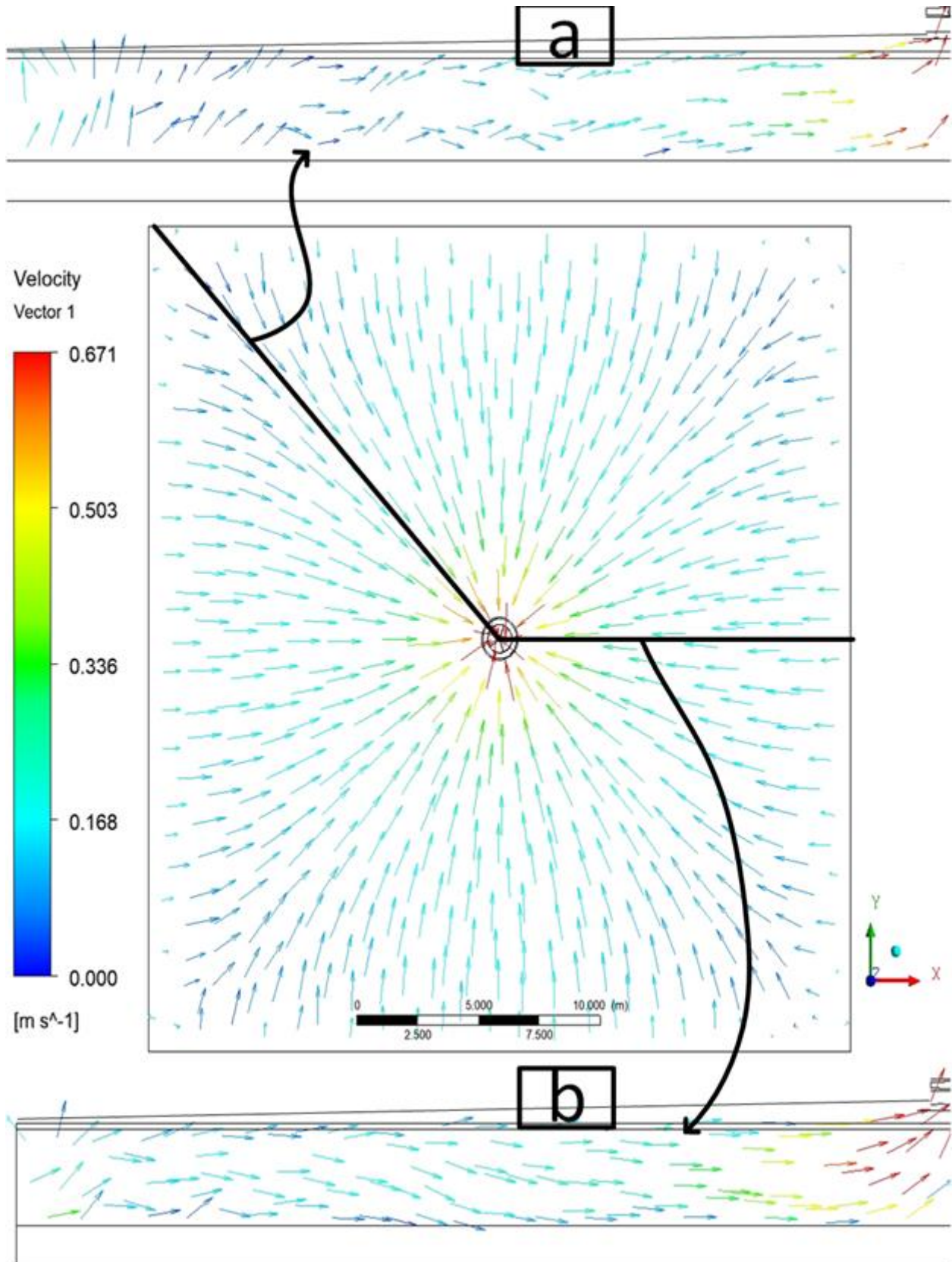


Fig. 4.11. Velocity vector inside the square shape collector

4. Results

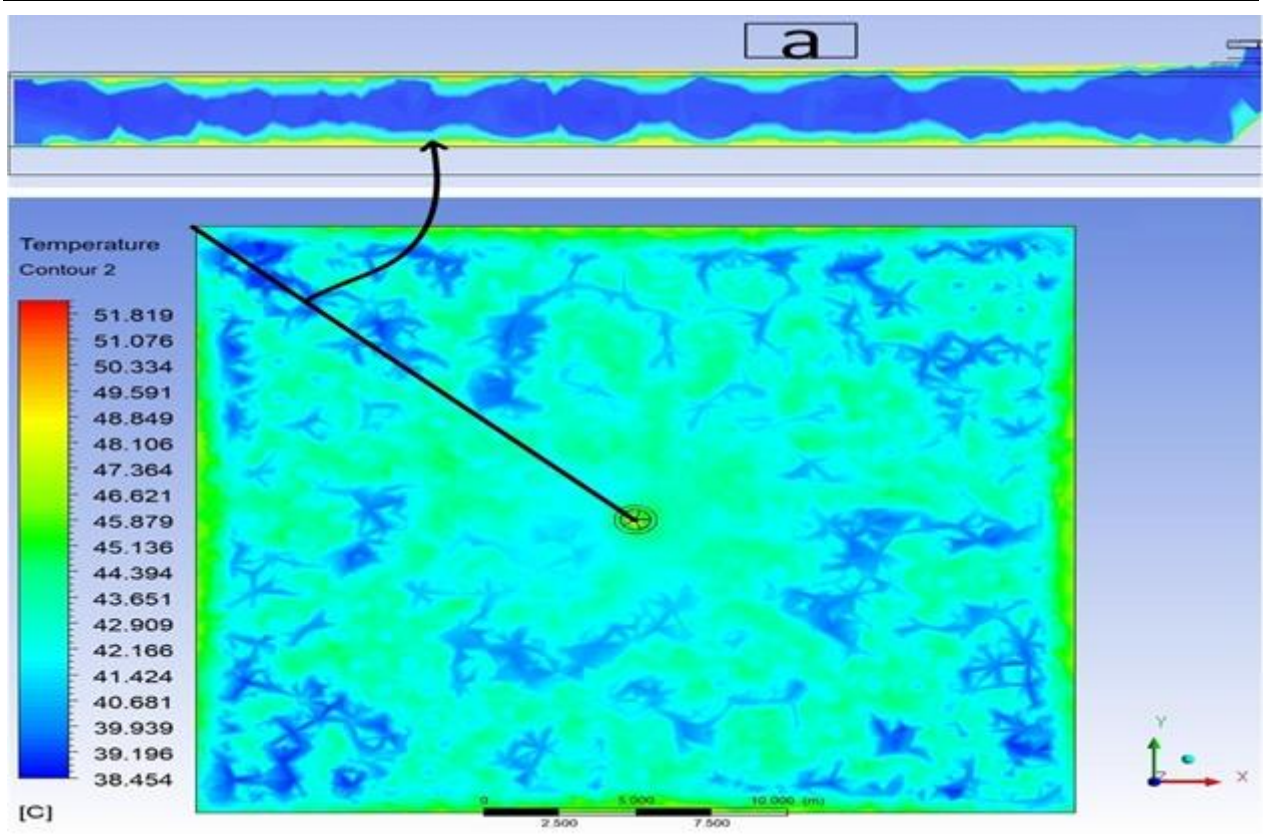


Fig. 4.12. Temperature distribution of the square collector

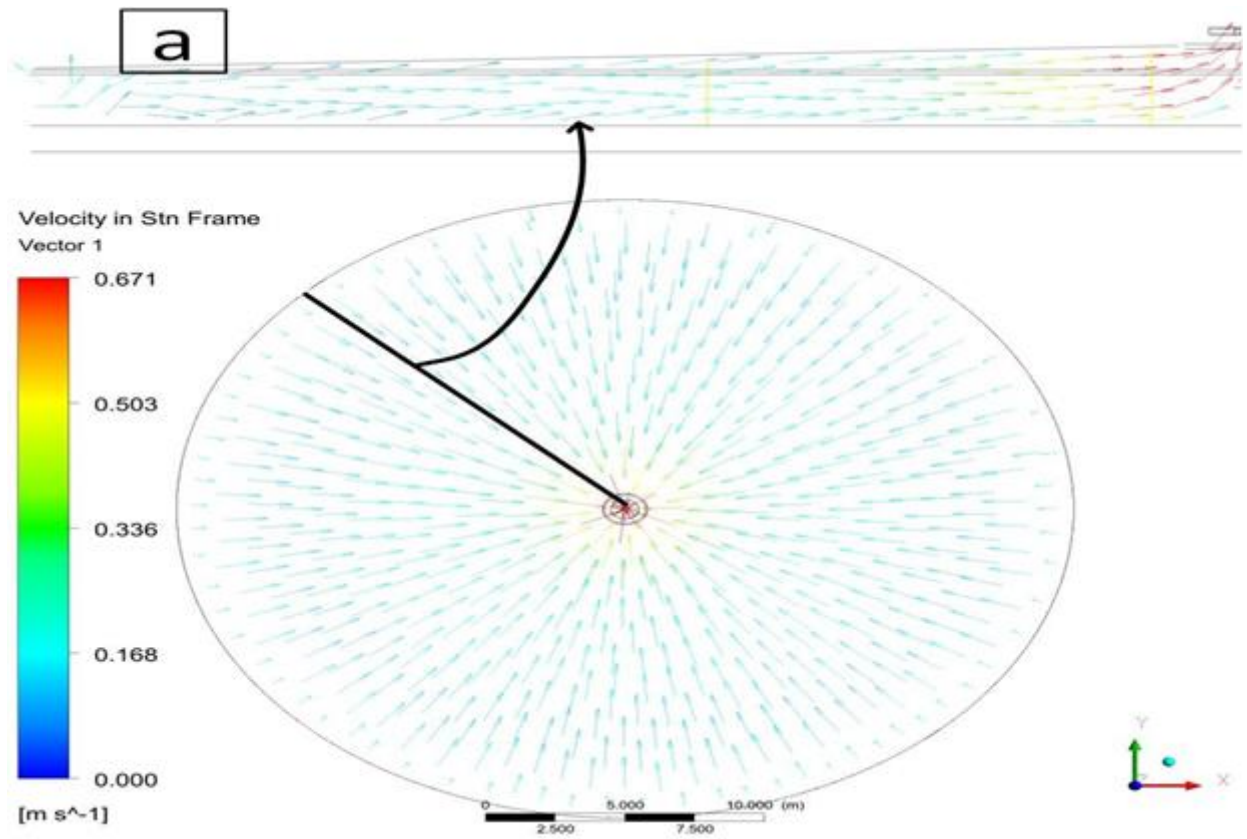


Fig. 4.13. Velocity vector of the circular shape collector

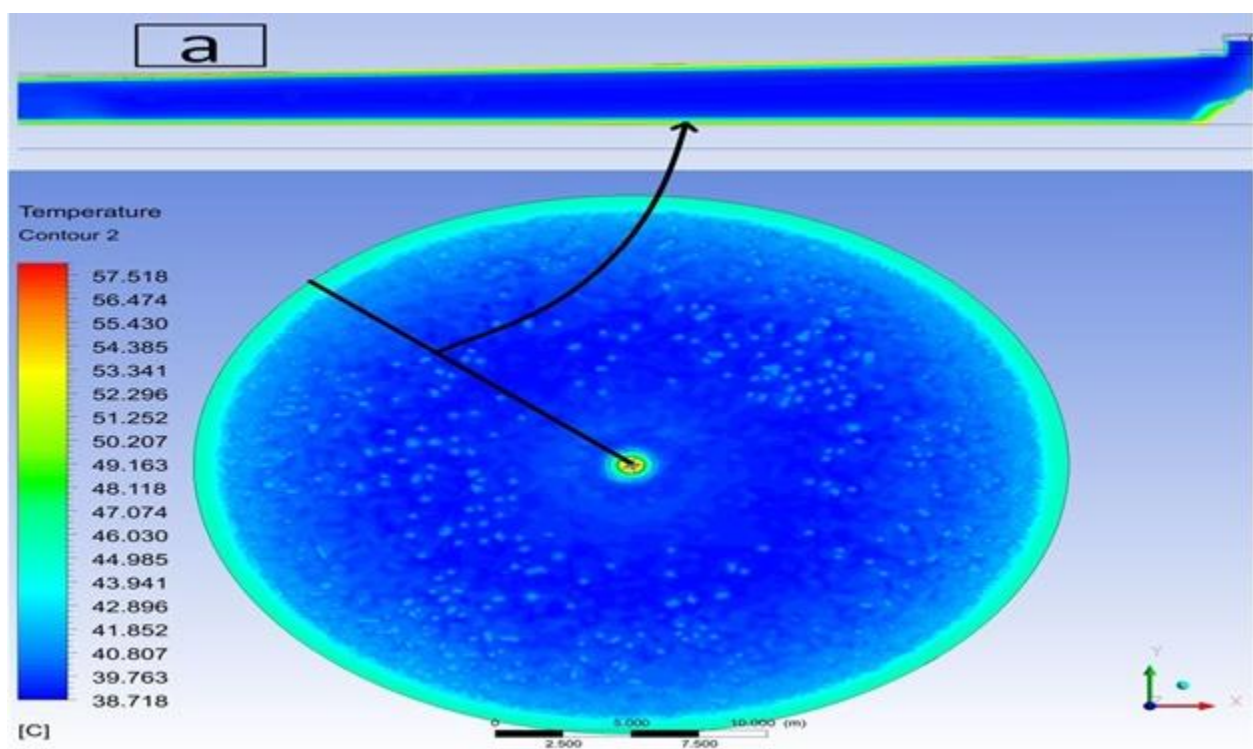


Fig. 4.14. Temperature distribution of the circular shape collector

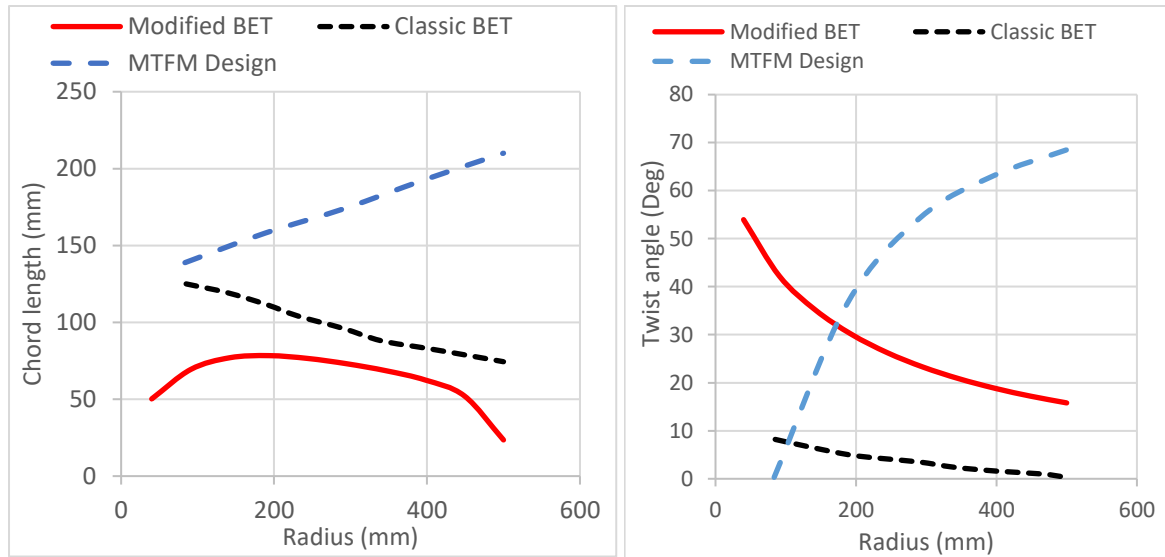
4.5. Comparing of the different theories of the turbine design

To raise its reliability and expansibility, efficient design of the solar chimney system components is an utmost necessity. A turbine is a key component because it captures the mechanical energy from airflow. In a recent study, we presented and compare three different designs of the solar chimney turbine for a substantiation the more suitable theory to design solar chimney turbines. We used CFD simulation models to study three different designs of a solar chimney turbine as

- A. MTFM design: this design is carried out using Matrix throughflow method. The Vista AFD under ANSYS Workbench v 18 is used to design the turbine of the SCPP by A. Elmagid and Keppler, (2017);
- B. Classic BET design: this design is carried out by solving the Blade Element Theory (BET) equation, which usually used to design the horizontal axis wind turbine that is used in Aswan prototype;
- C. My design blade: I designed a blade according to BET that considering surrounding duct , this design carried out by solving modification of BET theory to make it considering the surrounding duct effect by A. Elmagid, Keppler and Molnar, (2020);

As a pre-step of the grid generation, 3-D geometry of the solar chimney prototype is drawn using SOLIDWORKS software according to a small-scale solar chimney prototype, which was implemented in Aswan, Egypt, that dimensions are shown in Table 4.6. The turbine blade shape was obtained by using the Loft command within SOLIDWORKS software, which created a 3D solid or surface by lofting a series of cross-sections. The cross-sections are defined as airfoil shape according to Fig. 4.15-a and twist to the twist angle in Fig. 4.15-b. Then, ANSYS Workbench Meshing software was used for creating the CFX grid for different zones of the prototype, except for the turbine domain in which we used TurboGrid program, Fig. 4.16 shows 3D turbine domain of three different design blade.

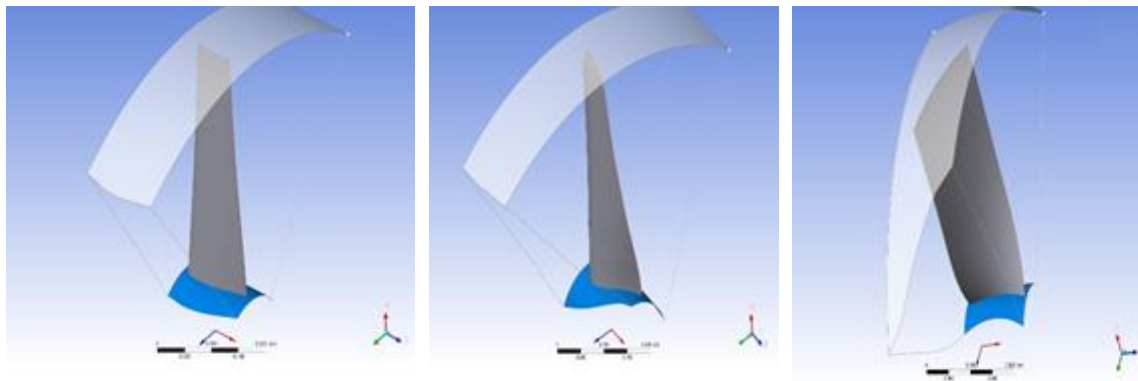
4. Results



a. Chord Distribution

b. Twist angle

Fig. 4.15. Comparison of blade parameters for different designs



a. Classic BET blade

b. My design blades

c. MTFM blade

Fig. 4.16. TurboGrid element for various designs

Table 4.8 shows the location and the value of the used boundary conditions in Aswan SCPP model. The height of the chimney is considered by evaluating the change of the atmospheric pressure with height as it is well-known that the flow inside the chimney follows up a dry adiabatic lapse rate, I used the two-opening surface with differences pressure to simulate a dry adiabatic laps rate effect. The boundary condition is selected to be in the range of the previous experimental studies, especially, Aswan SCPP prototype. Direct radiation and rotational of the turbine are taken from experimental data because the data continuously changes with time. The rotational speed of the turbine is an important parameter that affects the performance of the SCPP, it also indicates the electrical load on the turbine. The surface of the ground which is in contact with air exposed to solar radiation is less than the outer cover surface by glass transmission. Fig. 4.17 showed many points of the experimental data which have been achieved by using the CFD model, additionally, the values of the theoretical results are part of the range of the experimental record data of Aswan prototype.

Table 4.8. Boundary condition of the CFD models

Location	Boundary type	Value
Inlet of collector	Opening	1 atm
Outlet of chimney	Opening	0.9967 atm (adiabatic lapse rate)
Turbine domain	Rotational farm	Rotation speed from experimental
Outer surface of glass cover	Wall, Radiation source	Direct radiation from experimental
surface between collector air and ground	Interface surface, Radiation source	Direct radiation from experimental x transmissivity of glass

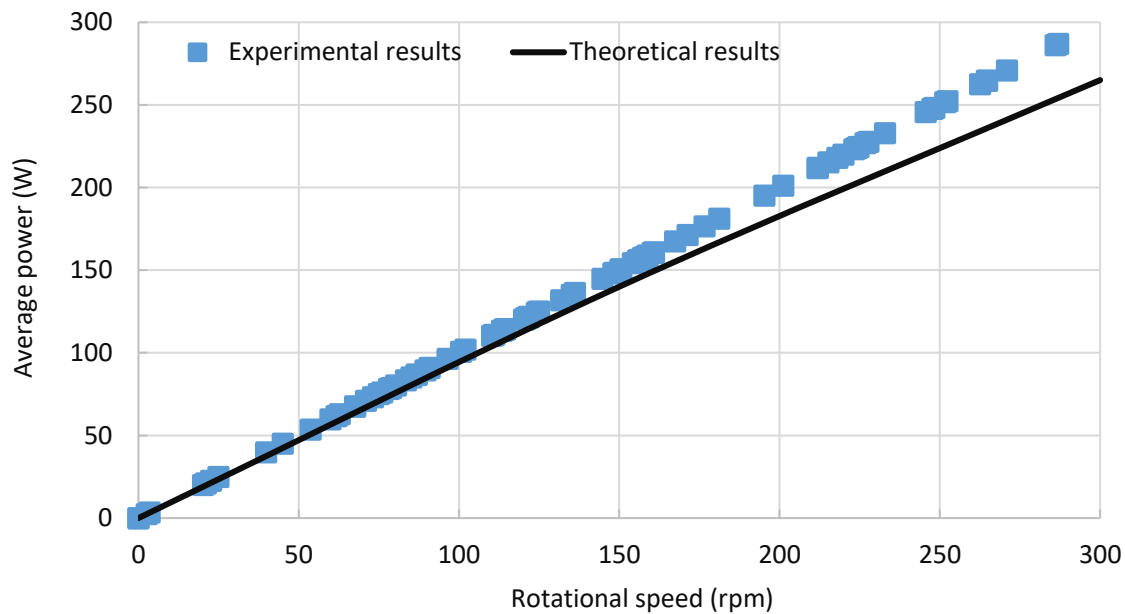


Fig. 4.17. Validation of the theoretical results

To analyse the performance of a solar chimney turbine, the mechanical output power of the different turbines. My designs and Classic BET have the same trend of curve behaviour because they obey to blade element theory (BET). However, my design gives higher power than Classic BET Design at the same rotational speed because it considers the surrounding duct and tip correction factor. MTFM design provides the highest output power at the low rotational speed, but its productivity is the lowest at the high speed. The high rotational speed is more preferred in electric power generation.

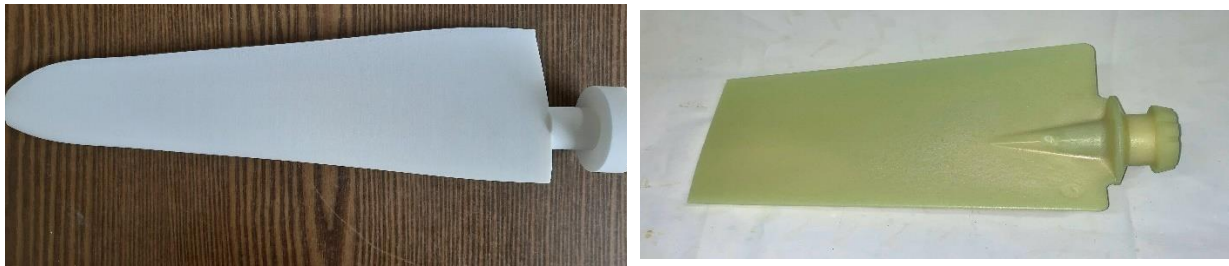
4.6. Wind tunnel measurements

A three-dimensional analytical model to compute the deflection and stresses in the rotor blades is important to show the ability for manufacturing my designed blade. I used a finite element simulation model within the ANSYS Mechanical model. The results showed mapping of stress and strain on a rotor blade, which provides vital information concerning the turbine design and

4. Results

leads to the detection of the blade critical section. Most of the structural failures of turbine blades occur in the blade root section.

Wind tunnel testing provides an accurate performance of the physics system, but they do it under the very strict operating conditions to ensure the stability of the system. This condition and stability assist in the systems investigation and going deeply in some point. We tested two turbines; the industrial fan rotor that was manufactured by MULTI WING and model of MWCZF2505041, and the second one is the turbine designed according to our calculation in section 3.5, which was manufactured by 3D printing technology. The geometry of the experimented elements are shown in Fig. 4.18 as; Fig. 4.18-a show the designed blade and Fig. 4.18-b show the industrial one.



a. Designed blade

b. Industrial blade

Fig. 4.18. Geometry of the experimented blade

The electrical load of the turbine is the generator, we can change the excitation to change the torque against turbine torque. Fig. 4.19 shows the different excitation of the generator for the industrial turbine. The change of the excitation has a minor effect on the rotational speed of the turbine because the turbine works at the near its designed tip speed ratio. The generator construction puts its limit on the excitation power.

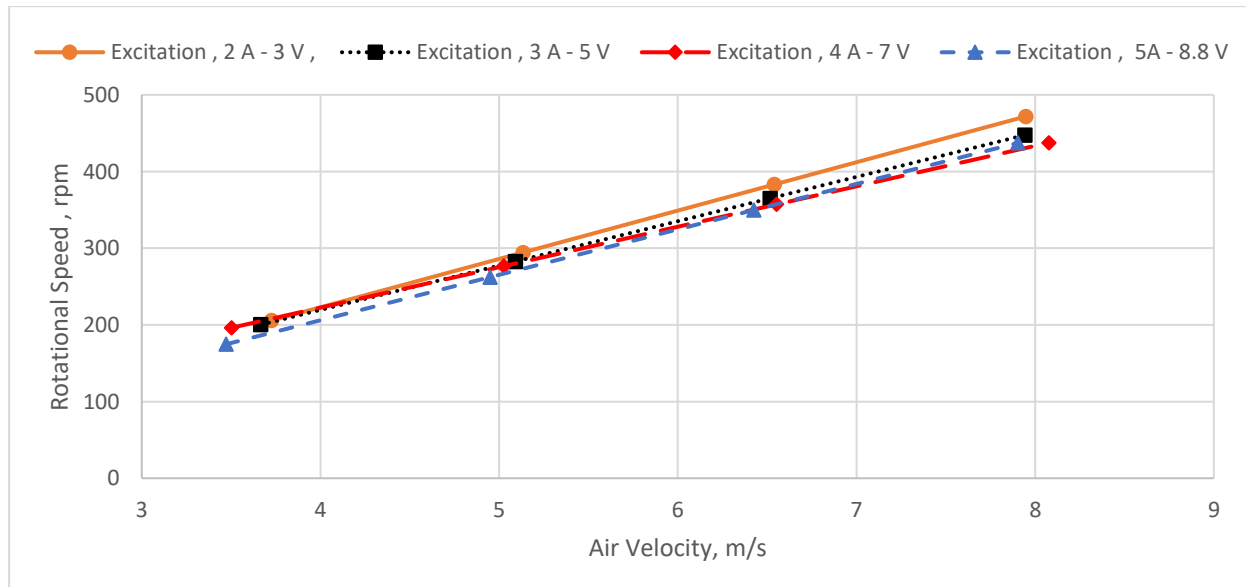


Fig. 4.19. The rotational speed of the industrial turbine at the different excitation power

The generator shows the same behaviour on the designed turbine, as shows in Fig. 4.20. The turbine has the higher rotational speed on the 8 m/s as design point while I calculated my design at 3.5 Tip speed ratio. The designed turbine achieved higher rotational speed than the industrial

4. Results

one at low air velocity (5-8 m/s), that give the designed turbine advantages to work at this range of air velocity.

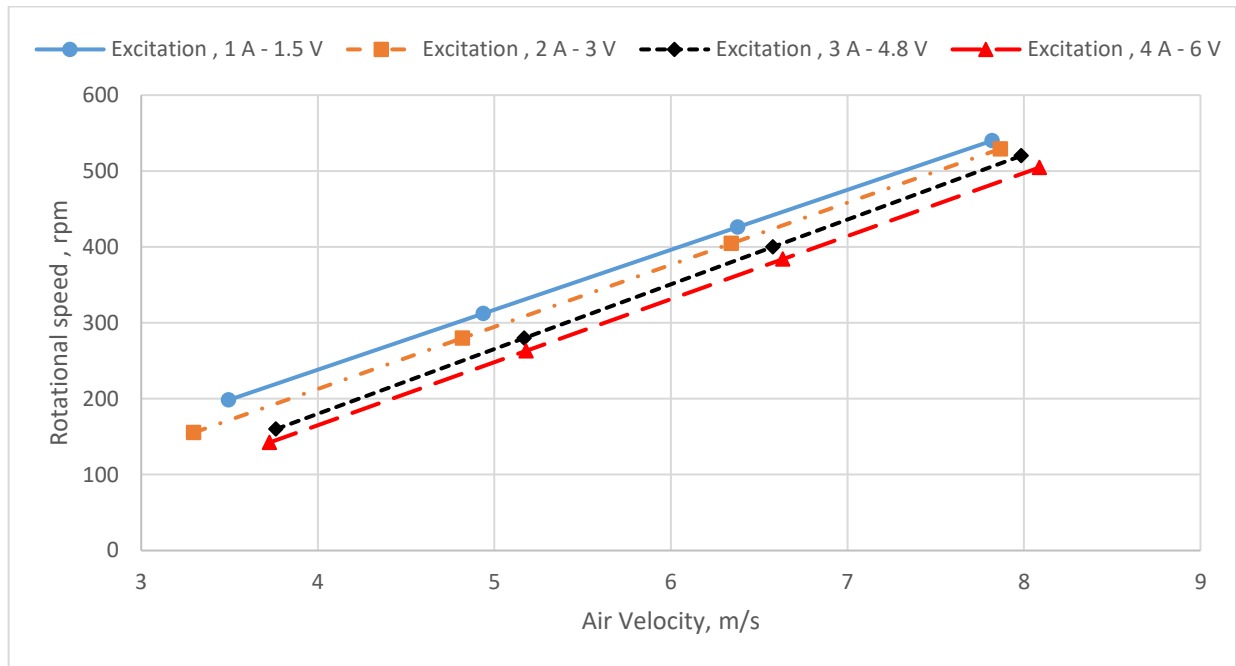


Fig. 4.20. the rotational speed of the designed turbine at the different excitation power

Fig. 4.21 shows the pressure drop by the turbine, the turbine pressure drop has a dominant influence on performing the SCPP, indicates what energy is absorbed by the turbine at excitation of generator by 2 A - 3 V. The pressure drops increases with increasing the inlet velocity because more energy is available for the turbine by the airflow. Generally, the pressure drop of the designed turbine is higher than the industrial turbine by 1.5 times approximately at all points. The designed turbine achieved 65.08 Pa of the pressure drop, while the industrial turbine achieved 43.93 Pa at the inlet velocity of 15 m/s.

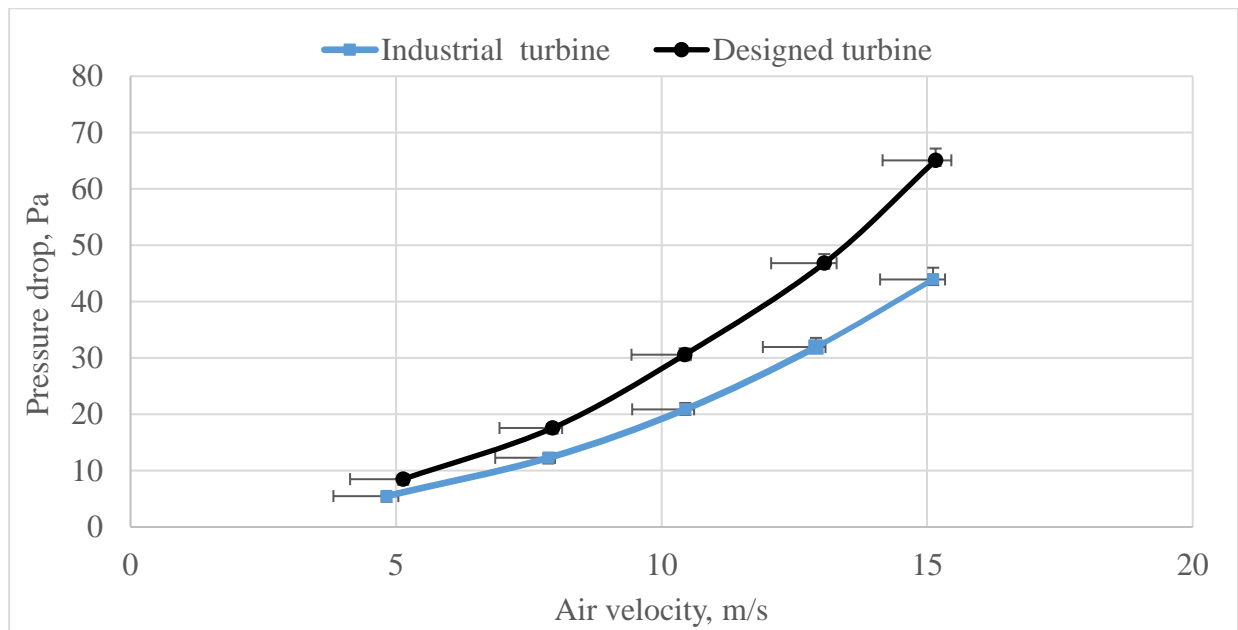


Fig. 4.21. Pressure drop around the turbine

4. Results

Output power is the major purpose of the system, the turbine produces power that is proportional to inlet fluid power. In the case of the shrouded turbine, fluid power is a combination of the kinetic energy of airflow and pressure energy. Fig. 4.22 shows the power of the turbine according to the inlet velocity of the airflow at excitation of generator by 2 A - 3 V. The designed turbine achieved more power than the industrial one. The designed turbine comprises 4 blades, and the industrial turbine comprises 3 blades, the designed turbine produces 135.16 W per blade, and the industrial turbine provides 121.69 W per blade at 15 m/s inlet velocity. Thus, the designed turbine produces 12.55% higher than the industrial one as average increase on all points.

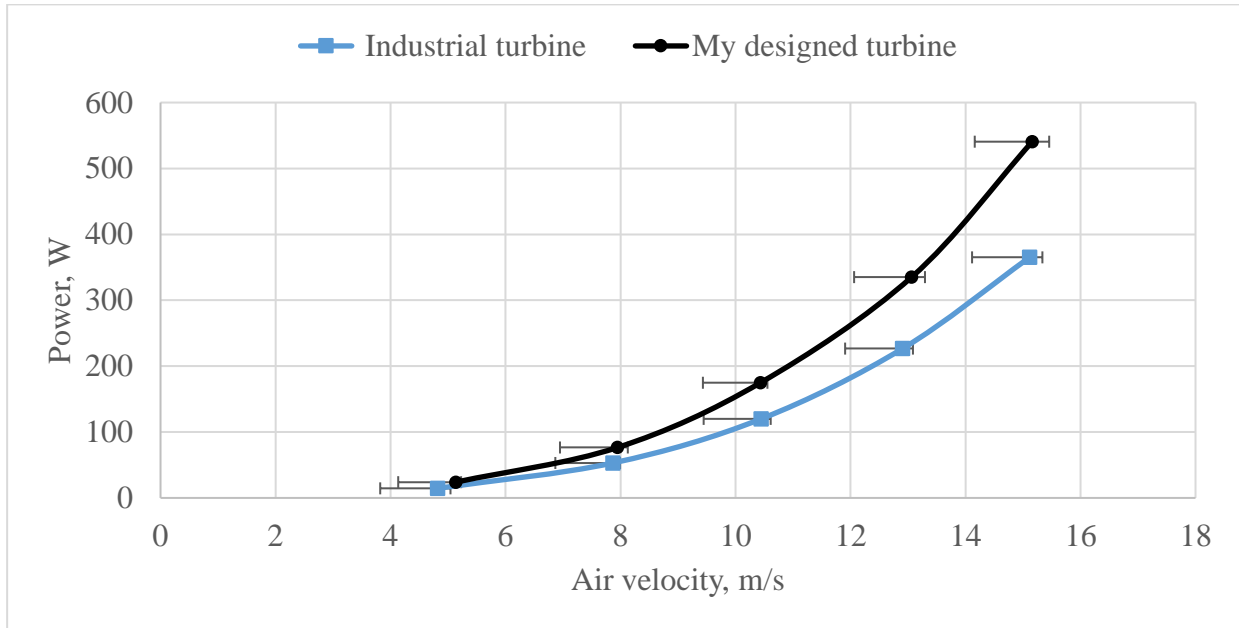


Fig. 4.22. Power of the turbine vs. the inlet velocity

Power coefficient and tip speed ratio variables have to be determined from the measured quantity, as shown in Table 4.9 .Fig. 4.23 shows the power coefficient that achieved according to tip speed ratio. The highest power coefficient of the designed turbine is 0.45 achieved at a 2.8 tip speed ratio, because it was designed at 5.5 tip speed ratio, however, it has many operation points around 3 tip speed ratios. The highest power coefficient of the industrial turbine is 0.30 achieved at a 3.3 tip speed ratio. The designed turbine achieved power coefficient 1.5 times (approximately) higher than the other turbine.

Table 4.9 Sample of the exerimental data

My Designed turbine				
Inlet Velocity (m/s)	Rotational speed (rpm)	Outlet Power (W)	Power Coefficient	Tip Speed ratio
4.949637112	476.9230769	23.33086675	0.44540822	5.045144391
7.902899913	823.0769231	75.96867313	0.3563055	5.453214313
10.56070584	612.3076923	173.0338108	0.34009446	3.035815624
13.03536116	727.6923077	320.791605	0.33527504	2.922963135
15.38203959	878.4615385	536.8006359	0.34144336	2.990249657

4. Results

16.66507328	1026.153846	767.3410202	0.38380812	3.224065615
Industrial turbine				
Inlet Velocity (m/s)	Rotational speed (rpm)	Outlet Power (W)	Power Coefficient	Tip speed ratio
5.170658438	280	17.64671834	0.29551112	2.835376943
7.984517832	520	54.18487745	0.24642198	3.409991299
10.45852021	735.3846154	122.2511203	0.24739422	3.681653585
12.74871903	916.9230769	219.740332	0.24550343	3.76586698
15.13228875	1123.076923	360.1664686	0.24062284	3.88600635

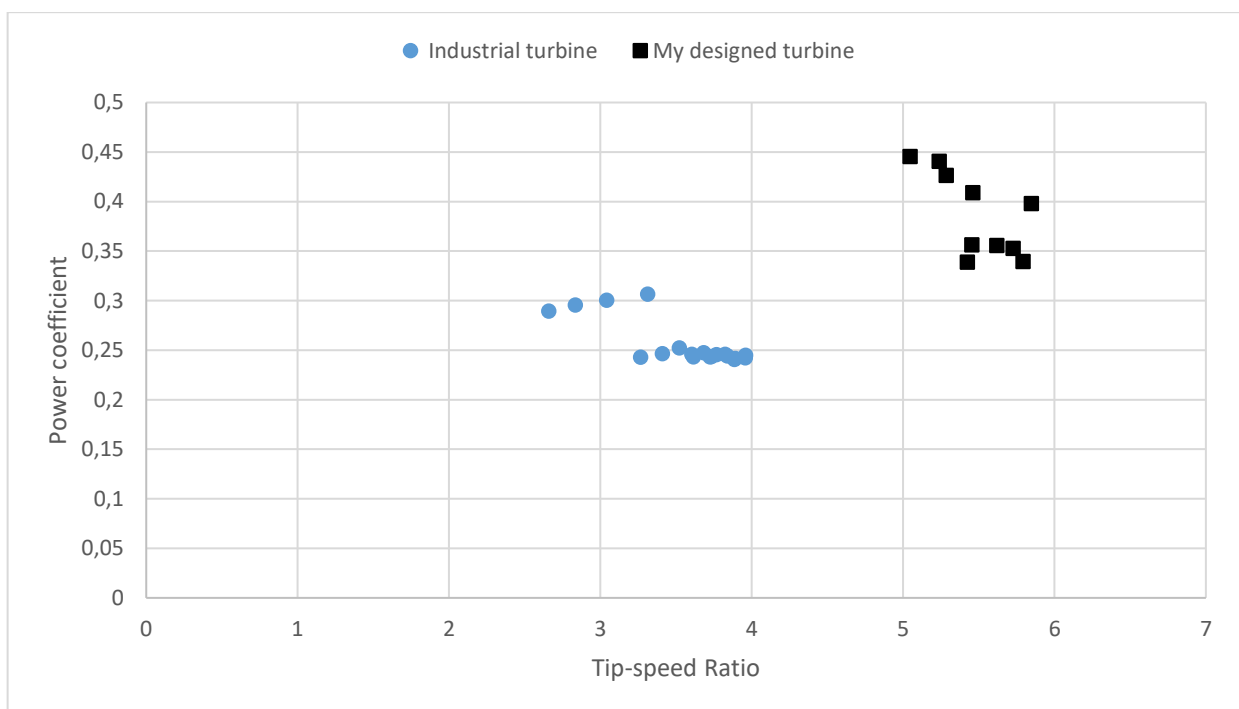


Fig. 4.23. Power coefficient of the tested turbines

4.7. New scientific results

In this section the unique scientific results investigated in my study are shown as following:

1. Development of a modified mathematical model of solar chimney power plant

My modified mathematical model calculates the temperature distribution of collector and flow field inside the SCPP with fewer assumptions than the existing models in the literature in the theoretical analysis. The aim of this model is to calculate the essentials terms of the turbine design. SCPP is influenced by many parameters that effect of the performance of the turbine, however, the solar radiation and mass flow rate are essential variables, which should be studied. The collector is divided to sections at radial position and I applied my MATLAB code on at every section, my model calculates variation of temperature through the radial direction of the collector

To validate the mathematical model, calculated results were compared with the experimental results of the prototype from Manzanares, Spain. The deviation of collector loss coefficient,

collector exit temperature, pressure drop of turbine, and output power are 1.808%, 5.943%, 6.668% and 0.5909% respectively, which are acceptable values.

My new mathematical model shows that the output power of SCPP is a function of the mass flow and solar radiation. So, the recommendation for optimum operation of the SCPP using an optimization algorithm, which can be applied by changing the turbine speed or changing the blade setting angle.

2. New methodology of turbine design working on SCPP

I presented a new design of axial flow turbine based on the blade element theory (BET), which is modified to improve the performance of the wind turbine by the concept of argument diffuse wind turbine (ADWT). The speed ratio, γ , and tip speed ratio, λ , are the main parameters that control of the blade shape and make the blade more suitable for its enclosure.

Aerodynamic analysis of the wind turbine consists of actuator disc theory that applies the momentum concept on the infinite number of the blade rotor, rotor disc theory that takes into account the rotation effect of the rotor, and blade element theory (BET) that considered the force acting on an element of the blade. The analysis is incorporated with the diffuser duct effect to make the blade more sensitive and to have efficient performance during its working inside the duct. By solving equations of the BET theory, the chord distribution and twist angle are obtained presenting the final shape of the blade turbine.

Blade shape of solar chimney turbine is optimized to achieve maximum output power possible form SCPP. My optimization procedure is implemented using iteration algorithm within MATLAB. The interface between MATLAB and XFOIL is used to obtain FX W-151-A aerofoil data. MATLAB code is validated with the previous design that presented by Vaz and Wood, (2016). My measurements showed (Fig.4.23) that the power coefficient of the presented design has reasonable value reaching 0.45 at design point condition (5.5 of tip speed ratio). Therefore, improved to reach the power coefficient 0,45 while the original design achieves power coefficient 0,3 at design point.

3. The influence of the solar collector shape

I used CFD to study velocity and temperature distribution inside collectors that have the square and circular shapes with same surface area. The 3D CFD model of the whole SCPP with turbine and radiation model is carried out. To achieve that purpose, I used ANSYS CFX software for solving the governing equation with the k-omega turbulence model and validate calculated results by comparing to experimental data of Aswan prototype. The instantaneous temperature distribution at different sections and rotational speed of the turbine generator unit are measured during a period of time. Then, I compared the two shapes of the solar chimney collector at constant surface area.

The collector has two common shapes: circular collector and square shaped collector with same area, for studying the more efficient shape, the geometric calculation shows the square shape collector increases the inlet area by 11.4 % than the circular collector. The airflow isn't a uniform distribution on the inlet area because of low inlet air velocity, the reverse airflow takes a place on the geometric inlet area and the effective inlet area present the actual part of a geometric inlet area that allows the airflow inside the collector. The square collector increases the effective inlet area by approximately 30% at the same inlet height, the mass flow rate of square shape is consequently

4. Results

increased by 4.3 %. However, solar radiation exposed to the same surface area in both cases, but the circular shape achieves 0.683 °C higher than the square shape collector of the average exit temperature. Due to the increase in the mass flow rate, the output power that produces increases by 7.6 % based on the square calculation result at constant surface area.

.

5. CONCLUSIONS AND SUGGESTIONS

Solar chimney power plant (SCPP) is a new technology that uses solar air heating and chimney effect to produce electricity. The operating conditions of SCPP impose special properties on the solar chimney turbine. So, the turbine has characteristics mixing between gas turbine and wind turbine. The main aim of this study is to determine the more suitable design theory for a turbine that works inside SCPP. Subsequently, we use CFD simulation to compare performances of three different designs: DAWT (diffuser argument wind turbine) design, MTHM (Matrix through-flow method) design, and Aswan design that is applied classic blade element theory.

The CFD results present the distribution of velocity and temperature for studying the square and circular shape of collectors. The conclusion that the square collector achieved higher output power than the circular collector by 7.6 % at the same surface area Exposed to solar radiation, additionally, the square shape causes a turbulent flow pattern due to change in flow stream lengths that assists to improve the heat transfer process.

The mathematical model is presented, it depends on easily measurable quantities to estimate the performance of SCPP and calculate the design parameter of a solar chimney turbine. The validation of the mathematical model is carried out by comparing its result with the experimental data from the prototype in Manzanares. The comparison shows good agreement.

The blade shape of the solar chimney turbine is optimized to achieve maximum output power possible from SCPP. The optimization procedure is implemented using an iteration algorithm within MATLAB. The interface between MATLAB and XFOIL is used to obtain FX W-151-A aerofoil data. MATLAB code is validated with the previous design that is presented by Vaz and Wood, (2016). Power coefficient of the presented design has reasonable value reaching 0.7250 at design point condition, which is higher than the Betz limit. Additionally, the output power is improved by 15.19 % to reach 55.752 kW while the original design achieves 48.4 kW.

The blade that was designed for SCPP, is manufactured by 3D printing, then the whole rotor of the turbine and industrial turbine are tested within the wind tunnel. The pressure drop of the designed turbine is higher than the industrial turbine by 1.5 times approximately. Generally, the designed turbine has more performance than the industrial one. The highest power coefficient of the designed turbine is 0.45, while the highest power coefficient of the industrial turbine is 0.31. the designed turbine produces 12.55% higher than the industrial one as average increase on all points.

For the future works; The modern energy field recently depends on the renewable energy system such as a solar chimney power plant (SCPP). The field testing of SCPP is a main aim. The solar radiation is source of energy in SCPP, which depend on climate condition of operation location. The field measurement provides realistic data that forms the real performance of the solar chimney system, so, the field experiment is an essential step should be carried out before proposing the SCPP in the markets. Studying the heat storage system takes also a great part of the development of the SCPP system.

For same reasons that mentioned above (making commercial system and increasing both reliability and expansibility), studying the ability of cooperation between Solar chimney system with other solar systems such as photovoltaic or Water desalination will be focused. Hybrid system increases utility of solar energy, it improves effectiveness of the solar system and expands the solar appliances.

6. SUMMARY

AXIAL FLOW TURBINE FOR SOLAR UPDRAFT TOWERS

In this work, a chief aim is an improvement of performing solar chimney power plants (SCPPs) by making its turbine more efficient, The SCPP is a modernistic solar technology that powered combination of solar heating and chimney effect. We developed a comprehensive mathematical model to understand the working environment of the turbine and to calculate the parameters of design, this model calculated the pressure and temperature at some position of SCPP and mass flow rate through it by the iterative code that is implemented by MATLAB.

Blade element theory with a diffuser is selected for designing the solar chimney turbine, the theory takes into account the shape of surrounding duct, that give the designed blades more sensitivity and harmony with its duct. the parameters of the blade geometry (chord distribution and twist angle) calculated by MATLAB code, which optimize the blade element-momentum theories equations to achieving maximum output power. The MATLAB code is interfaced with *XFOIL* program to load the results data of the aerofoil which you can then use in iterative algorithm.

To calculate the design parameter, the comprehensive mathematical model is carried, which has an ability to describe the flow inside solar chimneys. An iteration algorithm is implemented using MATLAB to obtain optimization of the turbine blade chord and twist angle distributions in the presence of a diffuser. The comparison of the mathematical model results and experimental data of Manzanares prototype reveal the good agreement, validating our mathematical model.

Computational fluid dynamics technique (CFD) is used also for studying the performed of SCPP and comparing three different designs of the solar chimney turbine for a substantiation the more suitable theory to design solar chimney turbines. We solved the governing equation of the whole SCPP unit using the computational fluid dynamics module of ANSYS CFX v18.1. The computational results were compared with experimental data to validate it. The testing of SCPP prototype has been carried out in Aswan, Egypt, where the climate is suitable for commercial SCPP units. The theoretical comparison between the three different designs showed that the highest output power is achieved by the design that applied DAWT (diffuser argument wind turbine) theory. Three dimensional CFD simulations were made to calculate the temperature and velocity distribution inside two different shapes of SCPP collector. The conclusion is that the square-shaped collector achieved higher output power than the circular collector by 7.6 % at the same surface area exposed to solar radiation.

The blade that was designed for SCPP, is manufactured by 3D printing. we measured the power, flow rate, rotational speed and pressure drop of the designed and industrial turbines within the wind tunnel, and the power coefficient of the turbines are calculated by measured values. The pressure drop of the designed turbine is higher than the industrial turbine by 1.5 times approximately. Generally, the designed turbine has more performance than the industrial one. The highest power coefficient of the designed turbine is 0.45, while the highest power coefficient of the industrial turbine is 0.31. The designed turbine produces 12.55% higher than the industrial one.

7. ÖSSZEFOGLALÁS (SUMMARY IN HUNGARIAN)

A DOLGOZAT CÍME MAGYARUL: AXIÁLIS ÁTÖMLÉSŰ TURBINA NAPKÉMÉNYHEZ

A szakirodalmi összefoglaló röviden foglalkozik a globális energetikai problémákkal, és a növekvő energiaigény kielégítésére szolgáló egyik megoldást, a napkémények alkalmazását részletesen bemutatja. A napkéményekkel kapcsolatos szakirodalmi forrásokat részletesen elemezve láthatjuk, hogy a napkémények hatékonyságának vizsgálatával foglalkozó kutatók számos matematikai modellt alkottak abból a célból, hogy optimális geometriát tudjanak kialakítani, ugyanakkor más kutatók pedig kísérleti vizsgálatot végeztek a napkémények működésével kapcsolatos jelenségek feltárása érdekében.

A napkémény hatékony működése szempontjából a benne működő turbina kulcsfontosságú szerepet játszik, emiatt számos kutató vizsgálta részletesen a napkéményben működő turbinákat. A napkéményben alkalmazott turbina tulajdonságai a szél- és gázturbinák között helyezkednek el. Számos elméleti vizsgálatot végeztek az ilyen típusú turbinák tervezésével kapcsolatban. Ebben a szakirodalmi összefoglalóban a csőben elhelyezett turbinák működésével kapcsolatos kérdéseket vizsgáljuk, a kutatásos szerint a turbinát körülvevő cső alakja jelentős hatással lehet a turbina hatékonyságára.

Az általam tervezett kutatás célja egy új megközelítés kidolgozása a csőben működő turbinák hatékonyságának növelése érdekében. Az általam kidolgozott elvek alapján megtervezett turbina alkalmazásával a napkémény hatékonyságának növelésére nyílhat mód. Egy új matematikai modell kidolgozásával pedig lehetőség nyílik a napkémények teljesítményének pontosabb becslésére. A napkéményben lejátszódó áramlási folyamatokról is pontosabb képet kaphatunk kutatásaim eredményeként.

8. APPENDICES

A.1. Bibliography

1. Ahirwar, J. and Sharma, P. P. (2019) ‘Analyzing the Effect of Solar Chimney Power Plant by Varying Chimney Height , Collector Slope and Chimney Diverging Angle’, 6(7), pp. 213–219.
2. Ahmed, O. K. *et al.* (2020) ‘A new method to improve the performance of solar chimneys A New Method to Improve the Performance of Solar Chimneys’, 020018(March).
3. Akeel, S. A. M. S. and Najjar, Y. S. H. (2013) ‘Comparison of free- and forced-vortex designs for computation of mass flux in an axial gas turbine stage’, *Energy Education Science and Technology Part A: Energy Science and Research*, 31(1), pp. 55–66.
4. Al-Kayiem, H. H. *et al.* (2019) ‘Performance evaluation of hybrid solar chimney for uninterrupted power generation’, *Energy*, 166, pp. 490–505. doi: 10.1016/j.energy.2018.10.115.
5. Al-Kayiem, H. H. and Aja, O. C. (2016) ‘Historic and recent progress in solar chimney power plant enhancing technologies’, *Renewable and Sustainable Energy Reviews*. Elsevier Ltd, pp. 1269–1292. doi: 10.1016/j.rser.2015.12.331.
6. ANSYS CFX-Solver theory guide.
7. *ANSYS CFX Introduction User Help*.
8. Aranake, A. C., Lakshminarayan, V. K. and Duraisamy, K. (2013) ‘Computational analysis of shrouded wind turbine configurations’, in *51st AIAA Aerospace Sciences Meeting including the New Horizons Forum and Aerospace Exposition 2013*. doi: 10.2514/6.2013-1211.
9. Arzpeyma, M. *et al.* (2019) ‘Solar chimney power plant and its correlation with ambient wind effect’, *Journal of Thermal Analysis and Calorimetry*, (0123456789). doi: 10.1007/s10973-019-09065-z.
10. Von Backström, T. W. *et al.* (2008) ‘State and recent advances in research and design of solar chimney power plant technology’, *VGB PowerTech*, 88(7).
11. von Backström, T. W. and Gannon, A. J. (2004) ‘Solar chimney turbine characteristics’, *Solar Energy*, 76(1–3), pp. 235–241. doi: 10.1016/j.solener.2003.08.009.
12. Baltazar, J., Falcão de Campos, J. A. C. and Bosschers, J. (2015) ‘On the modelling of the flow in ducted propellers with a panel method’, *4th International Symposium on Marine Propulsors (smp’15)*, (June), pp. 578–586.
13. Barbosa, D. L. M. *et al.* (2015) ‘An investigation of a mathematical model for the internal velocity profile of conical diffusers applied to dawts’, *Anais da Academia Brasileira de Ciencias*, 87(2), pp. 1133–1148. doi: 10.1590/0001-3765201520140114.
14. BATCHELOR, G. K. (2000) *An Introduction to Fluid Dynamics*, Cambridge University Press.
15. Bazilevs, Y. *et al.* (2011) ‘3D simulation of wind turbine rotors at full scale. Part II: Fluid-structure interaction modeling with composite blades’, *International Journal for Numerical Methods in Fluids*, 65(1–3), pp. 236–253. doi: 10.1002/flid.2454.
16. Burton, T. *et al.* (2011) *Wind Energy Handbook*, *Wind Energy Handbook*. Chichester, UK: John Wiley & Sons, Ltd. doi: 10.1002/9781119992714.
17. Carcangiu, C. E. (2008) *CFD-RANS Study of Horizontal Axis Wind Turbines*, *Meccanica*. Università degli Studi di Cagliari.
18. Celik, I. B. (Wester. V. U. (1999) ‘Introductory turbulence modeling’, *Western Virginia University Class Notes*, (December), p. 94.
19. Chen, T. Y., Liao, Y. T. and Cheng, C. C. (2012) ‘Development of small wind turbines for moving vehicles: Effects of flanged diffusers on rotor performance’, *Experimental Thermal and Fluid Science*, 42, pp. 136–142. doi: 10.1016/j.expthermflusci.2012.05.001.
20. Chen, X.-Y. and Zha, G.-C. (2005) ‘Fully coupled fluid–structural interactions using an efficient high resolution upwind scheme’, *Journal of Fluids and Structures*, 20(8), pp. 1105–1125. doi: 10.1016/j.jfluidstructs.2005.02.011.

21. Cirillo, L. *et al.* (2015) 'NUMERICAL AND EXPERIMENTAL INVESTIGATIONS ON A SOLAR CHIMNEY INTEGRATED IN A BUILDING FACADE', *International Journal of Heat and Technology*, 33(4), pp. 246–254. doi: 10.18280/ijht.330433.
22. Clifton-Smith, M. J. (2009) 'Wind Turbine Blade Optimisation with Tip Loss Corrections', *Wind Engineering*, 33(5), pp. 477–496. doi: 10.1260/030952409790291226.
23. Denantes, F. and Bilgen, E. (2006) 'Counter-rotating turbines for solar chimney power plants', *Renewable Energy*, 31(12), pp. 1873–1891. doi: 10.1016/j.renene.2005.09.018.
24. Dhahri, A. and Omri, A. (2013) 'A Review of solar Chimney Power Generation Technology', *International Journal of Engineering and Advanced Technology (IJEAT)*, 2(3), pp. 1–17.
25. Digaskar, D. a. (2010) 'Simulations of Flow Over Wind Turbines', *Thesis*, (May), pp. 1–100.
26. Duffie, J. A. and Beckman, W. A. (2013) *Solar Engineering of Thermal Processes: Fourth Edition, Solar Engineering of Thermal Processes: Fourth Edition*. John Wiley and Sons. doi: 10.1002/9781118671603.
27. Duquette, M. M. and Visser, K. D. (2003) 'Numerical implications of solidity and blade number on rotor performance of horizontal-axis wind turbines', *Journal of Solar Energy Engineering, Transactions of the ASME*, 125(4), pp. 425–432. doi: 10.1115/1.1629751.
28. Elkady, E.-A. *et al.* (2019) 'An Investigation on a Solar Chimney Model', *Journal of Al-Azhar University Engineering Sector*, 14(51), pp. 485–494. doi: 10.21608/aej.2019.33353.
29. Elmagid, W. M. A. and Keppler, I. (2017) 'Axial flow turbine for solar chimney', *Hungarian Agricultural Engineering*, (32), pp. 29–37. doi: 10.17676/hae.2017.32.29.
30. Elmagid, W. M. A., Keppler, I. and Molnar, I. (2020) 'Efficient Axial Flow Turbine for Solar Chimney', *Journal of Thermal Science and Engineering Applications*, 12(3). doi: 10.1115/1.4044903.
31. Fallah, S. H. and Valipour, M. S. (2019) 'Evaluation of solar chimney power plant performance: The effect of artificial roughness of collector', *Solar Energy*, 188(March), pp. 175–184. doi: 10.1016/j.solener.2019.05.065.
32. Fluri, T. P. and von Backström, T. W. (2008) 'Comparison of modelling approaches and layouts for solar chimney turbines', *Solar Energy*, 82(3), pp. 239–246. doi: 10.1016/j.solener.2007.07.006.
33. G.J.W. Bussel, van (1999) 'An assessment of the performance of diffuser augmented wind turbines (DAWT's)'. American Society of Mechanical Engineers, p. 1.
34. Gannon, A. J. and Von Backström, T. W. (2002a) 'Solar chimney turbine part 1 of 2: Design', *International Solar Energy Conference*, pp. 335–341. doi: 10.1115/SED2002-1070.
35. Gannon, A. J. and Von Backström, T. W. (2002b) 'Solar chimney turbine part 2 of 2: Experimental results', *International Solar Energy Conference*, pp. 343–349. doi: 10.1115/SED2002-1071.
36. Gannon, A. J. and Von Backström, T. W. (2003) 'Solar chimney turbine performance', *Journal of Solar Energy Engineering, Transactions of the ASME*, 125(1), pp. 101–106. doi: 10.1115/1.1530195.
37. Gilbert, B. L. and Foreman, K. M. (1979) 'Experimental Demonstration of the Diffuser-Augmented Wind Turbine Concept.', *Journal of energy*, 3(4), pp. 235–240. doi: 10.2514/3.48002.
38. Gilbert, B. L. and Foreman, K. M. (1983) 'Experiments with a diffuseraugmented model wind turbine', *Journal of Energy Resources Technology, Transactions of the ASME*, 105(1), pp. 46–53. doi: 10.1115/1.3230875.
39. Guerri, O., Hamdouni, A. and Sakout, A. (2008) 'Fluid Structure Interaction of Wind Turbine Airfoils', *Wind Engineering*, 32(6), pp. 539–557. doi: 10.1260/030952408787548875.
40. Guo, P. *et al.* (2013) 'Numerical analysis of the optimal turbine pressure drop ratio in a solar chimney power plant', *Solar Energy*, 98, pp. 42–48. doi: 10.1016/j.solener.2013.03.030.
41. Guo, P. *et al.* (2019) 'Questions and current understanding about solar chimney power plant: A review', *Energy Conversion and Management*, 182(December 2018), pp. 21–33. doi: 10.1016/j.enconman.2018.12.063.

42. Haaf, W. *et al.* (1983) 'Part I: Principle and Construction of the Pilot Plant in Manzanares', *International Journal of Solar Energy*, 2(1), pp. 3–20. doi: 10.1080/01425918308909911.
43. Haaf, W. (1984) 'Part II: Preliminary Test Results from the Manzanares Pilot Plant', *International Journal of Solar Energy*, 2(2), pp. 141–161. doi: 10.1080/01425918408909921.
44. Haghghat, S. *et al.* (2019) 'Fluid dynamics analysis for different photovoltaic panel locations in solar chimney', *Energy Conversion and Management*, 191(March), pp. 71–79. doi: 10.1016/j.enconman.2019.03.053.
45. Hamdan, M. O. and Rabbata, O. (2012) 'Experimental solar chimney data with analytical model prediction', *World Renewable Energy Forum, WREF 2012, Including World Renewable Energy Congress XII and Colorado Renewable Energy Society (CRES) Annual Conferen*, 1, pp. 327–332.
46. Hansen, M. O. L., Sørensen, N. N. and Flay, R. G. J. (2000) 'Effect of Placing a Diffuser around a Wind Turbine', *Wind Energy*, 3(4), pp. 207–213. doi: 10.1002/we.37.
47. Hassan, A., Ali, M. and Waqas, A. (2018) 'Numerical investigation on performance of solar chimney power plant by varying collector slope and chimney diverging angle', *Energy*, 142, pp. 411–425. doi: 10.1016/j.energy.2017.10.047.
48. Hjort, S. and Larsen, H. (2014) 'A Multi-Element Diffuser Augmented Wind Turbine', *Energies*, 7(5), pp. 3256–3281. doi: 10.3390/en7053256.
49. ten Hoopen, P. D. C. (2009) 'An experimental and computational investigation of a diffuser augmented wind turbine with an application of vortex generators on the diffuser trailing edge', p. 98.
50. Igra, O. (1985) 'Research and development for shrouded wind turbines.', 21((ed.), Bedford, U.K., H.S. Stephens & Assocs., 1985, Paper D7, pp.236-245. (EUR 9622)).
51. Jafari, S. A. H. and Kosasih, B. (2014) 'Flow analysis of shrouded small wind turbine with a simple frustum diffuser with computational fluid dynamics simulations', *Journal of Wind Engineering and Industrial Aerodynamics*, 125, pp. 102–110. doi: 10.1016/j.jweia.2013.12.001.
52. Kannan, T. S., Mutasher, S. A. and Lau, Y. H. K. (2013) 'Design and flow velocity simulation of diffuser augmented wind turbine using CFD', *Journal of Engineering Science and Technology*, 8(4), pp. 372–384.
53. Kasaeian, A. B., Heidari, E. and Vatan, S. N. (2011) 'Experimental investigation of climatic effects on the efficiency of a solar chimney pilot power plant', *Renewable and Sustainable Energy Reviews*, 15(9), pp. 5202–5206. doi: 10.1016/j.rser.2011.04.019.
54. Kiwan, S., Al-Nimir, M. and Salim, I. (2020) 'A hybrid solar chimney/photovoltaic thermal system for direct electric power production and water distillation', *Sustainable Energy Technologies and Assessments*, 38(February), p. 100680. doi: 10.1016/j.seta.2020.100680.
55. Kobayashi, I. and Delahanty, D. L. (2014) 'Awake/sleep cortisol levels and the development of posttraumatic stress disorder in injury patients with peritraumatic dissociation.', *Psychological Trauma: Theory, Research, Practice, and Policy*, 6(5), pp. 449–456. doi: 10.1037/a0033013.
56. Koonsrisuk, A. and Chitsomboon, T. (2009) 'A single dimensionless variable for solar chimney power plant modeling', *Solar Energy*, 83(12), pp. 2136–2143. doi: 10.1016/j.solener.2009.07.015.
57. Koonsrisuk, A. and Chitsomboon, T. (2013) 'Mathematical modeling of solar chimney power plants', *Energy*, 51, pp. 314–322. doi: 10.1016/j.energy.2012.10.038.
58. Krätzig, W. B. (2013) 'Physics, computer simulation and optimization of thermo-fluidmechanical processes of solar updraft power plants', *Solar Energy*, 98, pp. 2–11. doi: 10.1016/j.solener.2013.02.017.
59. Lawn, C. J. (2003) 'Optimization of the power output from ducted turbines', *Proceedings of the Institution of Mechanical Engineers, Part A: Journal of Power and Energy*, 217(1), pp. 107–118. doi: 10.1243/095765003321148754.
60. Li, J. yin, Guo, P. hua and Wang, Y. (2012) 'Effects of collector radius and chimney height

- on power output of a solar chimney power plant with turbines’, *Renewable Energy*, 47, pp. 21–28. doi: 10.1016/j.renene.2012.03.018.
61. Matsushima, T., Takagi, S. and Muroyama, S. (2006) ‘Characteristics of a highly efficient propeller type small wind turbine with a diffuser’, *Renewable Energy*, 31(9), pp. 1343–1354. doi: 10.1016/j.renene.2005.07.008.
 62. Michal, L., Maciej, K. and Krzysztof, J. (2016) ‘Analysis and comparison of numerical methods for design and development of small Diffuser-Augmented Wind Turbine (DAWT)’, *IECON Proceedings (Industrial Electronics Conference)*, pp. 5525–5531. doi: 10.1109/IECON.2016.7793199.
 63. Ming, T. *et al.* (2016) ‘Freshwater generation from a solar chimney power plant’, *Energy Conversion and Management*, 113, pp. 189–200. doi: 10.1016/j.enconman.2016.01.064.
 64. Ming, T. *et al.* (2017) ‘A moist air condensing device for sustainable energy production and water generation’, *Energy Conversion and Management*, 138, pp. 638–650. doi: 10.1016/j.enconman.2017.02.012.
 65. Moeller, M. M. and Visser, K. (2010) ‘Experimental and numerical studies of a high solidity, low tip speed ratio DAWT’, in *48th AIAA Aerospace Sciences Meeting Including the New Horizons Forum and Aerospace Exposition*. doi: 10.2514/6.2010-1585.
 66. Mostafa, A. A., Sedrak, M. F. and Dayem, A. M. A. (2011) ‘Performance of a Solar Chimney Under Egyptian Weather Conditions: Numerical Simulation and Experimental Validation’, *Energy Science and Technology*, pp. 49–63. doi: 10.3968/j.est.1923847920110101.004.
 67. Muhammed, H. A. and Atrooshi, S. A. (2019) ‘Modeling solar chimney for geometry optimization’, *Renewable Energy*, 138, pp. 212–223. doi: 10.1016/j.renene.2019.01.068.
 68. Mullett, L. B. (1987) ‘The solar chimney—overall efficiency, design and performance’, *International Journal of Ambient Energy*, 8(1), pp. 35–40. doi: 10.1080/01430750.1987.9675512.
 69. Nizetic, S. and Klarin, B. (2010) ‘A simplified analytical approach for evaluation of the optimal ratio of pressure drop across the turbine in solar chimney power plants’, *Applied Energy*, 87(2), pp. 587–591. doi: 10.1016/j.apenergy.2009.05.019.
 70. Ohya, Y. *et al.* (2008) ‘Development of a shrouded wind turbine with a flanged diffuser’, *Journal of Wind Engineering and Industrial Aerodynamics*, 96(5), pp. 524–539. doi: 10.1016/j.jweia.2008.01.006.
 71. Pasumarthi, N. and Sherif, S. A. (1998a) ‘Experimental and theoretical performance of a demonstration solar chimney model—part I: Mathematical model development’, *International Journal of Energy Research*, 22(3), pp. 277–288. doi: 10.1002/(SICI)1099-114X(19980310)22:3<277::AID-ER380>3.0.CO;2-R.
 72. Pasumarthi, N. and Sherif, S. A. (1998b) ‘Experimental and theoretical performance of a demonstration solar chimney model—Part II: experimental and theoretical results and economic analysis’, *International Journal of Energy Research*, 22(5), pp. 443–461. doi: 10.1002/(SICI)1099-114X(199804)22:5<443::AID-ER381>3.0.CO;2-V.
 73. Patel, S. K., Prasad, D. and Ahmed, M. R. (2014) ‘Computational studies on the effect of geometric parameters on the performance of a solar chimney power plant’, *Energy Conversion and Management*, 77, pp. 424–431. doi: 10.1016/j.enconman.2013.09.056.
 74. Phillips, D. G. (2003) ‘An Investigation on Diffuser Augmented wind Turbine Design’, *Thesis*, 1994, p. 370.
 75. Quaschnig, V. (2014) *Understanding renewable energy systems, Understanding Renewable Energy Systems*. doi: 10.4324/9781315800493.
 76. dos S. Bernardes, M. A., Voß, A. and Weinrebe, G. (2003) ‘Thermal and technical analyses of solar chimneys’, *Solar Energy*, 75(6), pp. 511–524. doi: 10.1016/j.solener.2003.09.012.
 77. Schaffarczyk, A. P. and Phillips, D. (2001) ‘Design principles for a diffusor augmented wind-turbine blade’, *Proc. EWEC*, (June).
 78. Shen, W. Z. *et al.* (2005) ‘Tip loss corrections for wind turbine computations’, *Wind Energy*, 8(4), pp. 457–475. doi: 10.1002/we.153.

79. Shives, M. and Crawford, C. (2011) 'Ducted turbine blade optimization using numerical simulation', *Proceedings of the International Offshore and Polar Engineering Conference*, pp. 407–413.
80. Song, Q. (2012) *Design, Fabrication, and Testing of a New Small Wind Turbine Blade* ABSTRACT DESIGN, FABRICATION, AND TESTING OF A SMALL WIND TURBINE BLADE. University of Guelph.
81. Swinbank, W. C. (1963) 'Long-wave radiation from clear skies', *Quarterly Journal of the Royal Meteorological Society*, 89(381), pp. 339–348. doi: 10.1002/qj.49708938105.
82. Tavares Dias Do Rio Vaz, D. A. *et al.* (2014) 'An extension of the Blade Element Momentum method applied to Diffuser Augmented Wind Turbines', *Energy Conversion and Management*, 87, pp. 1116–1123. doi: 10.1016/j.enconman.2014.03.064.
83. Tian, M. W. *et al.* (2020) 'New optimal design for a hybrid solar chimney, solid oxide electrolysis and fuel cell based on improved deer hunting optimization algorithm', *Journal of Cleaner Production*, 249. doi: 10.1016/j.jclepro.2019.119414.
84. Tingzhen, M. *et al.* (2008a) 'Numerical simulation of the solar chimney power plant systems coupled with turbine', *Renewable Energy*, 33(5), pp. 897–905. doi: 10.1016/j.renene.2007.06.021.
85. Tingzhen, M. *et al.* (2008b) 'Numerical simulation of the solar chimney power plant systems coupled with turbine', *Renewable Energy*, 33, pp. 897–905. doi: 10.1016/j.renene.2007.06.021.
86. Tingzhen, M., Wei, L. and Yuan, P. (2007) 'Numerical analysis of the solar chimney power plant with energy storage layer', in *ISES Solar World Congress 2007, ISES 2007*, pp. 1800–1805. doi: 10.1007/978-3-540-75997-3_368.
87. Tu, J., Yeoh, G. H. and Liu, C. (2018) 'Computational fluid dynamics: A practical approach', in *Computational Fluid Dynamics: A Practical Approach*. 3rd Editio. Elsevier, pp. 255–290.
88. Vaz, J. R. P. and Wood, D. H. (2016) 'Aerodynamic optimization of the blades of diffuser-augmented wind turbines', *Energy Conversion and Management*, 123, pp. 35–45. doi: 10.1016/j.enconman.2016.06.015.
89. Wilcox, D. C. (1988) 'Reassessment of the scale-determining equation for advanced turbulence models', *AIAA Journal*, 26(11), pp. 1299–1310. doi: 10.2514/3.10041.
90. Wood, D. H. (2015) 'Maximum wind turbine performance at low tip speed ratio', *Journal of Renewable and Sustainable Energy*, 7(5). doi: 10.1063/1.4934805.
91. Yan, M. Q. *et al.* (1991) 'Thermo-fluid analysis of solar chimneys', in *American Society of Mechanical Engineers, Fluids Engineering Division (Publication) FED*. Publ by ASME, pp. 125–130.
92. Zhou, X., Wang, F. and Ochieng, R. M. (2010) 'A review of solar chimney power technology', *Renewable and Sustainable Energy Reviews*, 14(8), pp. 2315–2338. doi: 10.1016/j.rser.2010.04.018.
93. Zhou, X. and Xu, Y. (2016) 'Solar updraft tower power generation', *Solar Energy*, 128, pp. 95–125. doi: 10.1016/j.solener.2014.06.029.
94. Zhou, Y. *et al.* (2016) 'Design for the turbine of solar chimney power plant system with vertical collector', *IOP Conference Series: Earth and Environmental Science*, 40(1). doi: 10.1088/1755-1315/40/1/012085.
95. Zuo, L. *et al.* (2011) 'Solar chimneys integrated with sea water desalination', *Desalination*, 276(1–3), pp. 207–213. doi: 10.1016/j.desal.2011.03.052.
96. Zuo, L. *et al.* (2018) 'The effect of different structural parameters on wind supercharged solar chimney power plant combined with seawater desalination', *Energy Conversion and Management*, 176(September), pp. 372–383. doi: 10.1016/j.enconman.2018.09.044.
97. Zuo, L. *et al.* (2019) 'Preliminary study of wind supercharging solar chimney power plant combined with seawater desalination by indirect condensation freshwater production', *Desalination*, 455(July 2018), pp. 79–88. doi: 10.1016/j.desal.2019.01.008.

A.2. Publications related to the thesis

Refereed papers in foreign languages:

1. **A-Elmagid, W. M.** and Keppler, I. (2017) ‘Axial flow turbine for solar chimney’, *Hungarian Agricultural Engineering*, (32), pp. 29–37. doi: 10.17676/hae.2017.32.29.
2. **A-Elmagid, W. M.**, Keppler, I. and Molnar, I. (2020) ‘Efficient Axial Flow Turbine for Solar Chimney’, *Journal of Thermal Science and Engineering Applications*. ASME International, 12(3). doi: 10.1115/1.4044903.
3. **A-Elmagid, W. M.** et al. (2020) ‘Studying the collector performance of updraft solar chimney power plant’, *Journal of Engineering and Technology (JET)*, Vol. 11, No. 1, pp. 1-8, ISSN: 2180-3811
4. **A-Elmagid, W. M.** et al. (2021) ‘A Numerical comparative study of axial flow turbines for solar chimney power plant’, *Case Studies in Thermal Engineering*, 26, p. 101046. doi: 10.1016/j.csite.2021.101046.
5. **Walid M.A Elmagid**, ‘Testing axial flow solar chimney turbine using wind tunnel’ (in progress)

International conference proceedings:

6. **A-Elmagid, W. M.**, and Keppler I. (October 16-19- 2017). Axial Flow Turbine for Solar Chimney. Synergy International Conferences - Engineering, Agriculture and Green Industry Innovation. Gödöllő, Hungary.

International conference abstracts:

7. **A-Elmagid, W. M.** et al. (2019). Load analysis for blades of a solar chimney turbine using Fluid–structure interaction modelling. Synergy International Conferences - Engineering, Agriculture and Green Industry Innovation, Gödöllő, Hungary, November 4-6, 2019. Szent István University Faculty of Mechanical Engineering, (2019) pp. 20, ISBN: 978-963-269-854-0.
8. **A-Elmagid, W. M.** “Design and testing of a small turbine blade at low speed wind”, 22th Workshop on Energy and Environment (EE 2016), December 1-2, 2016, Gödöllő, Hungary
9. **A-Elmagid, W. M.** “Theoretical Investigation of Solar Chimney Power Plant Installed in Aswan City”, 6th Scientific Workshop by Egypt’s Office for Cultural and Educational Relations Vienna, 27th of April 2017
10. **A-Elmagid, W. M.** “Mathematical model of the solar updraft chimney”, 23rd Workshop on Energy and Environment (EE 2017), November 30 - December 1, 2017, Gödöllő, Hungary

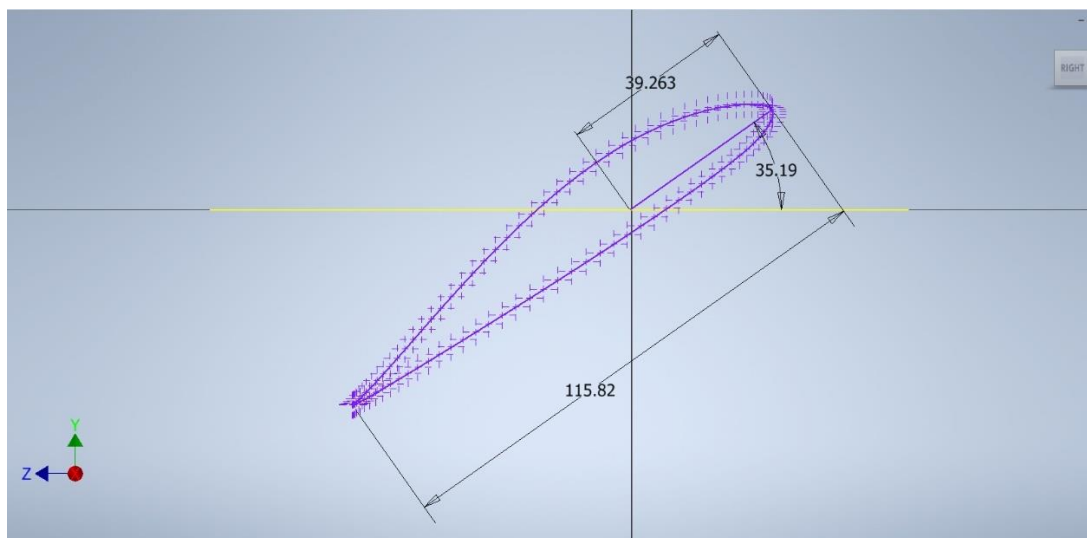
A.3. Engineering Drawing

A.3.1 Drawing of my designed blade.

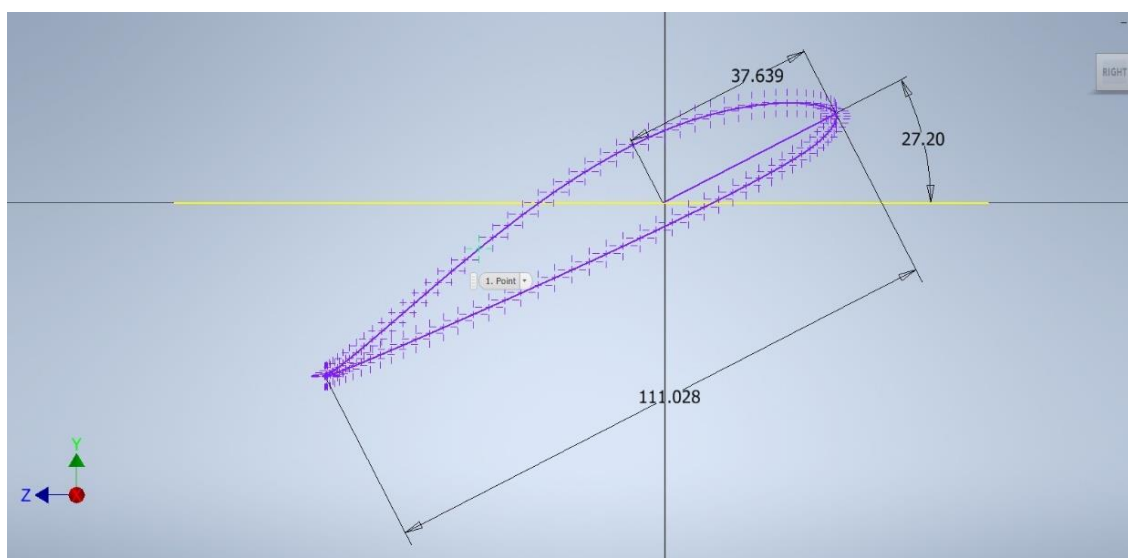
I present the results of the calculations of my code according to Fig. 3.6 in section 3.3 in following table that shows the chord distribution and twist angle of my design blade. I used in Aerofoil FX 79-W-151 to create nine sections, that I can show as:

Section	Raduis (m)	Twist Angle (deg)	Chord(m)
1	0.091111111	35.189045	0.11581959
2	0.14222222	27.198167	0.11102821
3	0.19333333	22.097837	0.10131916
4	0.24444444	18.569049	0.091338009
5	0.29555556	15.990967	0.082277383
6	0.34666667	14.029734	0.074115474
7	0.39777778	12.490179	0.066015699
8	0.44888889	11.250933	0.054930619
9	0.5	10.232765	0.024656165

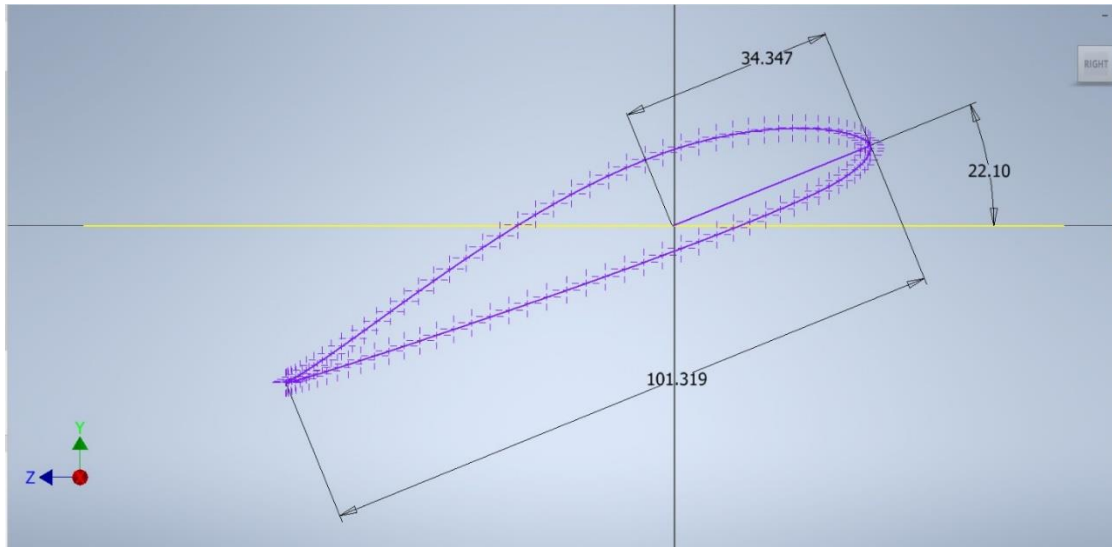
Section 1:



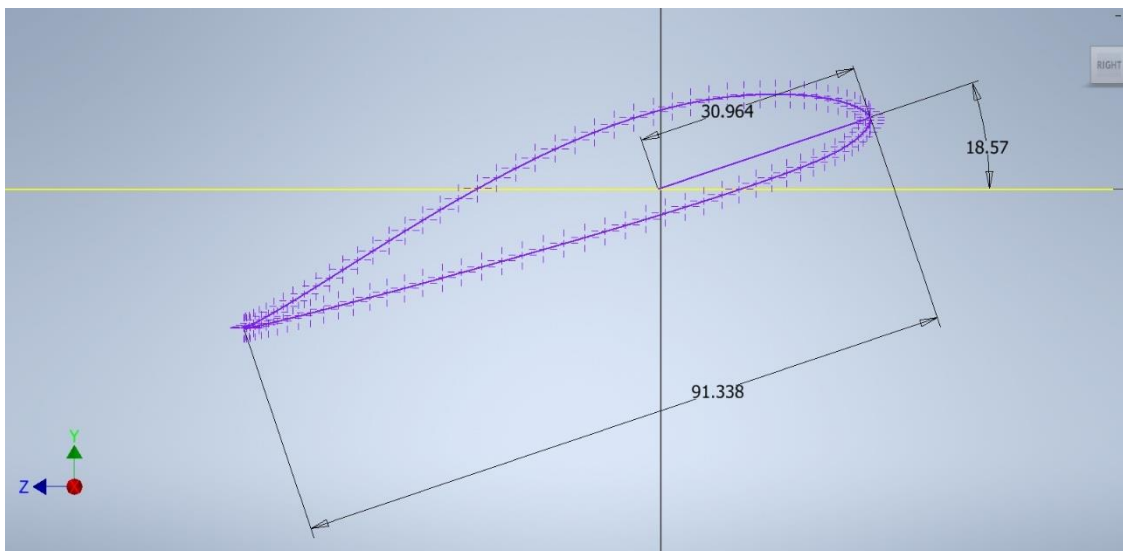
Section 2:



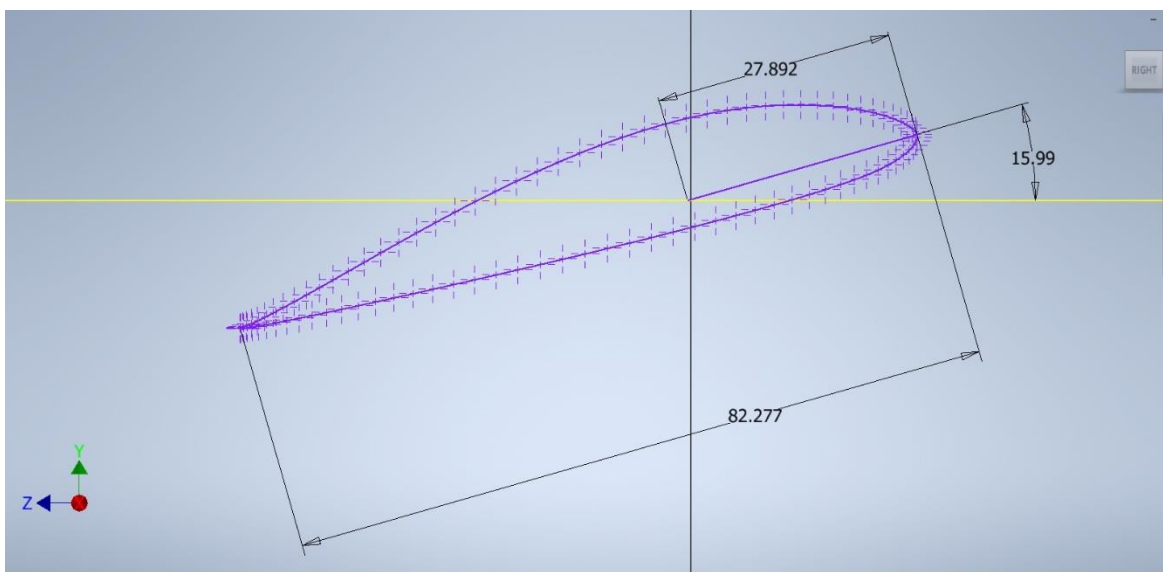
Section 3:



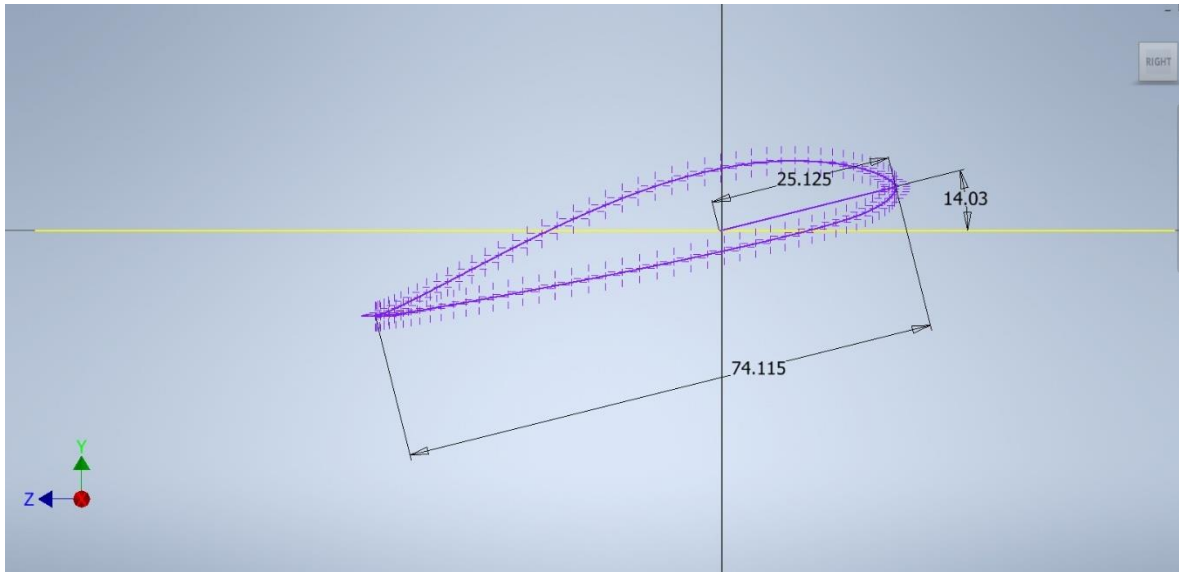
Section 4:



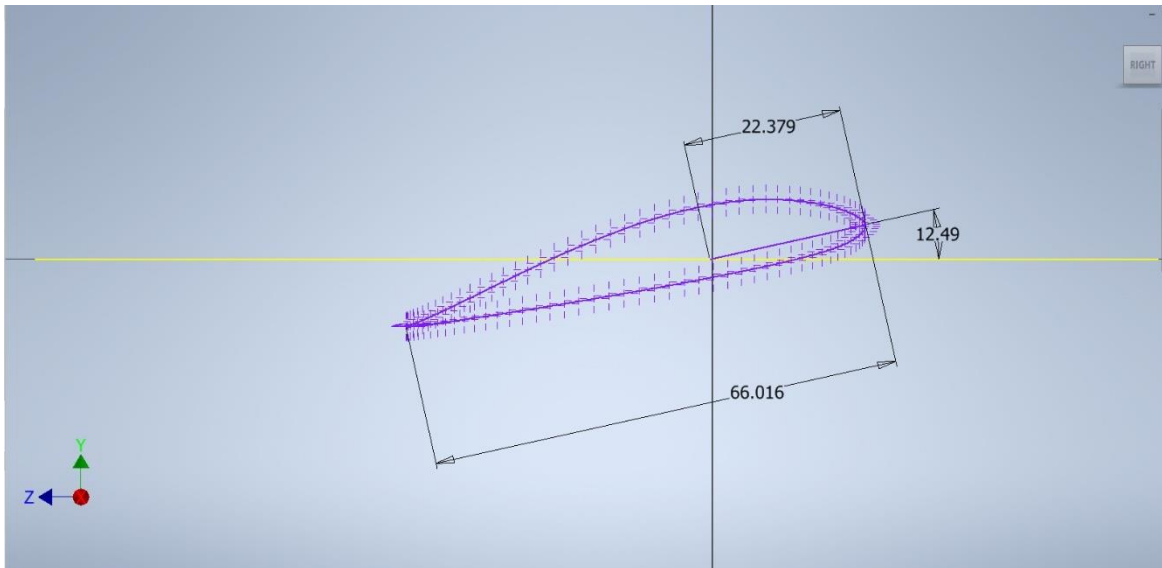
Section 5:



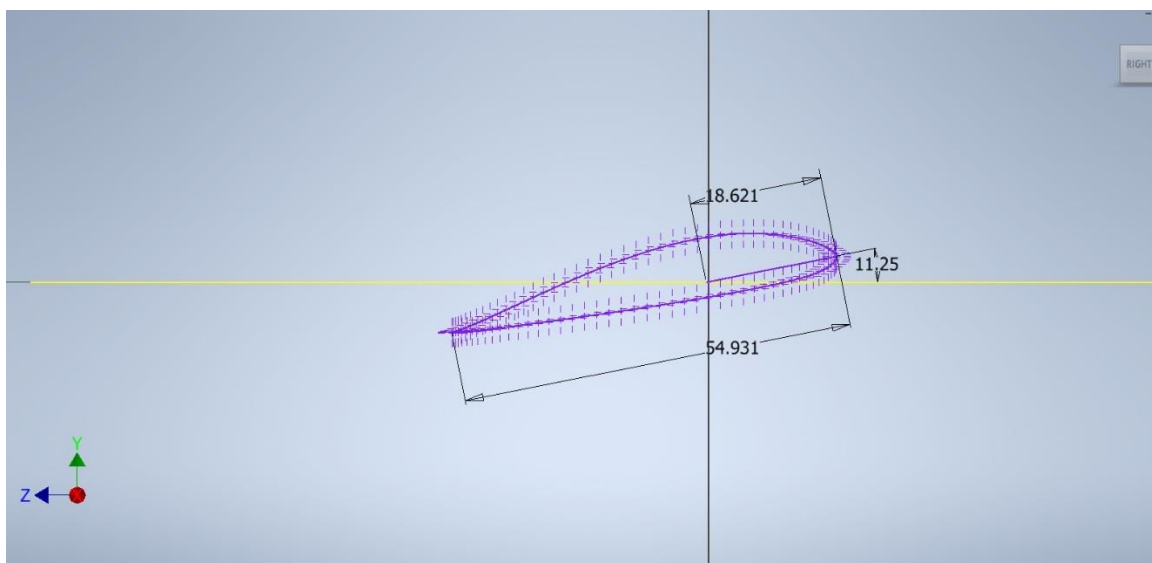
Section 6:



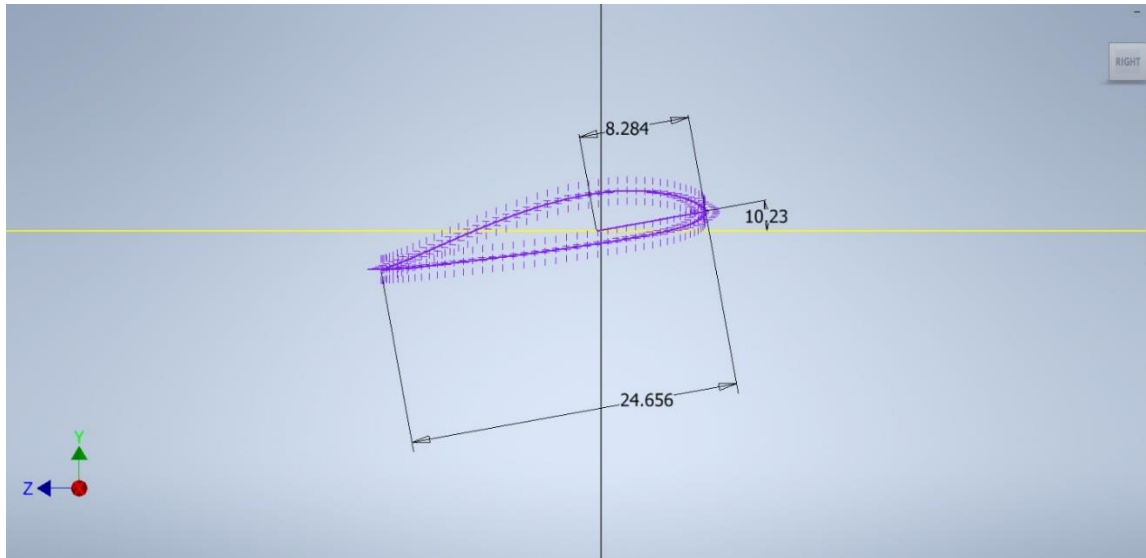
Section 7:



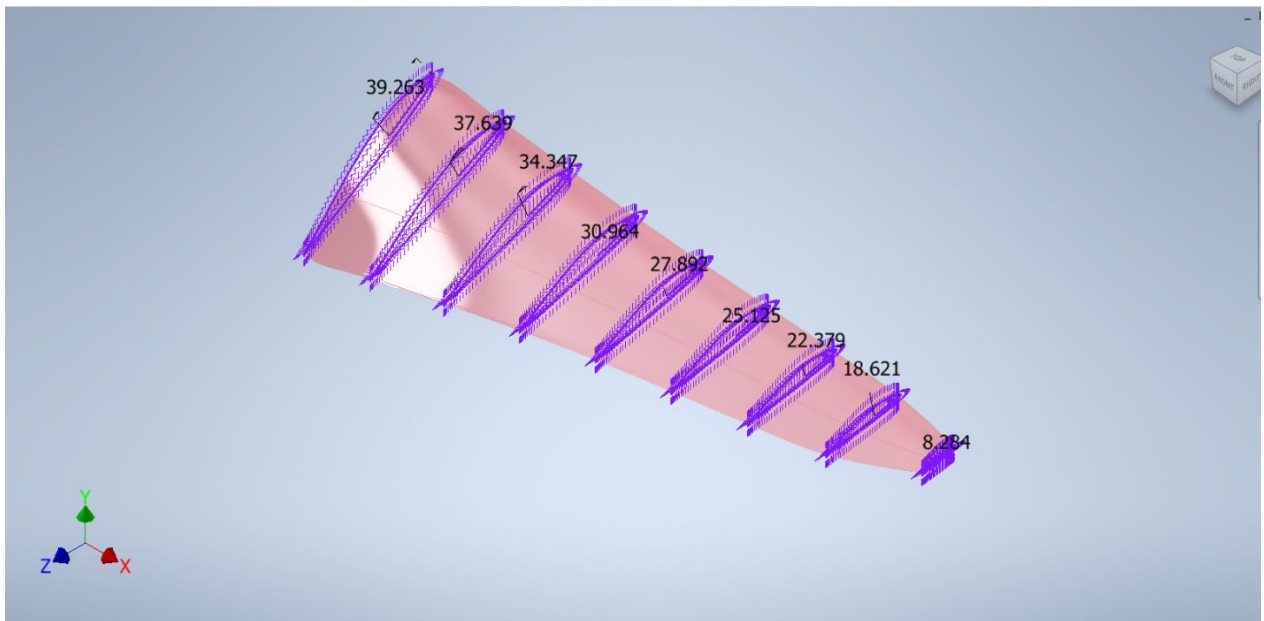
Section 8:



Section 9:

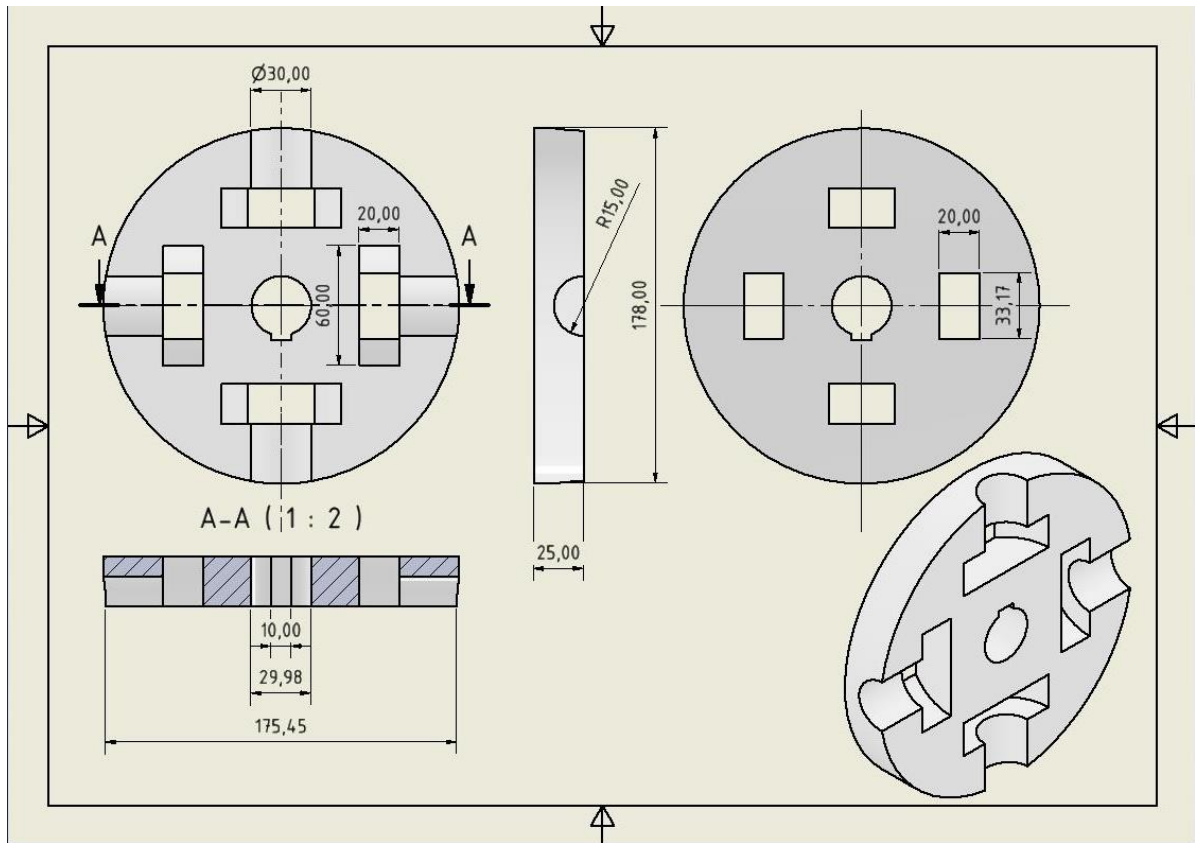


I margin all above section by LOFT order to create the complete blade shape:

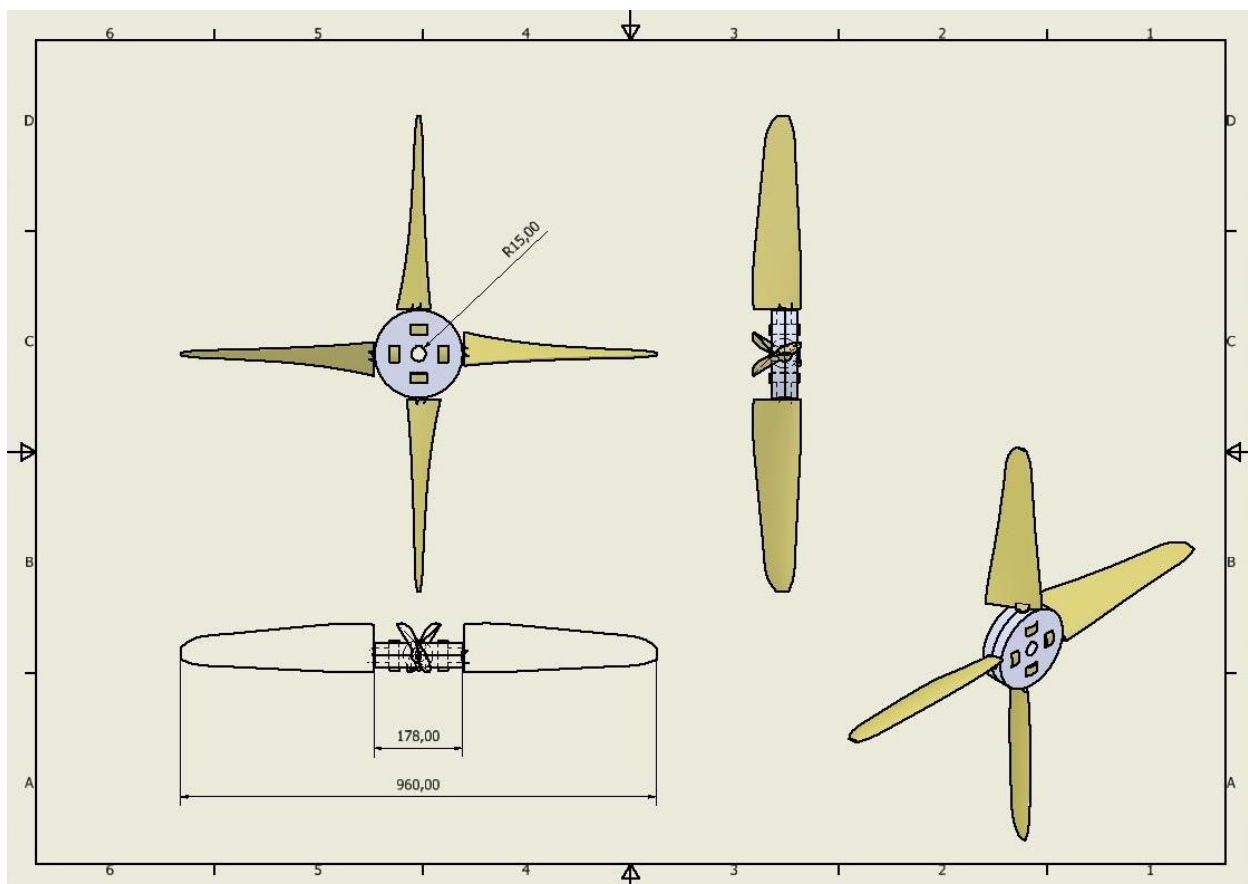


A.3.2 Drawing of the hub

I design the hub to be two similar halves to easy for mounting the blade as shown:



The complete rotor is shown as:



9. ACKNOWLEDGMENTS

This thesis work was supported by the Stipendium Hungaricum Scholarship Program and Mechanical Engineering Doctoral School at the Szent István University, Gödöllő, Hungary, between October 2016 and July 2020.

The solar chimney prototype is part of a joint project funded by the Science and Technology Development Fund (STDF, Project ID 5054) of Egypt and the Federal Ministry of Education and Research (BMBF) of Germany. Also, the turbine blades of this project are donated from Fiber Egypt company.

First of all, I would like to express my sincere gratitude and thanks to my God for the guidance through this work and for all the blessings bestowed upon me.

I am genuinely thankful to my supervisor, Prof. István Keppler and Ildikó Molnár, for the guidance, encouragement, and valuable advice he has provided throughout my time as his student. I have been fortunate to have a supervisor who cared so much about my work, and who responded to my questions and queries so promptly.

My most profound gratitude goes to my beloved my wife and family in Egypt and without whom this project would never have been possible, thank you so much for your love and patience all along.

I would like to express my thanks to the staff who helped me in Mechanical Engineering Doctoral school- Szent István University.

Furthermore, I would like to thank all kind, helpful and lovely people who helped me directly and indirectly to complete this work, and I apologize to those for being unable to mention them by name here.

Walid Belal

Gödöllő, 2022